ABSTRACT

WANG, RUI. Data-driven Health Prognostics for Lithium-ion Battery. (Under the direction of Dr. Mengmeng Zhu).

Lithium-ion (Li-ion) batteries have been used in a wide range of real-world applications, such as electric vehicles, portable electronics, and aerospace systems, because of their advantages of high power density, long lifespan, and low self-discharge rate. The performance of Li-ion batteries keeps declining during storage and usage, and a direct impact is the battery capacity drops during the degradation. The capacity measures the maximum energy a battery can store, and it is an important indicator for monitoring battery health status. When a battery capacity drops below a certain threshold, failure occurs to cause economic loss and catastrophic consequences. To avoid these negative influences, battery prognostic health management (PHM) aiming at detecting battery degradation status and ensuring battery reliability in a long-term, is applied by implementing tools such as state-of-health (SOH) and remaining useful life (RUL) predictions, in which SOH measures the ratio of current capacity to the initial capacity and RUL measures the elapsed time until the battery fails.

The accurate SOH and RUL prediction is challenged by both the battery operation conditions and the various capacity degradation patterns in a battery's lifetime. The operation conditions describe the battery working situations such as temperature, voltage, and current rates. Current studies have investigated these influences on battery degradation but overlooked current rates. The quantitative model that can link capacity drop to the current rates is still missing. Meanwhile, capacity degradation patterns describe various battery degradation behaviors such as different degradation rates and capacity regeneration. The prediction model needs to learn such degradation behaviors well and fit the degradation data before obtaining accurate prediction results. Current studies have applied the two-phase prediction model for the degradation process

with different degradation rates in two phases. However, the detection of change point (CP) in the two-phase prediction model has certain drawbacks. CP is either a fixed point for different battery degradation processes or a random variable, which causes the prediction model to lose fidelity or to increase model complexity. A CP detection method incorporating with RUL prediction model is missing.

The dissertation aims to fill the research gaps mentioned above. To investigate the influence of current rates on capacity degradation, a RUL prediction model based on Peukert's law (PC) function is proposed. Besides, a SOH prediction model based on the novel feature extracted from battery data at various current rates by differential voltage (DV) analysis is proposed to improve prediction accuracy. To overcome the drawbacks of the existing two-phase prediction model, a CP detection method incorporating a two-phase capacity degradation model is proposed for RUL prediction. Moreover, a new CP detection method based on voltage data is integrated with a two-phase stochastic degradation model to capture the trend of the two-phase degradation process with capacity regeneration. The integrated model is established for battery RUL prediction, and battery maintenance policies are determined based on the prediction results.

Data-driven Health Prognostics for Lithium-ion Battery

by
Rui Wang

A dissertation submitted to the Graduate Faculty of
North Carolina State University
in partial fulfillment of the
requirements for the Degree of
Doctor of Philosophy

Wilson College of Textile

Raleigh, North Carolina
2024

APPROVED BY:

_____	_____
Dr. Mengmeng Zhu Committee Chair	Dr. Eunkyoung Shim
_____	_____
Dr. Jeff Joines	Dr. Karen Chen

_____
Dr. Minh Tang

BIOGRAPHY

Rui Wang was born in Chengdu, Sichuan Province, China, in 1996. He received the B.S. degree in Mechanical Design, Manufacturing and Automation from University of Electronic Science and Technology of China in 2018, the M.S. degree in Industrial and System Engineering from Rutgers University, New Brunswick, in 2019. He became a Ph.D. student in the department of Textile Engineering, Chemistry, and Science at North Carolina State University in 2020. His research interests focus on system reliability modeling, data analysis, machine learning, Lithium-ion battery degradation modeling and remaining useful life prediction. After completing his Ph.D. studies, he plans to pursue a career in academia.

ACKNOWLEDGMENTS

I am profoundly grateful to my advisor, Dr. Mengmeng Zhu, whose expertise, understanding, and patience, added considerably to my graduate experience. Her willingness to give her time so generously has been very much appreciated. I extend my deepest thanks to the rest of my dissertation committees: Dr. Eunkyoung Shim, Dr. Jeff Joines, Dr. Karen Chen, and Dr. Minh Tang, for their insightful comments and encouragement.

My sincere appreciation also goes to the Wilson College of Textiles. I am particularly grateful for the assistance offered by the support staff in the department, and for the excellent opportunities I have been given to grow both personally and professionally.

I am also thankful to my friends, who supported me throughout this journey. Your friendship, shared laughs, and unwavering support helped me maintain my sanity and perspective. The memories we have created during these years will be treasured forever.

Finally, I must express my very profound gratitude to my parents for their love and support, not only during my PhD journey but throughout my life. Mom and Dad, I hope this dissertation makes you proud. It is not only my achievement but yours as well.

TABLE OF CONTENTS

LIST OF TABLES

LIST OF FIGURES

CHAPTER 1

1. Introduction

1.1. Background

In the current fast-paced society, the demand for fossil energy has been increasing incredibly to satisfy electricity generation, transportation, industrial processes, aviation, and shipping. The problems of fuel energy shortage and its influence on climate change are becoming serious and important. To reduce environmental pollution and ensure the sustainable development of the ecological system, renewable energy has become promising to reduce carbon emissions and prevent global warming [1].

The lithium-ion (Li-ion) battery is the mainstream energy storage device. It has been widely used in many countries and companies in a variety of industrial fields, for example, portable electronics, electric vehicles, aerospace, medical devices, and marine systems [2-3]. Specifically, portable electronics such as smartphones, tablets, laptops, smartwatches, and fitness trackers heavily rely on the energy supply of Li-ion batteries to maintain intended functions to meet users' demands. Also, medical devices such as defibrillators and insulin pumps achieve portable size because of the usage of Li-ion batteries. The Li-ion battery has advantages such as high energy density, long lifespan, low self-discharge rate, and good power capacity [3].

According to [4], the worldwide lithium-ion battery market revenue was expected to reach the level of 58.6 billion US dollars in 2024 compared to 22.5 billion US dollars in 2015. Meanwhile, the capacity of lithium-ion batteries in 2024 was expected to achieve 93.1 gigawatt hours (GWh) compared to 15.9 GWh in 2015 [5]. The trend of using lithium-ion batteries in energy storage, consumer electronics, automotive and industrial applications has risen

dramatically from 2017 to 2024. The lithium-ion battery plays a crucial role in real-world applications to meet the energy demand of society development and human daily life.

However, the performance of Li-ion batteries gradually reduces during use and storage due to degradation caused by internal electrochemical reactions, which brings economic loss and catastrophic failure for battery-supplied systems. For instance, Sony lost $430 million due to a global recall of its laptop batteries with a total amount of 9.6 million in 2006 [6]. Boeing 787 caught fire due to the failure of Li-ion batteries in 2013, which caused all airplanes to be grounded [7]. During the Li-ion battery degradation process, the risk of safety hazards like fire and thermal runaway keeps increasing, and the energy efficiency keeps decreasing. Finally, a replacement is taken to remove the failed Li-ion battery, to which a maintenance cost is usually assigned. To ensure the reliability of the battery, reduce operating costs, and guarantee its designed performance, it is critical to understand the lithium-ion battery degradation mechanisms and their causes.

A lithium-ion battery is composed of four components: two electrodes, in which two current collectors are separately attached to each of them, a separator that prevents any short circuit between these two electrodes but allows charged ions to move through, and the electrolyte, which is an extra source of lithium ions and allows facile charge transfer [8]. The variety of physical and chemical mechanisms affects the battery components at a micro-scale and triggers different types of side reactions inside the battery to cause degradation. Battery capacity [9] is an important health indicator, which represents the total energy the battery can store, and it gradually decreases as the battery degrades. The overall capacity degradation analysis framework from electrochemical perspectives includes causes, side reactions, and degradation modes. As for each degradation mode, it contains a few side reactions that are affected by several influence

factors such as design causes, production causes and operation conditions. Fig. 1.1 shows detailed information of the framework and Table 1.1 provides the framework summary.

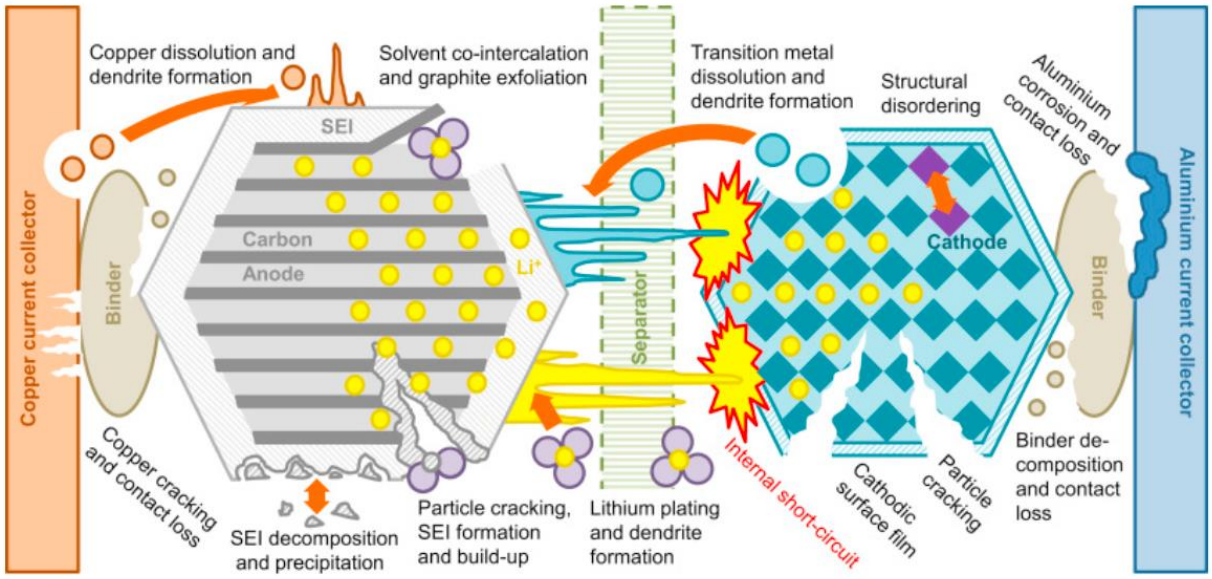

Figure 1.1. Degradation mechanism in lithium-ion battery [10].

Typically, there are three types of degradation modes: loss of lithium ion inventory, loss of anode and cathode active material, and loss of electrolyte. The battery capacity is related to the amount of the active material and lithium ions. The active material is like a tank and the lithium ion is like the water inside the tank. A loss of active material in either anode or cathode electrode represents size shrinkage in a tank and a loss of lithium ion inventory represents the reduction of water inside [11]. Besides, a large amount of electrolyte loss can lead to the end of battery life.

Side reactions are complicated and coupled in each degradation mode. For example, the loss of active material is affected by graphite exfoliation, electrode particle cracking, binder decomposition, and corrosion of current collectors. The loss of lithium ion inventory is caused by solid electrolyte interface (SEI) film formation and thickening, lithium plating, and transition metal dissolution. The SEI film formation and thickening and lithium plating also affect the loss

of electrolyte. One or more external causes can trigger the side reaction inside the battery cell. For instance, the design causes include the material selection of the anode, cathode, electrolyte in a battery cell, and the mechanical stress applied in a battery pack.

Table 1.1
Framework of battery capacity degradation

Degradation Mode	Side Reactions	Causes
Loss of lithium ion inventory	SEI file formation and thickening Transition metal dissolution Lithium plating	Material selection for cell Mechanical stress in the pack Cooling system in the pack Production line humidity Electrolyte filling method Formation method Temperature Current load Voltage Time
Loss of anode and cathode active material	Electrode particle cracking Transition metal dissolution Graphite exfoliation Binder decomposition Structure disordering Corrosion of current collectors	
Loss of Electrolyte	SEI film formation and thickening Lithium plating Electrolyte decomposition	

The principles and consequences of these main side reactions are listed as follows [8, 12]. The SEI film is the passivation layer formed when the liquid electrolyte comes into contact with the electron-conductive surface of the anode electrode. The operating voltage is usually below the stability window of the electrolyte, which leads to the irreversible breaking down of the electrolyte [13]. The SEI forms at the first cycle of a cell to result in around a 10% reduction of battery capacity and then stop the further reaction of the electrolyte at the anode electrode. However, the thickness of SEI keeps increasing as the battery degrades. Many reasons affect the growth of SEI film such as the diffusion of solvent molecules through existing SEI and new exposed electrode surfaces. High temperatures increase the diffusion rate of solvent to speed up the SEI growth, and high currents lead to particle cracking to form new SEI film [14]. The SEI film influences battery capacity degradation in several ways. The compounds in SEI include lithium, which traps it and prevents it from participating in the charge storage causing a loss of

lithium ion inventory. The SEI directly increases impedance since the lithium ions are less permeable than the electrolyte, which consumes the electrolyte solvent.

Lithium plating describes the metallic lithium ion forms on the surface of anode electrode without intercalating into it, which can happen when the anode electrode surface becomes fully lithiated or during fast charging. Even when the charge rate is moderate, temperatures below the freezing point also can slow down the intercalation reaction to cause plating [15]. Reasons affecting lithium plating include low temperature, high current, insufficient anode electrode mass, and high voltage. The plated metallic lithium ion can speed up the side reactions with electrolyte to form SEI, which isolates the remaining lithium ion without the possibility of recovery. The new growth of SEI and isolation of lithium ions lead to the loss of lithium ion inventory [16]. Moreover, lithium plating can puncture the separator to cause a short circuit [17].

The lithium ion battery itself is a complex electrochemical system, and its degradation analysis can only be achieved with systematic technical strategies. Prognostic and health management (PHM) is usually applied [6], which aims to ensure the safety and reliability of Li-ion batteries during operations. As mentioned before, battery capacity [9] is an important health indicator, which represents the maximum energy the battery can store, and it gradually decreases as the battery degrades. A battery is considered a failure if its capacity reaches the failure threshold [19]. The remaining useful life (RUL) of the battery is defined as the duration from the current time to the time when a battery fails. Hence, RUL can be described as the duration from the current time to the time when a battery capacity drops to its failure threshold [20]. Meanwhile, the battery state-of-health (SOH), which is a ratio of the current battery capacity to the initial battery capacity, can monitor the battery health status during the degradation process [21]. Both SOH prediction and RUL prediction are critical tools that can benefit PHM. Accurate

predictions ensure monitoring the battery health status, diagnosing the degradation process, and improving health management processes.

1.2. Motivation

The accurate RUL and SOH predictions are challenged by distinct operation conditions in real applications. The operation conditions include many factors such as current rate, voltage, temperature, and battery state-of-charge (SOC). SOC is a percentage to measure the ratio of current stored energy to the maximum energy, which has a range from the fully discharged state to the fully charged state. Among all factors affecting the battery degradation process, the role of charge and discharge current rates has been critical for battery lifetime. A high charge and discharge rate can accelerate capacity loss and internal resistance increase, and it also raises the temperature to affect the degradation process at the same time.

Current studies [22-23] identify the dependence between capacity fade and current rate. Peukert's law function [24-25] has been applied to RUL prediction by formulating the relationship between current rates and capacity and the Peukert's law coefficient (PC) is assumed to be constant. PC should change dynamically as the battery degrades and different PCs should be used for battery under different current rates. Thus, exiting studies on Peukert's law [24-25] show insufficient capability to predict RUL for batteries at different current rates.

Meanwhile, studies [26-33] applied feature-based methods, such as differential voltage (DV) analysis, to predict battery RUL and SOH. DV analysis can extract useful features by transforming the voltage-capacity curves from the battery data, which is effective for SOH prediction. However, features extracted from the battery data under a certain current rate may not be feasible for battery data with another current rate. This is because voltage and capacity data vary a lot with respect to current rates. In other words, features that can be commonly used

among different current rates have not been extracted by DV analysis for RUL and SOH prediction.

Despite the influences of current rates on establishing accurate RUL prediction models, the various battery degradation patterns also bring difficulties. Existing studies [19-20, 34-35] on the RUL prediction of Li-ion batteries commonly use single-phase degradation models, which limit the capabilities to capture various degradation patterns. Meanwhile, existing two-phase degradation models [36-38], which separate the degradation process into two phases based on degradation rates, a slowly decreasing phase, and a rapidly decreasing phase, have drawbacks in change point (CP) detection. CP in these two-phase degradation models is modeled in two ways. First, the CP is treated as a random variable, and a transition probability function is needed to describe the degradation status at CP, which increases the computational complexity because the RUL expression has an extra term compared to the expression with a deterministic CP. Second, the change point is treated as a fixed value, which may not be practical since it simplifies the degradation model and ignores the variations of CPs at different battery cells. The problem of CP detection in the two-phase degradation model needs to be well-addressed for accurate RUL prediction.

Motivations of the dissertation can be summarized into three perspectives: 1) current Peukert's law function limits the capability of RUL prediction at different current rates due to the coefficient being a constant. Features that can be generally extracted from battery data at all current rates are missing in DV analysis for SOH prediction. 2) A CP detection method based on the capacity drop curve is missing for the two-phase RUL prediction model to improve the prediction accuracy. 3) A CP detection method based on voltage data together with a two-phase

RUL prediction model considering capacity regeneration has not been proposed for improving prediction performance.

1.3. Problem Statement

There are still a few problems that can be further investigated to improve the performance of SOH and RUL prediction. They are listed as follows:

First, the current rate is considered an important factor that affects battery capacity degradation, and its impact needs to be investigated based on experimental data. Peukert's law function reveals the relationship between current rates and capacity, but PC in Peukert's law function is treated as constant, which causes the function inaccurate as the battery degrades. PC needs to be formulated as a function of battery cycles for battery cells at different current rates. The formulated PC values can be fed back to Peukert's law function to predict battery RUL. On the other hand, battery data obtained based on DV analysis include critical information relevant to battery capacity drop, which has not been used. Novel features need to be extracted from DV analysis for cells at different current rates. An SOH prediction model for cells at various current rates can be proposed based on extracted novel features.

Second, the current two-phase battery degradation models do not identify CP properly to separate the degradation dataset, which eventually causes inaccurate prediction results. A CP detection method based on capacity data needs to be applied in a proposed two-phase degradation model. Besides, the proposed degradation model needs to consider uncertainties among different battery cells to improve the RUL prediction results.

Third, the voltage curves of the battery data show two different patterns to correspond to battery two-phase degradation behaviors, but they have not been used for CP detection. A new method needs to be used to identify CP in terms of voltage data. Besides, the battery degradation

process has the capacity regeneration phenomena. A two-phase stochastic RUL prediction model is necessary to capture this capacity recovery behavior. Then, a RUL prediction framework including this two-phase stochastic model and CP detection method can be used for improving RUL prediction performance.

1.4. Experiment Settings

The battery data is collected from the cyclic battery test [39-44]. The battery cyclic test usually includes three steps, charge process, discharge process, and the rest time. At a specific cycle, the battery is charged from empty status to fully charged status, then it rests for a certain period before it starts to get discharged until the empty status.

Generally, the charge process has two types of modes, one is constant current charge (CCC) mode, and another is constant voltage charge (CVC) mode [42, 44]. These two modes are sequentially applied in the charge process, the battery voltage first increases at CCC mode until the upper cut-off threshold, then the battery voltage stays unchanged at CVC mode while the battery current decreases until a certain threshold. As for the discharge process, only the constant current discharge (CCD) mode is applied. The battery voltage keeps decreasing at CCD mode until the voltage reaches the lower cut-off threshold. To measure the amplitude of the charged and discharge current, C-rate, a ratio of the current rate to the battery initial capacity, is utilized to set up the level of current rate in the battery experiment.

The rest time is conducted between every charge process and discharge process, and each cycle includes two rest periods. The rest time is essential for the battery to finish side reactions in each charge and discharge process, to let battery voltage drop back to a stable level, and to change the impedance of the battery [45]. Moreover, the rest time helps the battery temperature

reach the thermal equilibrium status. The length of rest time can be set differently, from several minutes to a few hours [46-48].

In the battery experiment, a battery tester is used to conduct all the above steps of tests and automatically collect all types of measurements such as voltage, current, and capacity. A computer is utilized to receive the data sent from the battery tester, in which pre-installed software is used to store and visualize the data simultaneously. The battery tester and the computer form a battery test platform [39, 41-42, 45]. Although the battery test platform varies in different studies in terms of product specifications like structural design, sizes and shapes, basic functions mentioned above for both the battery tester and the computer are available in every battery test platform to finish the battery cyclic test.

1.5.Contributions

In this dissertation, experiments of lithium-ion batteries are conducted to collect cyclic battery data, the battery capacity degradation process is investigated, and several RUL and SOH prediction models are proposed to improve the prediction performance of PHM. The contributions of this dissertation are listed as follows:

1) The battery data is collected from the battery cyclic test under three different current rates in the lab. By calculating PC in terms of the collected capacity data and the current rate, the coefficient is not a constant as existing studies mention. Instead, it keeps changing as the battery degrades and it is different for batteries under different current rates. To accurately predict battery capacity degradation, a Peukert's law-based prediction model is proposed, in which the PC is precisely obtained. A regression model and an autoregressive model are used to fit PC. After the model parameters are determined, these two models are used to predict values of PC in future cycles. The predicted PC values are fed to calculate capacity fade, which is later applied to

predicting battery RUL. On the other hand, battery voltage data is collected at various current rates, which includes multiple curves from different cycles under each current rate. Those curves are different as the battery degrades and curves from different current rates are also significantly different. The latent information exists inside the battery data at all current rates to be used for SOH prediction. Thus, DV analysis, a feature-based prediction method, is proposed first to obtain a novel feature. Then, a statistical method is applied to link battery SOH to the extracted new feature, and then predict SOH for future cycles. The prediction results are compared with other existing features extracted in terms of other methods, such as incremental capacity (IC) analysis, cycle number, and charge voltage. It shows the novel feature from DV analysis has the most accurate SOH prediction performance. Both Peukert's law-based prediction model and the DV analysis-based prediction model provide promising results for batteries under different current rates.

2) The existing battery capacity degradation process has shown a two-phase pattern, which includes a slow drop phase and a fast drop phase. Accurate fitting capacity degradation data benefits the battery RUL prediction performance. Thus, a two-phase capacity degradation model with a dynamic CP is proposed, in which binary segmentation is utilized to identify CP. Two regression functions are used to fit battery capacity data from two different phases. Due to the variations in battery production, the measurement noise, and the process noise, this study includes uncertainties in the RUL prediction model. Then, a particle filtering-based framework considering uncertainties is developed, in which the model parameters of the proposed two-phase degradation model are updated via Bayesian inference before prediction. The framework is evaluated using both the laboratory data and NASA data. The results are compared with other

existing degradation models using particle filtering, and the proposed framework provides superior performance among all models.

3) The battery voltage data is a group of curves that vary at different cycles, which shows two different patterns to correspond to the two phases of battery capacity degradation process. Such information hidden in the battery voltage data can be captured and used for CP detection in an RUL prediction model. Thus, a hybrid method that combines dynamic time warping (DTW) and nonnegative matrix factorization (NMF) is proposed to detect the CP of capacity degradation by using discharge voltage data. DTW treats battery voltage curves as time series data and applies a distance-based measurement for all curves, which forms a similarity matrix between each curve and all the rest. NMF separates the formed similarity matrix into two small matrices, one of which has clustering properties to allocate all cycles into two groups. CP is obtained after utilizing NMF. Later, A two-stage Wiener process incorporating CP detection (TSWP-CP) model is proposed to predict RUL using both the lab data and NASA data. Two replacement policies based on the prediction results are analyzed to minimize maintenance costs for Li-ion batteries in the long term.

In Chapter 2, the state-of-art battery degradation models, SOH and RUL prediction methods are reviewed. In Chapter 3, experiments of lithium-ion batteries in the lab are introduced in detail. In Chapter 4, an RUL prediction model based on Peukert's law function is first introduced and a SOH prediction model in terms of the feature extracted by DV analysis is presented afterward. In Chapter 5, the proposed two-phase battery capacity degradation model with CP detection is first presented. In Chapter 6, the two-phase stochastic degradation model with a new CP detection method based on battery voltage data is displayed.

CHAPTER 2

2. Literature Review

The existing RUL prediction models can be classified into three groups: physics-based models [49-50], data-driven models [26-27, 39-40, 51-59]. Physics-based models are established based on information such as battery operation conditions and material properties. Data-driven models rely heavily on battery historical data and apply statistical or machine learning techniques to predict battery RUL. They consist of particle filtering methods, stochastic methods, and feature-based methods, which do not require much knowledge of failure mechanisms and electrochemical reactions of batteries. Particle filtering methods usually consider the uncertainties of model parameters and use the collected battery data to recursively update the model parameters before RUL prediction. Stochastic models [58-59] treat the battery capacity degradation process as a random process, and the next degradation state can be obtained by a certain regularity. Feature-based models include machine learning methods, Peukert's law function, DV analysis and incremental capacity (IC) analysis [26-27]. Feature-based models usually use features, such as current, voltage, and time, to predict the RUL of battery cells. These methods mentioned above are introduced in the following subsections.

2.1. Physics-based Models

Physics-based models usually take the fundamental principles of physics such as thermal heat, mechanical stress, and incorporate the chemistry and material properties within the battery to consider the degradation process and link to battery RUL prediction. They consist of a variety of models such as electrochemical models [60-62] and equivalent circuit models (ECMs) [63-65]. Physics-based models usually pair with filtering algorithms for parameter estimation and updating [61, 64]. Each group of physics-based models is reviewed below.

The electrochemical models [66] apply the nonlinear partial differential equations to describe electrochemical reactions, ion transport, and heat generation inside batteries, which consider changes in both space and time domains to investigate the battery degradation. The pseudo 2-dimensional model (P2D) [67] is the most common, which is based on the porous electrode theory, the state of partial differential algebraic equations and boundary conditions. It represents three different domains, the two electrodes and the separator, in which the transport and charge-transfer phenomena happen. Zhang et al. [68] applied a P2D model in terms of the difference in battery impedance characteristics to analyze impedance characteristics. It was found that the low-frequency band's impedance characteristics and the actual battery impedance characteristics are consistent. Then, the original model was changed and compared with the electrochemical impedance spectroscopy (EIS) model. The EIS model measured battery impedance characteristics and linked them to battery RUL. It applied an alternating current voltage to the battery and analyzed the response across a spectrum of frequencies to determine the battery impedance. The prediction error was reduced compared with the original model. Liu et al. [69] proposed a new electrochemical-model-based particle filtering framework for battery RUL prediction. The parameters of the electrochemical model are used as state variables in the state-space function of the particle filtering algorithm. These parameters are identified by giving designed current excitations to the battery. Study [70] proposed an enhanced single particle model to estimate battery SOH, in which the estimated model parameters as indicators of SOH include the number of moles of cyclable lithium and ohmic resistance. Finally, the composite SOH obtained from the estimated model parameters was used to predict RUL based on the particle filtering algorithm. The electrochemical model method requires a strong theoretical background, which can display the internal electrochemical reactions and their intensity in the

battery's degradation process. It can accurately capture lithium-ions' movement and the change trend of active substances in both electrodes. However, the lithium-ion battery is a very complex electrochemistry system with many side effects in real-time. As the working conditions vary, describing the degradation condition of the model becomes relatively difficult. The model parameters are coupled with each other, which results in poor generality and brings challenges to improve performance for real-time SOH estimation and prediction.

The ECM [63-65] treats the battery as a black box and applies electrical components to build a circuit model that can dynamically mimic the degradation characteristics of battery cells. ECMs [71] have been applied in different battery index predictions such as state-of-charge (SOC), state-of-health (SOH), and impedance analysis because of model simplicity and short execution time. The ECMs have a few variants, for example, Rint model, Thevenin model, and multi-stage RC model [63-64, 72-73]. Tran et al. [63] proposed the Thevenin model and estimated the model parameters via nonlinear curve fitting algorithms, in which an empirical function was built to describe the relationship between the estimated parameters and SOC, SOH, and temperature. Wei et al. [72] added a parallel module of resistor and capacitor to the first-order Thevenin model to describe the battery degradation process. The grey neural network was utilized for training, in which health indicators were taken out as input parameters and capacity degradation was used as output parameters. Finally, battery SOH is predicted based on the defined health indicators. Study [73] applied the Thevenin model and empirical degradation model, which accurately estimate the capacity loss and battery lifetime. The dataset used for prediction was driving cycle data from the real operation of electrical vehicles, in which both highways and cities' roads at different temperatures were considered. He et al. [74] made a comparison of different order RC equivalent circuit models. A second-order RC model had its

performance improved greatly, which indicates that the second-order RC network model for dynamic state estimation can have better results. Xia et al. [64] applied a second-order RC model to approximate the battery performance. A cubature particle filtering method based on the cubature Kalman filtering and particle filtering was used to achieve an accurate and stable state-of-charge estimation. Shi et al. [75] proposed a second-order RC model for SOH prediction, in which the improved unscented particle filtering algorithm was applied. The unscented Kalman filtering was used to obtain the importance probability density function for the particle filtering algorithm.

Overall, physics-based models have high fidelity in considering battery degradation mechanisms but require computational costs. For example, the electrochemical model parameters can be different between different types of batteries even different cells, which needs complex optimization and data fitting techniques. Solving equations of electrochemical models usually requires a high computational cost. ECMs require strict operation conditions such as specified battery types and constant ambient temperature to be implemented [71]. The ECM has fewer parameters, and stronger timeliness compared with electrochemical models for SOH estimation and prediction. However, some weak influence SOH attenuation change may not be considered due to the approximation.

2.2. Data-driven Models

2.2.1. Feature-based Models

The neural network models [76] are a subset of machine learning algorithms that mimic the structure and functioning of human brain to recognize patterns and make decisions based on the simulated biological neuron signals, which include artificial neural network (ANN), convolutional neural network (CNN), recurrent neural network (RNN), and long short term

memory (LSTM) neural network. ANN consists of many neurons according to certain rules with very strong learning ability. ANN can achieve any nonlinear mapping by increasing the number of layers and neurons [76]. CNN is a feedforward neural network comprised of the convolutional layer, pooling layer, and fully connected layer, in which the back propagation algorithm is used to update the weights. CNN can extract data features and reduce the data dimensions due to its structural characteristics in local correlation as well as weight sharing [77]. RNN is utilized for time series problems, and it includes a dynamic memory that can analyze complex problems by assigning proper values of weights. Each layer of RNN consists of a recurrent connection with a tap delay. The output of RNN is subject to the output of the hidden layer at the present and previous instants [78]. LSTM is a variant of RNN, which is comprised of an input gate, an output gate, and a forget gate. LSTM can alleviate the vanishing gradient problem of RNN [79].

Study [80] estimated both SOC and SOH by applying a set of five ANNs for the regression and classification tasks. The estimated SOC was based on capturing the aging behaviors of batteries, and the SOH prediction was in terms of SOC in a recursive closed-loop. The dataset used was from a real drive profile in an electric vehicle. The prediction model provided promising results at last. Study [81] proposed an ANN model to predict battery RULs under different training datasets. A multi-channel input profile was utilized to compare with single channel input profile. The multi-channel input profile-based RUL prediction had shown superior performance over the single channel input profile by using the NASA battery dataset. Zhang et al. [82] proposed a hybrid model that combines the partial increment capacity and ANN to estimate SOH and RUL under the constant current discharge conditions. At first, strong correlation features were extracted from incremental capacity curves under the smoothing effect from the advanced filter method. Then, features are fed into two ANNs for SOH and RUL

prediction simultaneously. Wu et al. [83] investigated the curves of terminal voltage from different charge cycles and proposed a feed-forward neural network model incorporated with importance sampling methods to predict battery RUL. Kong et al. [84] improved battery prognostic by combining voltage-dependent and temperature-dependent health indicators, extracted from battery degradation data, in the proposed model. Liu and Xu [85] obtained energy-based health indicators via voltage curves of the battery discharge process. However, these health indicators are greatly affected by the quality of collected data.

CNN, RNN, and LSTM are often incorporated for RUL prediction. For example, Ren et al. [86] proposed a prediction model that combines CNN and LSTM considering both the spatial and temporal perspectives to solve the problem of insufficient degradation data. An autoencoder was utilized to augment the dimensions of data for better training of the proposed hybrid model. The proposed model is applied to real-world datasets to show the effectiveness and accuracy compared with other existing prediction methods. Study [87] proposed a sequential CNN-LSTM model for accurate RUL prediction. Six features were obtained first, and they are fed into CNN model for filtering. The CNN hyperparameters were optimized by using orthogonal experiment. At last, the time-series features flattened by CNN and the non-time series feature are fed into LSTM for RUL prediction. Kara [88] proposed a CNN-LSTM model to extract the spatio-temporal relations in time series data and obtain the nonlinear characteristics of battery degradation for accurate RUL prediction. Meanwhile, particle swarm optimization was utilized to identify the optimal hyperparameters of the hybrid model, which includes the number of convolutional and LSTM layers and the size of neurons in each layer. The proposed model had shown better results compared with other machine learning models. Zhang et al. [89] proposed an LSTM-RNN model to solve the problem of insufficient learning in the long-term

dependencies of the degradation characteristics of the battery. The LSTM-RNN is optimized by applying the resilient mean square back-propagation method. Song et al. [90] proposed an RNN with gated recurrent unit to overcome the problem of handling the long-term relationship of RNN. The structure of the proposed model was much simpler to contribute to a higher computational complexity.

Vector machine models include support vector machine (SVM) models and relevance vector machine (RVM) models. SVM is a supervised machine learning algorithm that can find a hyperplane to classify the data into several groups in space. These models not only return accurate prediction results based on limited data samples but also overcome the problems of easily falling into optimal local extremum. RVM is an improved machine learning algorithm in terms of sparse Bayesian theory. The algorithm of RVM reduces the dependence on kernel function and penalty factor selection. Nuhic et al. [91] applied SVM regression algorithm for battery SOH and RUL prediction, in which a new method for training and testing data processing in terms of load collectives was used. The prediction was conducted based on data from real driving profiles. Widodo et al. [92] first extracted sample entropy feature of the discharge voltage data, and applied SVM and RVM to predict SOH, in which the sample entropy feature was treated as input and SOH was treated as output. Study [70] integrated the classification and regression properties of support vectors in terms of machine learning techniques. The classification and regression model first provided a gross estimation based on features obtained from SVM, and support vector regression was applied to predict RUL when the battery is close to the end of life. The features used in this study and the multistage approach achieve RUL prediction for multiple batteries at the same time. Zhang et al. [93] proposed an SOH prediction model based on an optimized RVM model. The model reduced the amount of data for online

training compared with traditional SVM, which provides a new solution of embedded calculation for predicting battery SOH.

Peukert's law function has been extensively implemented to allow the transformation of battery capacities among different discharge rates, and it was originally developed for lead-acid batteries and introduced to lithium-ion batteries [24-25, 94]. This function describes the battery capacity is a power function of the current rate, and the capacity can be calculated once the current rate is known. PC is the coefficient in Peukert's law function, which is usually assumed to be a constant [94-96]. For example, study [37] obtained the optimal PC value by minimizing the relative error between the actual battery discharge time and the estimated discharge time. Similarly, study [95] treated PC as a fitting parameter to obtain the battery discharge time for high constant discharge rates. However, the accuracy of Peukert's law function in describing the capacity drop is reduced under dynamic battery working conditions [97-98]. Especially, the value of PC is not constant but varies during the lifecycle, discharge rates, and temperature [98-99]. For example, study [99] applied the Coulomb counting method to adjust PC, which shows PC was affected by the current and voltage. Also, study [98] considered PC a function of temperature, lifecycle, and current ratio. The above studies started to investigate the dynamics of PC instead of treating PC as a constant. They lacked exploration of variations in PC for battery cells at different discharge rates.

DV analysis and IC analysis have received abundant attention for SOH prediction [26-33]. Both DV analysis and IC analysis demonstrate the ability to reveal various degradation statuses by analyzing the variations of DV or IC curves. These two methods only require data on voltage, current, and cycle number, which is available during the battery tests [27]. Unlike extracting features from direct measurable parameters such as voltage and current, DV analysis

and IC analysis allow features to be extracted by transforming the voltage-capacity curve. The transformed curve enhances the visibility of voltage plateaus in the voltage curve and displays them as identifiable peaks. The peaks of both DV and IC curves show the phase transition of the lithium intercalation and deintercalation, and the battery degradation status can be reflected by changes in peak position, height, and enclosed area of these curves [28].

IC analysis has been applied to studies [26, 29-31] on battery SOH prediction. For instance, Li et al. [26] conducted IC analysis based on partial charging data, and correlated battery SOH to the positions of identified features from the IC curve via a linear regression model. He et al. [29] applied a Lorentzian function-based model to mimic the battery IC curve, and a group of significant features was extracted from the model for SOH prediction. Li et al. [30] conducted IC analysis after smoothing by using the moving average, Gaussian filter, and voltage window methods. Indexes at a specific interval of the IC curve were used as features, and grey rational analysis was applied for SOH prediction. The quality of IC curves in the above studies [26, 29-31] is affected by the filtering method, which aims to reduce noise and increase curve smoothness. The extent of smoothness resulting in good prediction performance can be difficult to determine.

Compared to IC analysis, DV analysis has two advantages to be used for SOH prediction. First, the voltage sensor has a smaller impact on DV calculation accuracy than that of IC calculation accuracy [28]. Second, the DV curve is linear in terms of time, which shows the uniformity of lithium distribution [27, 100]. For example, Zhang et al. [27] conducted the 3C battery test, in which C represents the ratio of current to battery initial capacity. DV analysis was applied, and two features were extracted from DV curves for state-of-charge (SOC) estimation. The SOH prediction was obtained by using the coulomb counting based on estimated SOC. Xia

et al. [101] considered the 1 C battery test. The DV curve was separated into two capacity regions, and they are treated as features for SOH prediction. Wang et al. [102] found two inflection points from DV curves for SOH prediction, in which the second point was highly linear with battery capacity. The battery tests were also conducted at 1 C. Zhou et al. [103] proposed an online SOH prediction method based on DV analysis and inconsistency analysis. The region capacity from DV curves was obtained as a feature.

Overall, feature-based models directly obtain useful features to link to battery capacity and use the extracted features for SOH and RUL prediction. The performance is subject to the model specific analytic expression and the extent of correlation between features and battery capacity.

2.2.2. Particle Filtering Methods

Particle filtering methods [42, 104-108] show advantages such as self-correct and overcoming disturbance. For example, Wang & Feng [104] proposed a Wiener process battery degradation model, in which maximum likelihood estimation was used to initialize the model parameters and unscented particle filtering was utilized to dynamically estimate the model parameters. The proposed model showed superiority and effectiveness compared to other RUL prediction models. Chen et al. [105] proposed a novel model based on the second-order central difference particle filtering algorithm. The particle degeneracy phenomenon of particle filtering was solved by optimizing the importance probability density function. Two datasets, NASA dataset and CALCE dataset were applied to the proposed model to evaluate the accuracy and effectiveness. The stability of the proposed model was verified by observing the small width of the PDF of RUL obtained by the proposed model. Duan et al. [106] proposed a novel extended Kalman filtering model, in which the extended Kalman filtering was used as the sampling density

function to optimize the particle filtering algorithm. The proposed model was applied for RUL prediction, and it showed a higher accuracy compared to the standard particle filtering algorithm. Kim et al. [108] proposed a novel prognostic model for battery RUL prediction, in which the proposed model based on particle filtering algorithm can detect the data point of state changes. Zheng & Fang [109] utilized unscented particle filtering to provide a precise description of the state equation for the degradation model, which showed a high prediction accuracy. Zhang et al. [110] utilized unscented particle filtering to generate the proposal distribution and applied the linear optimizing combination resampling method to remove the deficiency of particle diversity.

Particle filtering methods usually combine with the empirical battery degradation models to achieve good RUL prediction performance. For example, He et al. [19] used a two-term exponential function to describe battery capacity degradation. Wang et al. [20] employed a one-term exponential function to fit the capacity degradation process. Micea et al. [34] utilized a quadratic polynomial function to describe capacity degradation. Xing et al. [35] integrated a quadratic function with an exponential function to measure capacity degradation. However, these models [19-20, 34-35] have limited capabilities to capture various degradation patterns.

Studies [19-20, 34-35] above applied the particle filtering method because those studies consider the good convergence properties of this method in the model parameter updating process, which ensures the predicted battery degradation trend is close to the true one. However, the selection of prior distribution in the updating process needs to be carefully considered, which usually affects the updated parameters and the prediction results.

2.2.3. Stochastic Models

Stochastic models require lower computational demands than machine learning models and less specific knowledge on battery chemical degradation mechanisms than electrochemical models,

which still can provide good RUL prediction [111]. The Wiener process has been used by many studies [38, 112-114] for RUL prediction because it can capture the non-monotonic degradation pattern. It is a diffusion process with Brownian motion incorporating a drift coefficient. Wiener process has linear and nonlinear drift coefficients in terms of different degradation processes. For example, Tang et al. [114] developed a degradation model in terms of the linear Wiener process integrating measurement error. Xu et al. [113] proposed a nonlinear Wiener process model with time-varying temperature conditions, in which the drift coefficient is a time-dependent function, and the random parameter for the degradation rate is a function of time and temperature. Kong et al. [115] proposed an accelerated stress factors-based nonlinear Wiener process model. Peukert's law and the Arrhenius equation were used as two specific accelerated stress-relevant drift functions in the proposed model. RUL prediction was conducted under different temperatures and different discharge rates. The robustness and accuracy of the proposed model were evaluated by comparing it with other existing RUL prediction models. Zhang et al. [116] proposed a Wiener process model that considered both the measurable and unobservable external impacts on battery degradation. The measurable time-varying covariate was modeled by an Ornstein-Uhlenbeck process, and the unobservable factors were modeled by a time-varying rate via Brownian motion. Both impacts are fused in the proposed wiener process model for RUL prediction.

Wiener process can describe two-stage and multi-stage degradation processes by introducing the CPs. For example, Zhang et al. [117] proposed a TSWP model with a CP by considering uncertainties of the degradation state at the CP. The battery dataset from Maryland University was utilized for predicting RUL, in which the model parameters were estimated by MLE. Lin et al. [38] proposed a TSWP model to capture battery degradation. The model includes

nonlinear drift coefficients for degradation functions from both stages, which are bounded by the CP. Wen et al. [118] proposed a Wiener process degradation model that has multiple CPs and assumed parameters as random variables to represent the between-unit heterogeneity. Liao et al. [119] developed a multi-stage Wiener process degradation model with jumps. The diffusion and drift coefficients were determined by the expectation maximization algorithm and updated at the online prediction stage.

Stochastic models capture the variability of the battery degradation process such as capacity regeneration to enhance the model fitting and incorporate randomness in prediction by considering all possible scenarios with probabilistic approaches. However, the model complexity is usually high in terms of the model analytic expression.

2.3. Battery Experiment

The battery cyclic test is conducted under the battery test platform [39, 41-42, 45]. As mentioned before, the battery test platform can be different in different studies, but it usually consists of a battery tester and a computer. One can conduct the specific test and collect the battery data, another is responsible for receiving the collected data and storing it. The software in the computer helps the operator to design the experiment settings and can control the testing process of the battery tester in real-time. Applying this type of battery test platform to collect battery data is beneficial to research battery SOH and RUL predictions.

Shen et al. [39] established a test platform to test NCR18650B lithium-ion batteries. The computer had a software named battery test system (BTS), which can design different experiments and monitor the testing process. The computer is connected to a control unit, which is the intermediate unit between the computer and the battery tester. The control unit used the TCP/IP communication protocol to ensure real-time data transmission during the battery test.

The above battery test platform is built under the ambient constant temperature, other platforms can control the environmental temperature for the battery test by adding a Thermal chamber [41-42]. For example, Tong et al. [41] used NEWARE CT-4008T battery tester to test APR18650M1A lithium-ion batteries, in which batteries were put inside a thermal chamber named GDH-2005B. The temperature chamber provided holes that allowed wires of batteries to connect to the battery tester outside. Lai et al. [42] also implemented a temperature chamber in the test platform. Only batteries were sat inside the chamber and the batteries were connected to the battery tester via chamber holes. The computer and battery tester are connected via TCP/IP communication protocol as well to ensure data transmission. The above two platforms allowed the environmental temperature of battery testing to be significantly different compared to the normal ambient temperature, which facilitated the battery degradation test especially for high temperature to meet their experiment goals. Study [43] aimed to measure the swelling force of lithium-ion batteries when they were charged and discharged. A force sensor was added to the test platform. The battery cells were put between two metal plates, in which a pre-loading force was given in one of these two metal plates. The swelling force of battery cells can be detected by the installed sensor. Although different battery test platforms were conducted in different studies due to different research goals, all these platforms can perform the basic testing functions for lithium-ion batteries to meet the requirements of designing battery tests, collecting the battery data, and controlling the testing process.

The battery cyclic test includes three steps, charge process, discharge process, and rest time. As for the charge process, lithium-ion batteries are usually charged as CCC and CVC modes. C-rate, a ratio of the current level to the battery initial capacity, is applied to measure the amplitude of current during the battery test. 1 C means the battery can be charged for 1 hour at

the constant current level of its capacity while 2 C indicates the battery can be charged for half an hour at the constant current level of its doubled capacity. However, real experiments usually need CVC followed by CCC to get the battery fully charged. Different C-rates can be set up for CCC mode, for example, 0.5 C at studies [45, 120], 1 C at studies [39, 41, 43, 121] and 2 C at studies [41, 122]. As for the CVC mode, the constant voltage is determined by the specification of the tested battery cell. During this process, the battery current keeps decreasing, and the process is terminated when the current drops below a certain threshold. Different studies [39, 41-43, 45, 123] applied different thresholds for the current. As for the discharge process, C-rate is also utilized to measure the current level. The settings of C-rate are quite different, such as 1 C, 2 C, 3 C, and 5 C [41-42, 45, 124]. Low current rates were usually used when the studies focused on investigating the effects of low current rates on the battery degradation process while high current rates were usually set up when the studies care more about battery fast degradation and collecting accelerated degradation data. The rest time allows batteries to finish the side reactions between each charge and discharge process to provide more available capacity for future cycles. The setting of rest time also varies from seconds to a few hours [43, 125-127]. The consideration of rest time length is similar to that of the current rate. The short rest time could be insufficient for battery cells that causes fast degradation in the accelerated test while the long rest time may be related to measure battery open circuit voltage (OCV), which only becomes stable and measurable after resting for a long time. All these different experimental settings of lithium-ion batteries serve different purposes of studies in SOH and RUL predictions.

The exiting data resources can be grouped into two parts, one is lab data which is designed by researchers on their own to meet the research needs, another is public data which includes battery data for some typical types of lithium-ion batteries such as coin, cylindrical, and

prismatic batteries under specific testing conditions. Public data has been published for a few years to serve many researchers and their studies, and it is also used as benchmark data to evaluate and highlight the contributions of many studies [128]. As mentioned in study [128], from a historical point of view on the battery dataset, the battery experiment has been scaled up in the past 20 years. The number of tested cells has increased from a few to hundreds. Besides, the interest in types of lithium-ion batteries has changed from lithium iron phosphate (LFP) to nickel manganese cobalt oxide (NMC) and nickel cobalt aluminum oxide (NCA) in recent a few years. The test conditions of batteries are also expanded to consider more factors such as varied initial SOC and varied cut-off voltage in battery cyclic tests. There are a few groups of public lithium-ion battery datasets commonly used by existing studies [19, 27, 35, 129-131]. Two popular datasets are selected from them in this section to give detailed descriptions as follows. NASA dataset [129] included data of 34 lithium-ion batteries that have a capacity of 2 Ah. The batteries were cycled at various temperatures such as 4 ℃, 24 ℃, and 43 ℃, in which they were charged at CCC and CVC modes and discharged with different cut-off thresholds. The dataset had information on measurements such as voltage, current, discharge capacity and impedance. CALCE battery dataset [19, 35] had 15 LCO prismatic CS2 battery cells with different capacities such as 0.9 Ah and 1.1 Ah. These batteries were tested under room temperature of 23 ℃, in which the test had different depths and ranges of charge and discharge processes. Besides, this dataset also includes 12 LCO prismatic CX2 battery cells with a capacity 1.35 Ah, which are tested at a range of temperatures such as 25 ℃, 35 ℃, 45 ℃, and 55 ℃. The availability of public data facilitates the research in battery SOH and RUL predictions.

CHAPTER 3

3. Experiments

The purpose of this dissertation is to propose battery SOH and RUL prediction models based on the investigation of the battery degradation data. The battery experimental setup is described in this section. The experiments in the lab collect battery data that is used by studies in the subsequent chapters. Except the battery data in the lab, some well-known public battery datasets are also introduced in this section, which are utilized as an extra example in Chapters 5 and 6 to evaluate the proposed prediction model.

As shown in Fig. 3.1, the test platform consists of battery testers and a monitoring computer, in which RS422 and universal series bus (USB) ports are implemented to ensure signal transmission. The battery tester allows two types of battery connections so that the tested battery cells can be linked by the cell or wire channels. A variety of test modes are allowed in the battery tester, for instance, CCC, CVC, and CCD. The monitoring computer with the testing software has two main functions. One is Programming, which allows customization of experiment designs and controls the charge and discharge process of the battery tester. Another is Visualization, which facilitates the process of data recording.

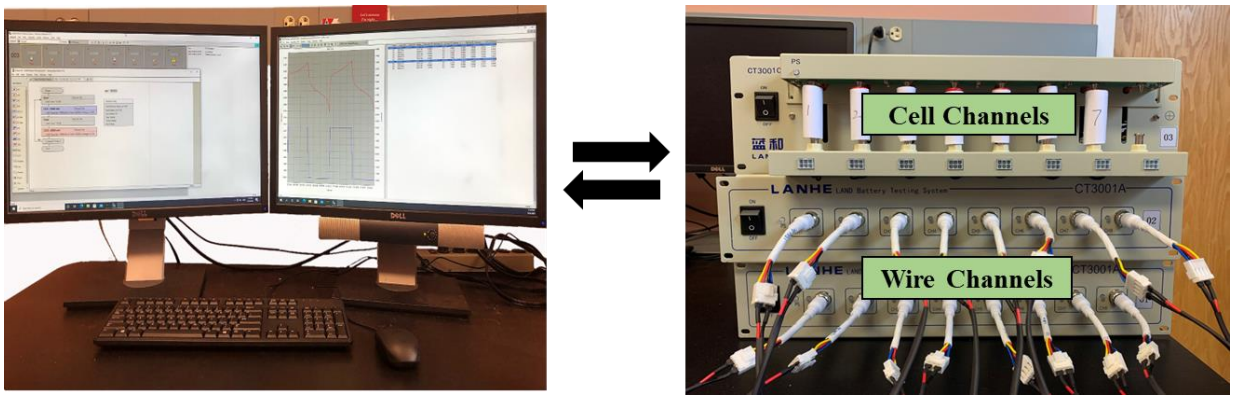

Figure 3.1. Battery test platform.

To guarantee the functionality of the monitoring computer, a software coming together with testers at purchase is installed. In Fig. 3.2, the software has one interface that displays the overall test status for all battery testers. Each row in this interface indicates one battery tester, and the red number in the front represents the label of this tester. At this moment, only two testers are on and displayed in this interface. As for all squares shown in each row, they represent the individual channels of a typical tester. All channels are independent of each other to ensure the battery test can be conducted separated without disruption from other channels. Some of these squares show the word “End” to indicate the test is done for the current channels. Some of these squares carry an arrow with either blue or red color to show the battery is under either charge or discharge process.

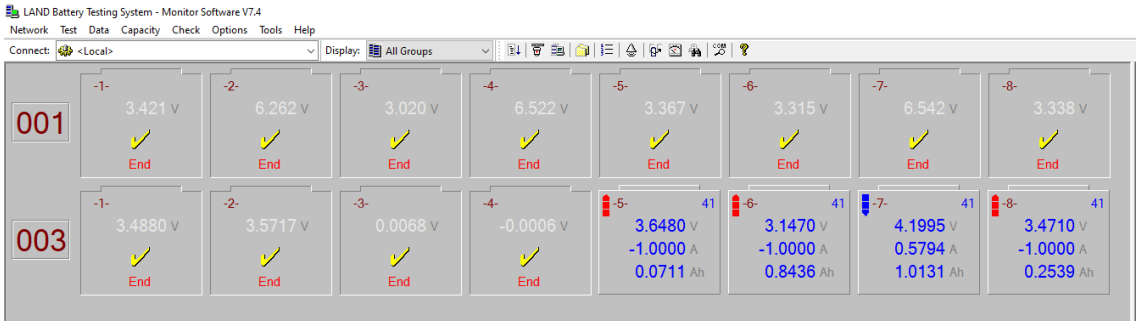

Figure 3.2. Battery test monitoring interface.

The software has a design interface for users to set up different battery tests. An example is shown as follows. The battery test is conducted for 5 cycles, and each cycle includes three different test modes, CCC, CVC, and CCD. Each mode has several ending conditions, which can be set up based on experiment needs. As for the charge process, the upper cut-off voltage of 4.2 V is applied as the threshold to stop CCC while the cut-off current of 200 mA is applied as the threshold to stop CVC. Besides, the lower cut-off voltage threshold for CCD is set as 2.75 V. The rest time is set as 1 minute between every charge and discharge process. All data is recorded every 10 seconds.

The software also allows visualization of collected data in real-time, and it can show large size of data when a battery is tested for many cycles. Fig. 3.3 shows an example of collected data. On the left-hand side, the voltage and current raw data are plotted according to testing time. Both voltage and current curves recursively change with consistent patterns among all cycles. On the right-hand side, all data are numerically recorded to form a table. The table includes a lot of information not just the measurements such as current, voltage, and capacity, but also shows the number of cycles, steps in each cycle, system time, charged and discharged power, and so on. By checking out the plotted curves and the recorded data, it is easy to match them and export the data as needed.

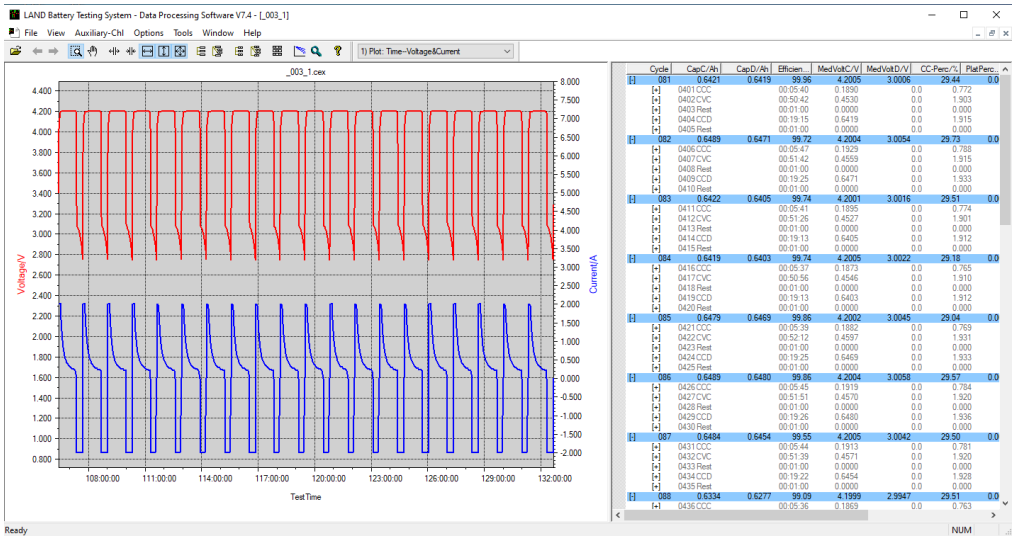

Figure 3.3. Battery test visualization interface.

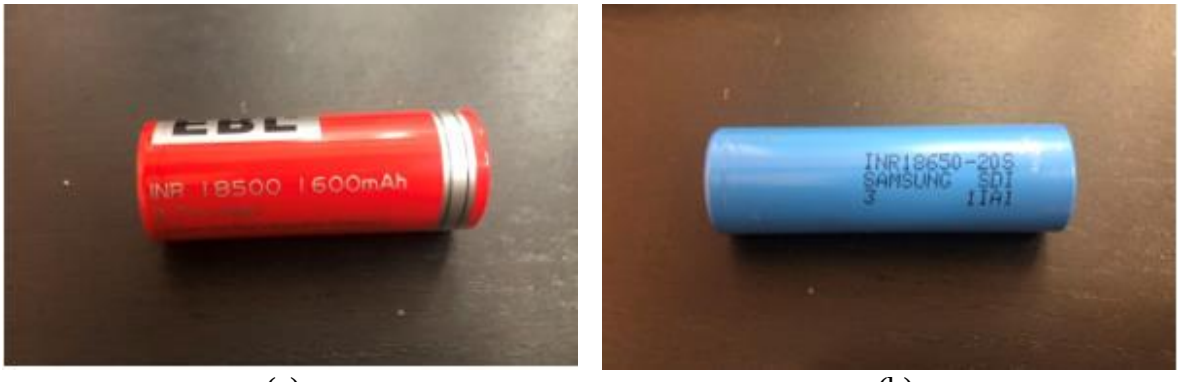

(a) (b)

Figure 3.4. Battery cells for testing: a) EBL; b) Samsung.

In this dissertation, cylindrical battery cells produced by EBL and Samsung are used to conduct battery capacity tests, as shown in Fig. 3.4. The specifications for the tested battery cells are given in Table 3.1 and Table 3.2. As for EBL battery cells, tests under CCC and CCD with 1.25 C rate (2 A) are conducted at 25°C ambient temperature at each cycle. The cut-off voltages for the charge and discharge process are 4.25V and 2.75V, respectively. The battery cells are rested for one minute between each charge and discharge cycle.

Table 3.1
Specifications of the tested EBL Li-ion battery cells

Type	EBL18500
Cathode	$Li(NiMnCo)O_2$
Nominal capacity (Ah)	1.6
Nominal voltage (V)	3.70
Lower cut-off voltage (V)	2.75
Upper cut-off voltage (V)	4.25

Table 3.2
Specifications of the tested Samsung Li-ion battery cells

Type	Samsung 18650 20s
Cathode	$Li(NiMnCo)O_2$
Nominal capacity (Ah)	2
Nominal voltage (V)	3.70
Lower cut-off voltage (V)	2.50
Upper cut-off voltage (V)	4.20

As for the Samsung battery cells at each cycle, they first get charged under the constant current charge (CCC) phase until the voltage increases to 4.2 V. Then, it gets charged at the constant voltage charge (CVC) phase until the current drops below 200 mA. After resting for 1 minute, the battery cell is discharged under the constant current discharge (CCD) phase until the voltage drops to 2.75 V. At last, the battery cell is rested for 1 minute. As for C-rate in the charge and discharge process, different current rates have been employed for different cells, they are 1 C, 2 C, and 4 C.

CHAPTER 4

4. An Investigation on Lithium-ion Batteries Degradation Characteristics under Different Discharge Rates and Remaining Useful Life Prediction

4.1. Peukert's Law-based Prediction Model

4.1.1. Introduction

Lithium-ion batteries show a lot of advantages such as high-power density, long lifespan, and lightweight to take the dominating marketplace in rechargeable batteries for all types of devices and systems, such as marine systems and electronic devices [9, 124, 132]. The battery capacity degradation process is influenced by a few significant factors [124], for example, ambient temperature, storage voltage, depth of discharge, etc. As an important factor, the discharge rate has a large influence on the battery degradation trend [97]. However, the quantitative analysis of the relationship between the capacity and the discharge rate is not sufficiently investigated, which limits the use of discharge rates in battery degradation characteristic analysis.

The battery degradation mechanisms can be classified into three groups: active material loss, internal resistance increase, and lithium inventory loss [133]. For instance, the Li ions are transmitted between the battery anode and cathode during the charge and discharge process to ensure energy transmission. The lithium inventory gradually loses due to battery aging and operation conditions. Despite the degradation in the electrochemical perspectives, various discharge rates, a representative of battery operation conditions to indicate dynamic battery working loads, can also significantly affect the battery degradation process [98, 134]. Since the battery capacity degradation is not a deterministic process for various discharge rates, it brings challenges for battery PHM [115, 135-136], in which the basic goal of PHM is to maximize the operational capability, reduce the maintenance cost, and improve the reliability of products or

services by RUL prediction [137]. Thus, the relationship between the battery capacity and the discharge rate requires further investigation.

Thus, this study aims to provide a thorough investigation into the variations and dynamics of PC at different discharge rates and provide a battery RUL prediction tool based on Peukert's law function. The contributions are listed as follows:

(1) Demonstrate the battery degradation characteristics at different charge and discharge rates for the laboratory testing data.

(2) Apply a nonlinear regression model and an autoregressive model for fitting PC at different discharge rates.

(3) Conduct battery RUL prediction based on the regression models and evaluate the performance.

The remaining parts of this study are organized below. Section 4.1.2 provides the details of experimental designs and visualizations of collected battery degradation data. Section 4.1.3 introduces the concept of Peukert's law function, displays the regression models for PC, and provides the results of battery RUL prediction. Section 4.1.4 gives the conclusion of this paper and future studies.

4.1.2. Experiment

A group of tests is conducted to obtain the battery degradation data at different discharge rates in the laboratory. The battery cells are Samsung 18650 20s lithium-ion batteries with Li(NiMnCo)O2 cathode and graphite anode. The specification of this type of battery is displayed in Chapter 3. The nominal capacity is 2 Ah, the nominal voltage is 3.7 V, and the cut-off charge and discharge voltages are 4.2 V and 2.5 V in terms of the manufacturer's specifications. All tests are under the ambient temperature of 25 ℃. The equipment setup and the battery experimental

designs can be viewed in Chapter 3. Three battery cells are selected in this study, they are cell #2 at 1 C, cell #9 at 2 C, and cell #13 at 4 C.

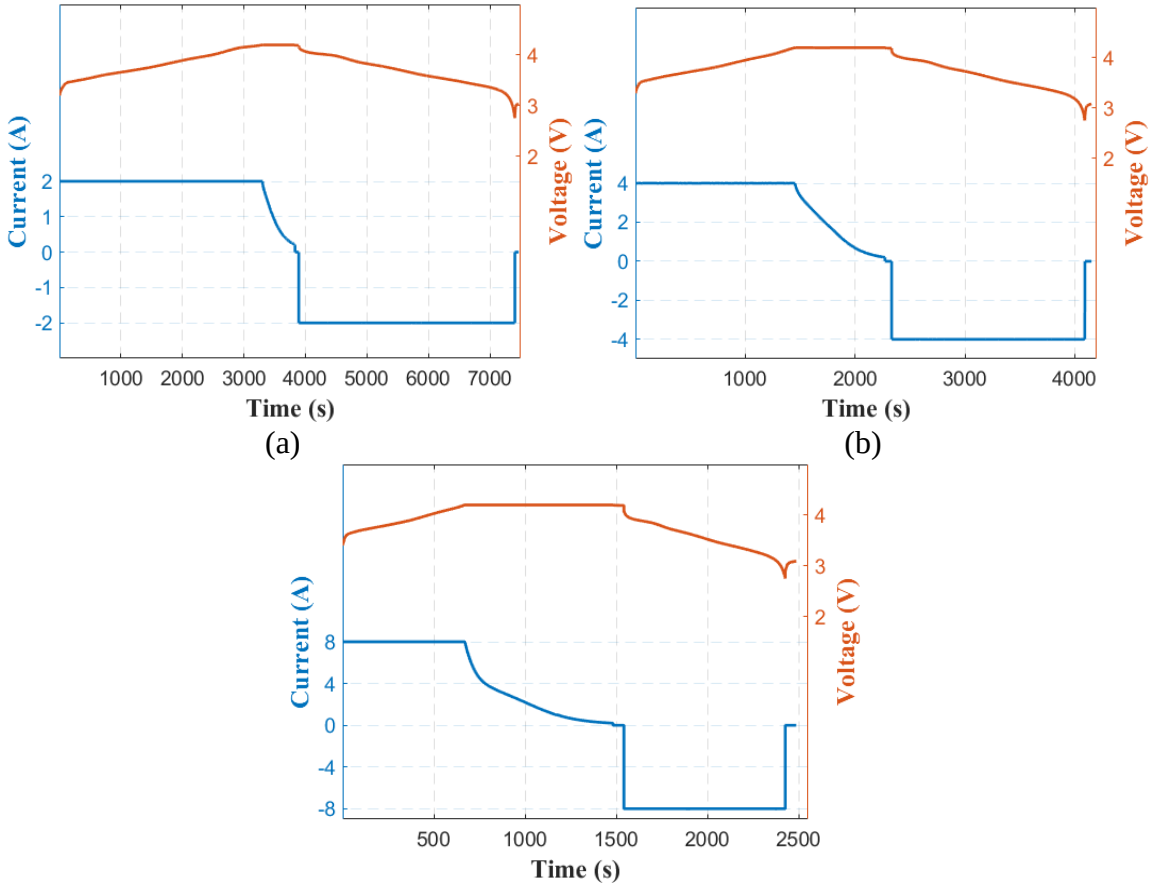

Figure 4.1. Profiles of voltage and current in charge and discharge processes: (a) cell #2; (b) cell #9; (c) cell #13.

The charge and discharge profiles for the first testing cycle of three battery cells are displayed in Figs. 4.1(a)-(b). The voltage and current curves show similar trends for all three cells, though, the amplitude of current for each cell is different from one another. Fig. 4.2(a) shows the curves for voltage drop and capacity released during the discharge process at the first testing cycle. Although the nominal capacity indicated by the manufacturer is 2 Ah, the true capacities measured at the first cycle for cells #2, #9, and # 13 are 1.95 Ah, 1.96 Ah, and 1.96 Ah, respectively. Thus, the measured capacities for all cells are treated as the initial capacities. The battery voltage curves at all discharge rates drop to the cut-off threshold, in which the cell

voltage with the 4 C test decreases more rapidly than other cells at the early stage while the cell voltage with the 1 C test decreases more rapidly at the end of the discharge process.

To demonstrate the capacity degradation pattern, the discharge capacity curves for all cells with all testing cycles are displayed in Fig. 4.2(b). The capacity includes degradation data from 100% to 85% for each cell. The number of cycles when the battery cell reaches 85% is 1059, 998, and 711, correspondingly. The cell with the 4 C test has a sharper decreasing slope and shows a smaller number of cycles than the other two cells.

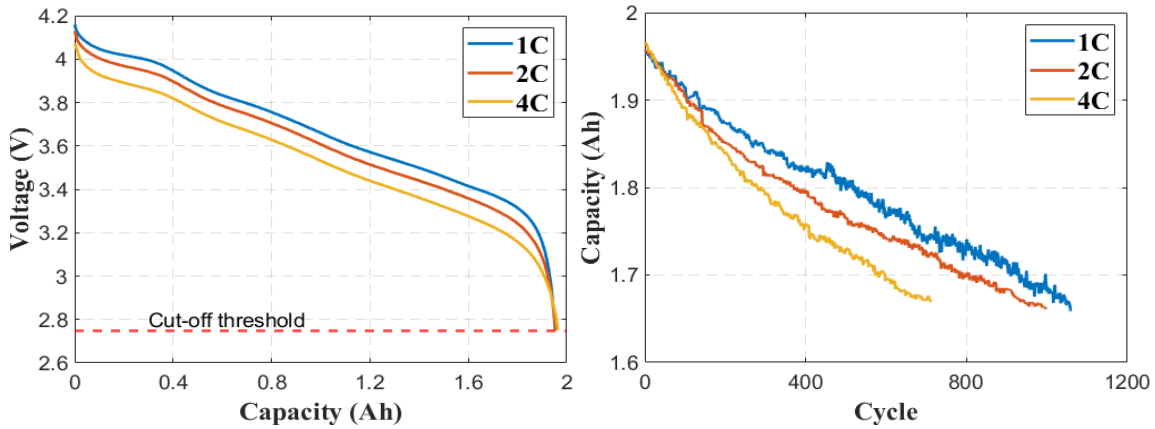

(a) (b)

Figure 4.2. (a) Discharge voltage drop vs released capacity at the first cycle for all cells; (b) Discharge capacity vs cycles for all cells.

The variations of battery degradation behaviors at different discharge rates are also observed from the detailed measurements in Fig. 4.3. Fig. 4.3(a) presents the charge current curves with time for cell #2 with the 1 C test at different numbers of cycles. A similar current curve to cell #2 is observed from cell #9 with the 2 C test and cell #13 with the 4 C test. So, Fig. 4.3(a) only displays the current profiles for cell #2. As the number of cycles increases, the battery cell takes less time to reach the constant voltage charge phase, and the current drops slower at the end of the charge process. Fig. 4.3(b) displays the discharge voltage curves with the number of cycles for all three cells. The voltage curves drop faster as the number of cycles increases. Fig. 4.3(c) and (d) show the charge time and discharge time with the number of cycles

among all cells. The charge time for each cell remains almost unchanged at all cycles, which also can be seen in Fig. 4.3(a), as all current curves almost stop at the same time point. The discharge time shows a linear pattern for all three cells.

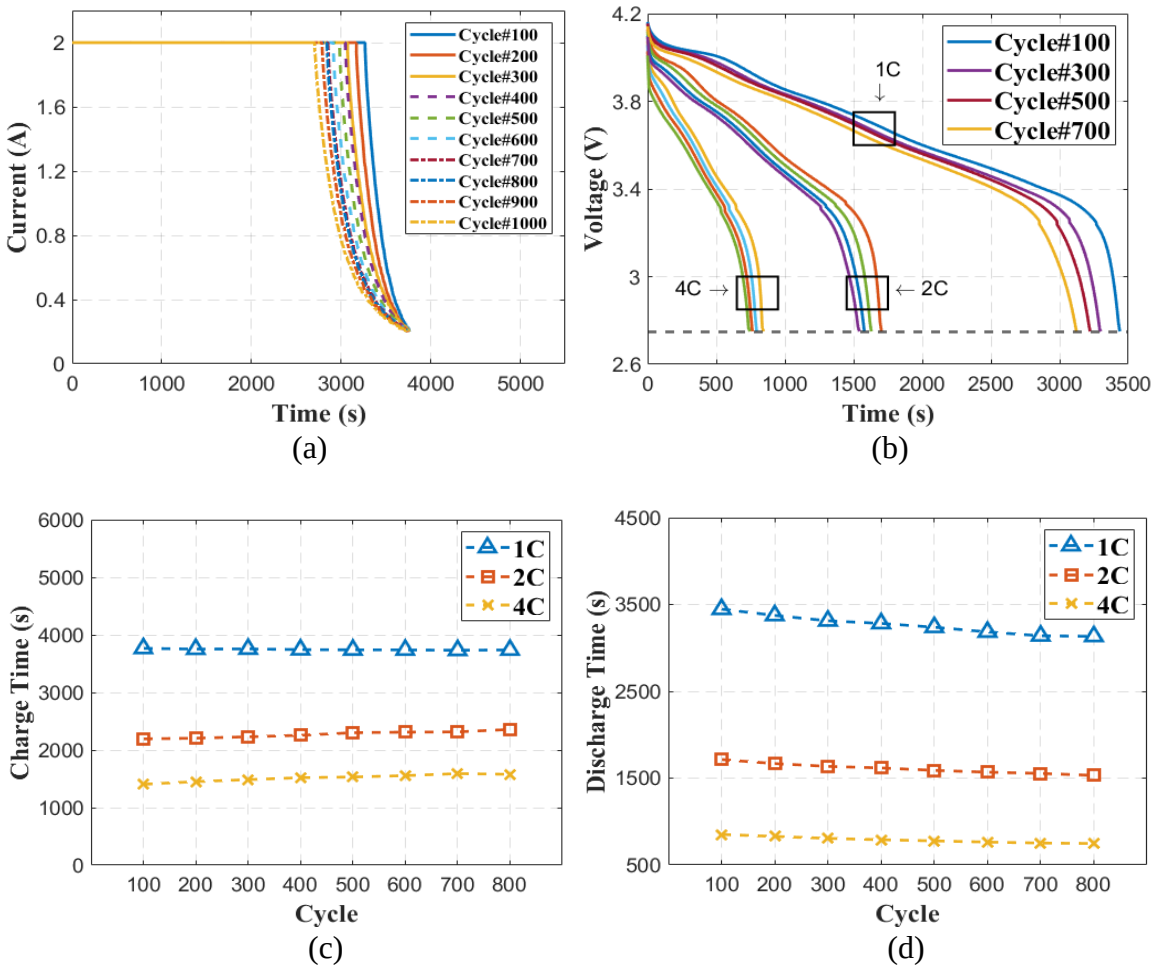

Figure 4.3. Characteristics of different measurements: (a) Charge current vs time at different cycles for cell #2; (b) Discharge voltage vs time at different cycles for all cells; (c) Charge time vs cycles for all cells; (d) Discharge time vs cycles for all cells

4.1.3. Model Development and Results

Peukert's law function [94-95, 97] establishes the connection between the measured discharge capacity and the discharge current. The formula is given in Eq. (4.1), in which $Q_n$denotes the nominal capacity, I denotes the discharge current, t denotes the discharge time, and PC denotes Peukert's law coefficient. This formula can be rewritten by introducing the measured discharge capacity $Q = I * t$ to substitute I in Eq. (4.1). The new formula is given in Eq. (4.2). This

equation reveals that the PC value keeps changing as the battery capacity degrades as well as at different discharge rates. Although the dynamics and variations of PC are displayed by Eq. (4.2), this equation is difficult to be applied for RUL prediction due to a lack of information on the lifecycle. Thus, the connection between the PC value and the number of cycles at different discharge rates needs to be identified.

$$Q_n = I^{PC} * t \tag{4.1}$$

$$Q_n = I^{PC-1} * Q \tag{4.2}$$

It is easily observed that the PC value has different trends for the three cells. As shown in Fig. 4.4, the PC value is calculated by Eq. (4.2) based on the degradation data from 100% to 90%, which keeps increasing as the number of cycles increases. Cell #2 with the 1 C test has the largest PC value at all cycles. If the PC value is a function of the number of cycles, denoted as $f_{PC}(m)$ where m is the number of cycles, the PC value for the future cycles can be predicted. Moreover, the predicted PC values can be used for battery capacity drop prediction, as shown in Eq. (4.3). At last, battery RUL can be predicted in terms of Eq. (4.4), in which Q_{thre} is the capacity at the failure threshold.

$$Q(m) = \frac{Q_n}{I^{f_{PC}(m)-1}} \tag{4.3}$$

$$RUL = \inf\{rul: f_{PC}(rul) \geq \frac{\log\left(\frac{Q_n}{Q_{thre}}\right)}{\log(I)} + 1\} \tag{4.4}$$

Based on the discussion above, two regression models, nonlinear regression and autoregressive, are implemented to fit the PC value based on degradation data from 100% to 90%. The capacity from 90% to 85% will be predicted and results are evaluated by mean absolute error (MAE). As for RUL prediction, a few failure thresholds are selected at different capacity degradation stages. The RUL is defined as the number of cycles when the cell capacity

degrades to the given failure thresholds for the first time. The estimation error in cycle and absolute estimation error in percentage are utilized to evaluate the prediction performance.

4.1.3.1. Nonlinear Regression

The nonlinear regression model [138] has the expression shown in Eq. (4.5), in which $a_1, a_2, a_3, a_4$are coefficients to be estimated. The fitting results provide the R-square of 0.9915, 0.9962, and 0.9979 for three cells, respectively. The estimated coefficients for three cells are $\{1.072, 1.457e-4, -4.262e-2, -6.629e-3\}$, $\{1.076, 4.56e-5, -6.271e-2, -3.466e-3\}$, and $\{1.023, 9.957e-5, -1.509e-2, -8.427e-3\}$.

$$f_{PC}(m) = a_1 * \exp(a_2 m) + a_3 * \exp(a_4 m) \tag{4.5}$$

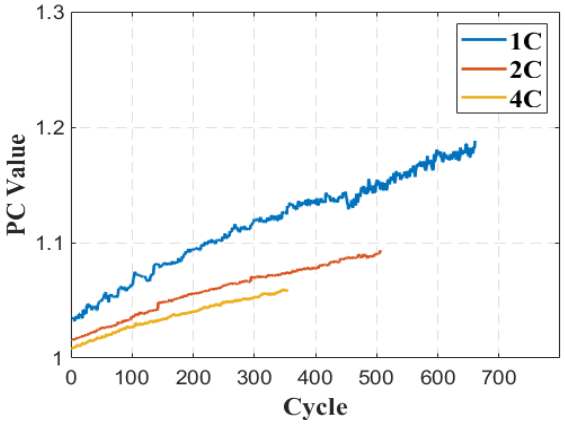

Figure 4.4. PC values vs cycles for all cells.

Fig. 4.5 shows the fitting results where the dashed line represents the estimated PC value. Based on the fitting results, PC values at the degradation stage from 90% to 85% are estimated. Based on Eq. (4.3), the predicted capacity is obtained, and the degradation path is given in Fig. 4.6. The predicted capacity curve for cell #2 accurately describes the true capacity degradation process while the predicted curves for cells #9, and #12 show a slower and a faster degradation path than the true one. Overall, the MAEs for predicted capacity and the true capacity for three cells are 0.0083, 0.0096, and 0.0183, correspondingly.

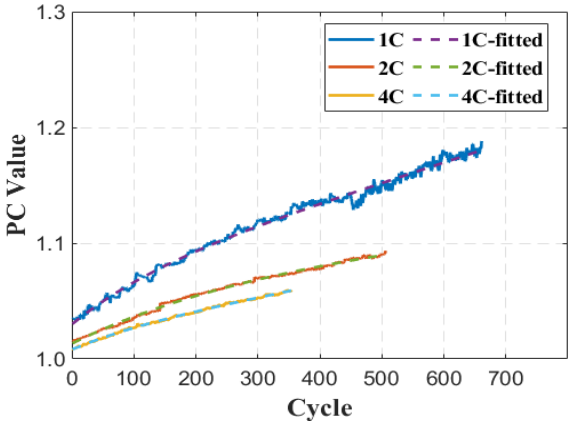

Figure 4.5. Fitted PC value based on nonlinear regression models.

Table 4.1

RUL prediction based on nonlinear regression models

Failure Threshold	Cell #2				Cell #9				Cell #12			
(capacity %)	AR	PR	EC	AP	AR	PR	EC	AP	AR	PR	EC	AP
87.5%	224	265	41	18.30%	230	307	77	33.48%	162	126	-36	22.22%
87.0%	248	311	63	25.40%	275	373	98	35.64%	213	151	-62	29.11%
86.5%	282	357	75	26.60%	318	442	124	38.99%	227	177	-50	22.03%
86.0%	307	403	96	31.27%	367	513	146	39.78%	261	202	-59	22.61%
85.5%	354	449	95	26.84%	426	587	161	37.79%	294	228	-66	22.45%
85.0%	397	494	97	24.43%	491	662	171	34.83%	356	254	-102	28.65%

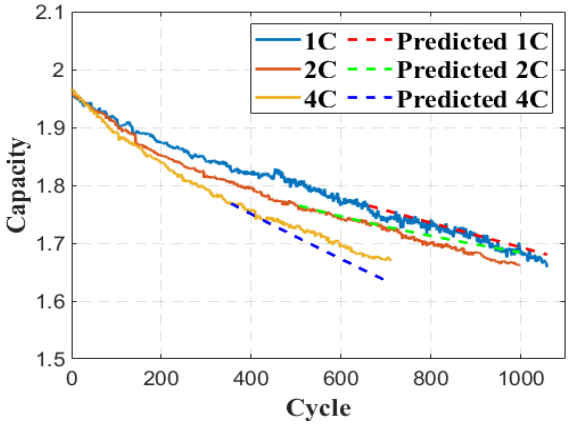

Figure 4.6. Predicted capacity based on nonlinear regression models.

The RUL prediction for three cells is straightforward by looking up the predicted capacity at each cycle. The RUL is the corresponding number of cycles between the capacity at the failure threshold and 90% capacity. The given threshold is a range of capacities from 87.5% to 85% with a reduction of 0.5%. Table 4.1 lists all predicted outcomes. The abbreviations are

used in the table for the following terms, actual RUL (AR), predicted RUL (PR), estimation error in cycle (EC), and absolute estimation error in percentage (AP). Overall, the MAEs for EC in three cells are 77.83, 129.5, and 62.5, the MAEs for AP in three cells are 25.47%, 36.75%, and 24.51%.

4.1.3.2. Autoregressive Model

The autoregressive model [139] has the expression shown in Eq. (4.6), in which $\{PC_{m-1}, \dots, PC_{m-p}\}$ are measurements in the past p time steps, $\{\emptyset_1, \emptyset_2, \dots, \emptyset_p\}$ are associated coefficients, c is a constant, and ε_t is the white noise. To identify the number of orders, p, a set of possible values is assigned for each cell in the model fitting process. Akaike information criterion (AIC) is applied to select the optimal model. Some potential values may provide very closed AIC results, then the autoregressive model that provides the best capacity prediction is considered optimal. Finally, the value of p for each cell is obtained as 19, 5, and 10, accordingly.

$$f_{PC}(m) = c + \emptyset_1 PC_{m-1} + \cdots + \emptyset_p PC_{m-p} + \varepsilon_t \tag{4.6}$$

The predicted capacity based on the estimated PC values from autoregressive models is provided in Fig. 4.7. Similarly, capacity from 90% to 85% is predicted and plotted by the dashed line. All predicted curves overlap with the true degradation curves. Overall, the MAE between the true capacity and predicted capacity for each cell is 0.0051, 0.0058, and 0.005, respectively.

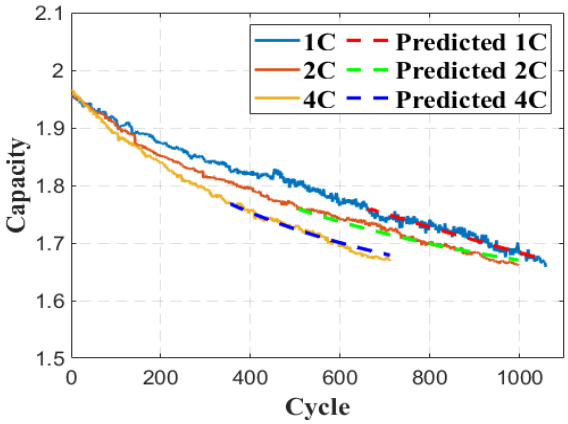

Figure 4.7. Predicted capacity based on autoregressive models.

As for RUL prediction, the same group of capacities ranging from 87.5% to 85% with a 0.5% reduction is given as failure thresholds. Table 4.2 displays the prediction performance with abbreviation for the following terms: actual RUL (AR), predicted RUL (PR), estimation error in cycle (EC), and absolute estimation error in percentage (AP). Overall, the MAEs for EC in three cells are 34.5, 34.83, and 32.83, the MAEs for AP in three cells are 10.60%, 8.67%, and 11.68%. The autoregressive model performs better than the nonlinear regression model in capturing the trend of PC values, and eventually contributes to better RUL prediction results. These results also reveal PC from Peukert's law function can be treated as a time series.

Table 4.2
RUL prediction based on autoregressive models

Failure Threshold	Cell #2				Cell #9				Cell #12			
(capacity %)	AR	PR	EC	AP	AR	PR	EC	AP	AR	PR	EC	AP
87.5%	224	223	-1	0.45%	230	226	-4	1.74%	162	168	6	3.70%
87.0%	248	267	19	7.66%	275	282	7	2.55%	213	209	-4	1.88%
86.5%	282	312	30	10.64%	318	343	25	7.86%	227	253	26	11.45%
86.0%	307	358	51	16.61%	367	409	42	11.44%	261	302	41	15.71%
85.5%	354	405	51	14.41%	426	483	57	13.38%	294	355	61	20.75%
85.0%	397	452	55	13.85%	491	565	74	15.07%	356	415	59	16.57%

4.1.4. Conclusion

This study aims to investigate the lithium-ion battery degradation characteristics at different discharge rates and explore a predictive tool for battery RUL. The dynamics and variations of PC values subject to battery lifecycle and discharge rates were not sufficiently analyzed in the past, which is explored by the nonlinear regression model and autoregression model in this study. By establishing the regression model for each cell separately, the battery RUL can be predicted based on the estimated PC. Overall, the autoregressive model provides a better estimation of PC values to achieve more accurate RUL prediction than the nonlinear regression model. As for future studies, a general model will be applied to describe the variations of PC under all different discharge rates.

4.2. DV Analysis-based Prediction Model

4.2.1. Introduction

The surge in demand for lithium-ion batteries over the past decade can be contributed largely to the popularity of consumer electronics and electrical vehicles [140-141]. For instance, the global sale of electrical vehicles reached around 5.3 million in 2018, and it was predicted to be 56 million by 2040 [142]. Electronic devices usually have different battery sizes to supply various power demands [97]. The battery working loads in real-world applications vary, which require various current rates to meet operation requirements. Especially, a higher current rate can induce significant thermal effects [143] and mechanical stress [144] on the battery electrode, resulting in severe battery degradation and capacity loss compared to lower current rates [111, 145-146]. Thus, predicting battery SOH for batteries considering various current rates is critical for accurately monitoring their health. This not only enhances battery safety and longevity but also improves system management through increased reliability and reduced maintenance costs [135-136, 147].

The use of DV analysis for SOH prediction can be further explored. The batteries are used in wide applications at various current rates. However, current studies [27-28, 101-103] extracted features from DV curves for SOH prediction at one specific current rate. These features may be unavailable or ineffective under other current rates for SOH prediction. In this study, a novel feature, which can be extracted from DV curves at different current rates, is proposed for SOH prediction using statistical methods. The Li-ion battery test is conducted under three different current rates. DV analysis is applied to demonstrate the distinct influences of various current rates on battery capacity degradation behaviors. For the comparison of model performance, three additional groups of features are also extracted from IC analysis [32], charge

voltage curves [148], and cycle number [28] for SOH prediction. The contributions of this paper are summarized as follows:

(1) In-lab experimental testing on Lithium-ion batteries under various current rates.

(2) The influences of current rates on capacity fade are demonstrated by DV analysis.

(3) A novel feature extracted from DV curves at various current rates and used to predict SOH based on statistical methods.

(4) Existing degradation features extracted from IC analysis, charge voltage curve, and cycle number, are used to predict SOH at various current rates based on statistical methods.

(5) Comparison results show a significant improvement in SOH prediction by using the DV curve-based feature.

The rest of this paper is arranged as follows. Section 4.2.2 introduces battery experimental settings and pre-processes for the experimental data. In Section 4.2.3, a new feature is proposed based on DV curves, and a regression model using the novel feature is proposed for SOH prediction. After that, the model based on the novel feature is compared with models using existing groups of features. Finally, a conclusion is given in Section 4.2.4.

4.2.2. Experiments and Data-preprocessing

The Lithium-ion battery cells are manufactured by Samsung (model: 18650 20s), a flat-top battery composed of Li(NiMnCo)O2 cathode and graphite anode. The battery specifications and the battery tests are given in Chapter 3. Based on the experimental setting, different categories of battery output data are collected. The data has been pre-processed and characterized in the following groups, current and voltage versus time profiles for the first cycle, discharge voltage versus capacity in the first cycle, current and voltage at various cycles, and measurements

comparison. Data for cells #2, #9, and #14 tested under 1 C, 2 C, and 4 C are included in this study.

As for the current and voltage profiles for the first cycle, profiles of cells #2 and #9 were originally presented in our previous study [149]. Fig. 4.8 only displays the profile of cell #14. All three cells have similar trends due to similar charge and discharge policies except for different current rates. Moreover, a fast voltage increment is observed when the battery cell starts to get charged, and the increasing rate becomes steady until the start of the CVC phase. An abrupt voltage recovery is recorded at the end of the discharge process, and the voltage stabilizes at a certain level within the rest period. Regarding the total duration of the first cycle, cell #2 takes around 7400 seconds, cell #9 costs around 4200 seconds, and cell #14 takes around 2500 seconds.

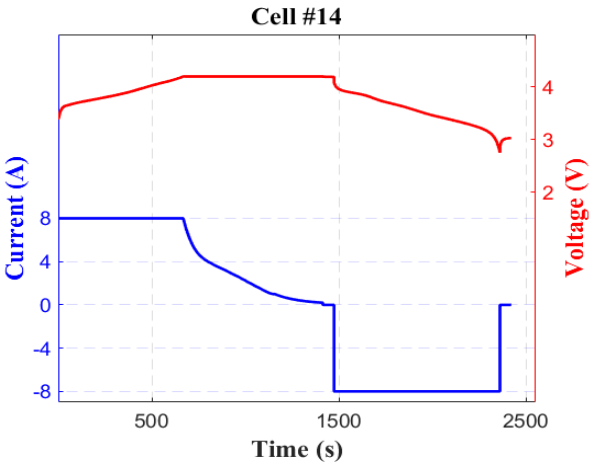

Figure 4.8. Voltage and current profiles of the first cycle for cell #14.

The data of discharge voltage versus released capacity for three battery cells at the first cycle is collected. Cell #2 has the highest voltage drop rate at the end of the discharge process. Cell #14 has the highest voltage drop rate at the beginning of the discharge process. This study considers the measured capacity in the first cycle as the nominal capacity for each cell. Thus, cells #2, #9, and #14 have nominal capacities of 1.95 Ah, 1.96Ah, and 1.97 Ah, accordingly.

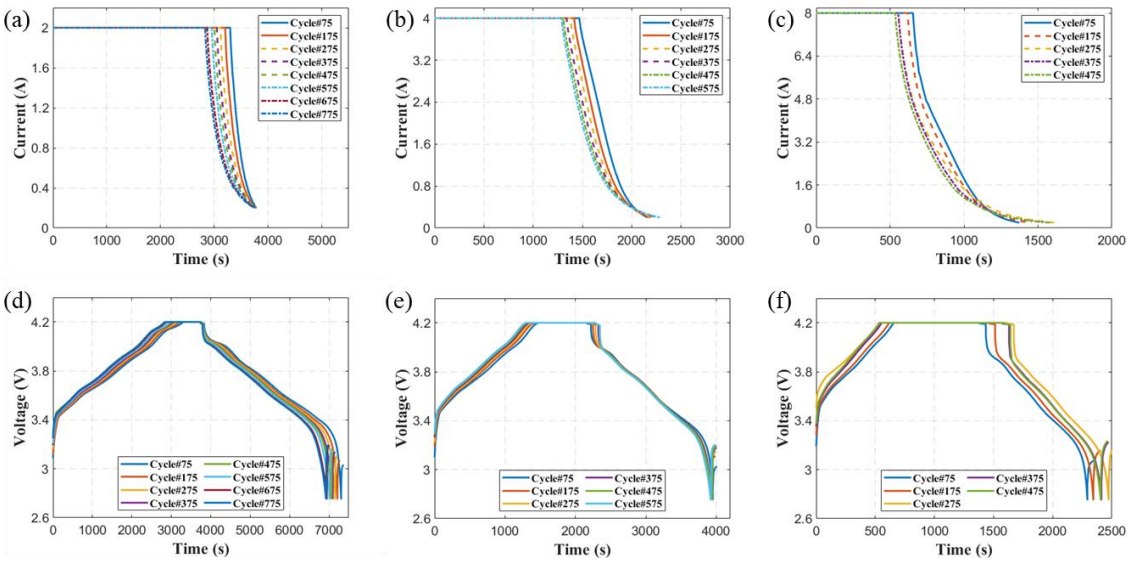

Figure 4.9. Charge process characterization with cycle number: (a) cell #2 current; (b) cell #9 current; (c) cell #14 current; (d) cell #2 voltage; (e) cell #9 voltage; (f) cell #14 voltage.

Fig. 4.9 displays the variations in current curves and voltage curves at different cycles for cells #2, #9, and #14 during the charge process. The current curves include two charge modes, CCC and CVC. As the number of cycles increases, the battery cell takes less time to finish the CCC mode and enters the CVC mode. The total time of the charge process (including CCC and CVC) at later cycles for cells #9 and #14 is slightly larger than that at the early cycles, as shown in Figs. 4.9(b) and (c). On the other hand, Figs. 4.9(d), (e), and (f) demonstrate voltage curves at different cycles. The voltage curve starts to shift left along the time axis as the number of cycles increases for cell #2. Since the total charge time of cells #9 and #14 increases as the number of cycles increases, the voltage curves for these two cells shift right instead of left. Overall, the variations of both charge current and voltage curves show the battery different degradation status at different cycles.

To explore more detailed battery data characteristics, a comprehensive comparison of discharge voltage changes, charge time, and discharge time among different cells is conducted. This comparison was first employed in our previous study [149] for a group of cells. Thus, only

the comparison summary is provided for cells #2, #9, and #14 in this study. Cell #2 has a smooth curve at the beginning of the discharge process and a sharp decline at the end of each cycle. Cell #14 only shows a rapid drop trend at each cycle. The voltage curves drop faster as the number of cycles increases, which is consistent at all cycles for all battery cells. The charge time of cell #2 is almost the same among all cycles, whereas the total charge time of cells #9, and #14 is slightly increasing. Moreover, an obvious decreasing trend can be seen for all cells as the number of cycles increases.

4.2.3. Proposed Model and Results

In this study, the first 10% battery degradation data (from 100% to 90%) is used for model training and the next 5% degradation data (from 90% to 85%) is used for SOH prediction. The corresponding cycle numbers for three battery cells at 90% of initial capacity are 661, 505, and 300, and at 85% of initial capacity are 1058, 997, and 523, respectively.

DV analysis is applied to explore latent information of the battery data in this section. A novel feature is extracted from DV curves for all current rates, and a linear regression model based on the novel feature is proposed. Another three groups of features are extracted from IC curves, charge voltage curves, and cycle number. The goodness-of-fit results of training data are evaluated by the coefficient of determination R^2 and root mean square error (RMSE) [9]. The prediction results based on the novel feature are compared with models using the other three groups of features. The capacity prediction error is calculated at each cycle and the model performance is evaluated by mean absolute error (MAE).

4.2.3.1. DV Curve-based Model

DV curve is calculated from the differentiation of the discharge voltage with respect to capacity, denoted as dV/dQ. Figs. 4.10(a), (b), and (c) display DV curves in the discharge process for three

battery cells. As for each cell, there is a valley at the beginning of the discharge process. The depth of the valley for cell #2 is the deepest among the three cells, while that of cell #14 is the shallowest. The variations of these DV curves show different impacts of current rates on battery degradation. Besides, DV curves increase rapidly at the end of the discharge process, and these increments occur earlier as the number of cycles increases. The variations of DV curves at the end of the discharge process are significant, which can be potentially linked to battery capacity degradation.

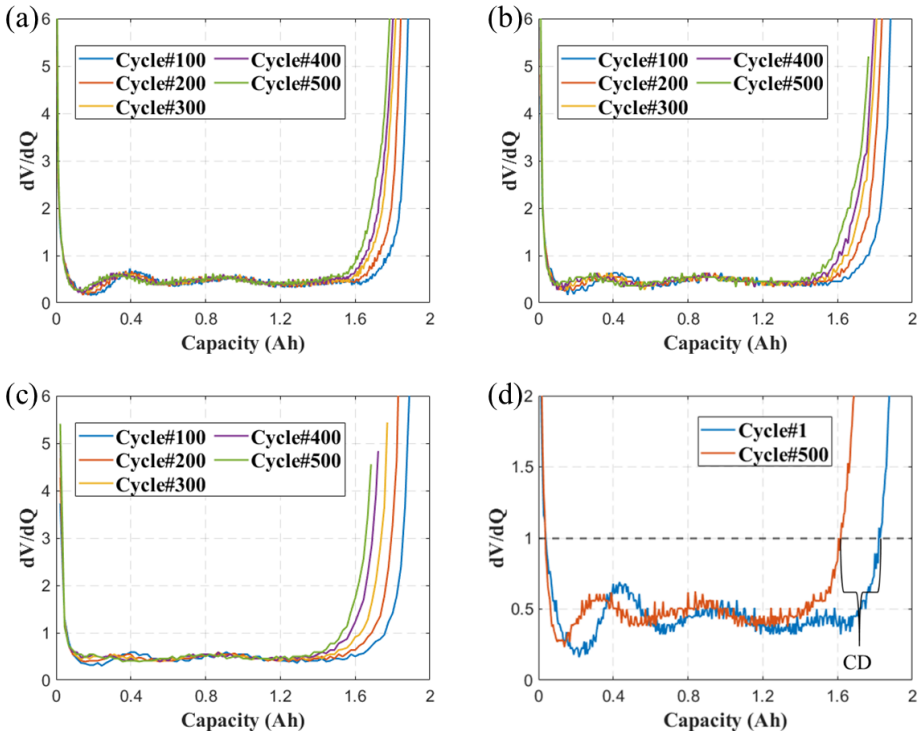

Figure 4.10. DV curves and extracted feature: (a) DV curves for cell #2; (b) DV curves for cell #9; (c) DV curves for cell #14; (d) Extracted features at cycle #500 for cell #2 from DV curves.

A novel feature is extracted from the DV curves at the end of the discharge process, in which large variations are seen among different cycles. A horizontal line with a value of 1, denoted as $dV/dQ = 1$, is used as the reference line. The feature is the capacity difference (CD) between the current curve and the curve at the first cycle crossing the reference line. Fig. 4.10(d) shows an example of the feature at cycle #500 for cell #2.

Then, the regression model is proposed: $SOH = a_1 CD + a_2$, in which a_1, a_2 are corresponding parameters. Table 4.3 presents estimated parameters and goodness-of-fit results based on training data, demonstrates that this model achieves a low RMSE across all cells. The predicted SOH curves for these cells are displayed in Fig. 4.11 with MAEs of 0.0018, 0.0025, and 0.0031, respectively.

Table 4.3

Model fitting coefficients and goodness-of-fit based on the DV curve feature of training data

	a_1	a_2	R^2	RMSE
Cell #2	-0.3752	0.9971	0.9963	0.0017
Cell #9	-0.3781	0.9977	0.9910	0.0027
Cell #14	-0.4613	1.0070	0.9815	0.0039

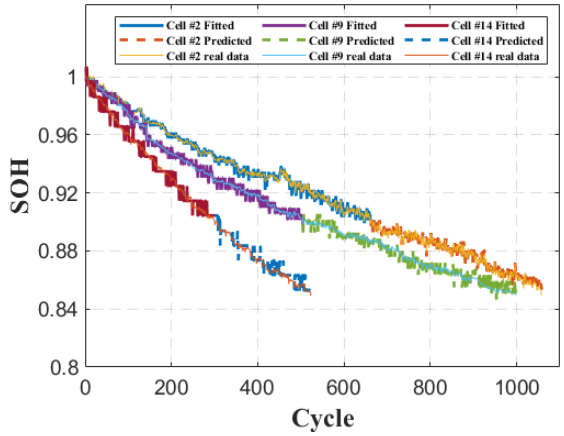

Figure 4.11. SOH prediction based on the DV curve feature: (a) cell #2; (b) cell #9; (c) cell #14.

4.2.3.2. IC Curve-based Model

IC curve is calculated from the differentiation of capacity with respect to the discharge voltage, denoted as dQ/dV. Figs. 4.12(a), (b), and (c) show the IC curves in the discharge process for all three battery cells. To link IC values to the battery discharge degrees, the X-axis of voltage is replaced by SOC instead, where SOC represents the current energy stored inside the battery. Gaussian filter [26] is applied to reduce the variability of IC curves via smoothing. It can replace each data point with a weighted average of its neighbors. Hence, the nearest data points have

more impact on the average and the distant data points only play a smaller role. There are two important parameters in the filter, one is the mean u, another is the standard deviation σ. The mean is usually set as 0 to ensure each data point has the largest influence on itself, and the standard deviation controls the window size to determine how smooth the curve is. A small σ may cause undesirable smoothing effects while a large σ may cause information loss and curve deformation. In this study, the value of σ is set as 3, and the window size is given as 5.

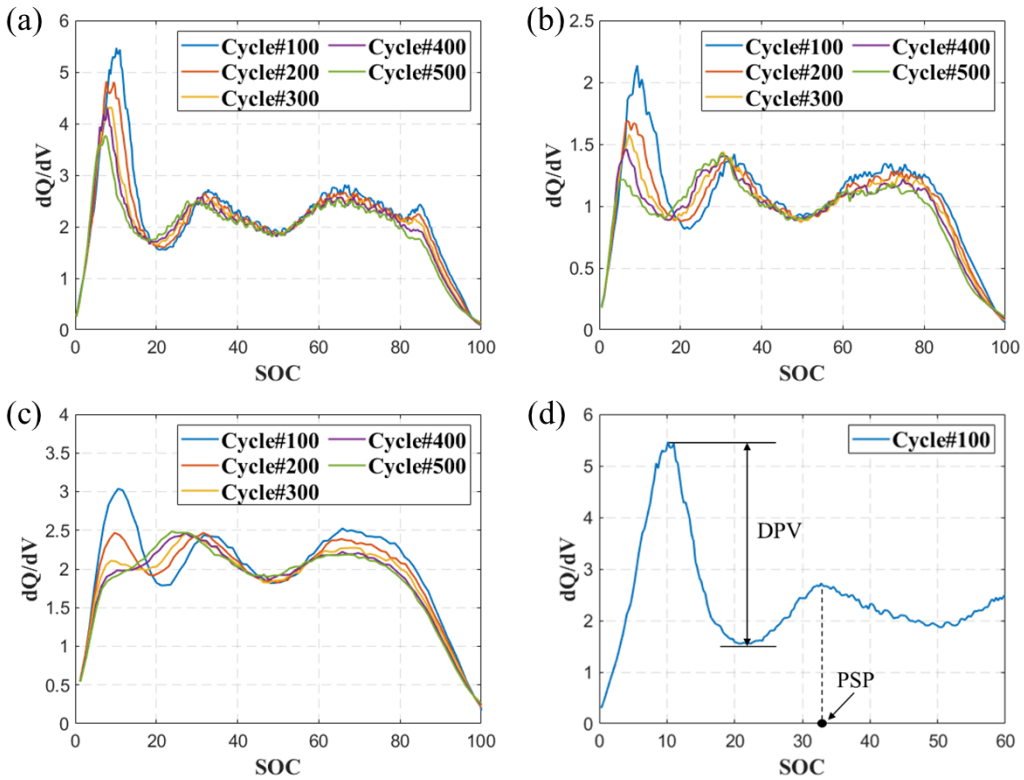

Figure 4.12. IC curves and extracted features: (a) IC curves for cell #2; (b) IC curves for cell #9; (c) IC curves for cell #14; (d) Extracted features at cycle #100 for cell #2 from the IC curve.

The IC curves exhibit different numbers of peaks and valleys at different current rates, yet the first two peaks and the first valley contain critical information. For example, as the number of cycles increases, the height of the first peak decreases and the depth of the first valley increases. Also, the position of the second peak shifts towards the left with the cycle number increasing. Thus, two features are extracted, the first is the vertical distance between the first

peak and valley, denoted as DPV, and the second is the position of the second peak, denoted as PSP [32].

Fig. 4.12(d) displays an example of extracted features for cell #2 at the 100th cycle. Then, the linear regression is formulated as $SOH = b_1 DPV + b_2 PSP + b_3$, in which b_1, b_2, b_3 are parameters to be estimated. Table 4.4 gives the estimated coefficients for all battery cells and goodness-of-fit results based on training data. The predicted SOH curves for these cells are shown in Fig. 4.13, with MAEs of 0.0027, 0.0055, and 0.0171, respectively. The predicted curves of cells #2 and #9 follow the trends of the real SOH drop curves, but the predicted curve of cell #14 does not capture the trend.

Table 4.4

Model fitting coefficients and goodness-of-fit based on the IC curve features of training data

	b_1	b_2	b_3	R^2	RMSE
Cell #2	0.0264	-0.7167	1.0870	0.9757	0.0042
Cell #9	-0.0003	-1.6090	1.9050	0.9993	0.0008
Cell #14	0.0329	-0.2491	1.2090	0.9910	0.0027

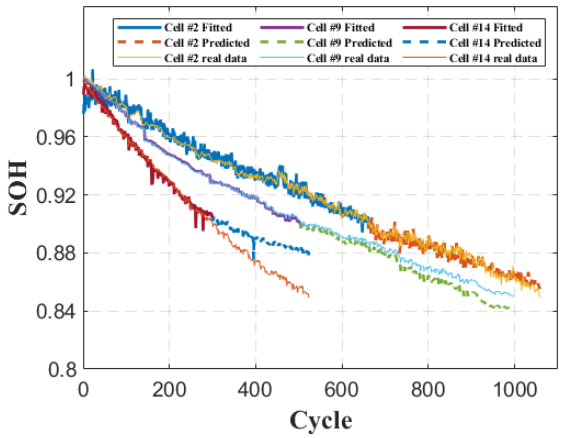

Figure 4.13. SOH prediction based on IC curve features: (a) cell #2; (b) cell #9; (c) cell #14.

4.2.3.3. Charge Voltage-based Model

The charge voltage keeps increasing in the battery charge process, and the charge voltage curves are different at different cycles. As shown in Figs. 4.9(d), (e), and (f), the charge voltage curves

for cell #2 shift left as the number of cycles increases while the charge voltage curves for cells #9 and #14 shift right. All cells take less time to finish the CCC as the number of cycles increases. In other words, as the battery ages, the charge time of the CVC mode constitutes a larger portion of the overall charge process. Besides, the areas covered by the CCC and CVC curves change with the cycle number. Considering the variations of the above observations at different cycles, two features [148] are extracted from the charge voltage curves to represent the battery degradation status: the time ratio (TR), which is the ratio of the period of CCC to CVC, and the covered area ratio (AR), which is the ratio of area covered by CCC to CVC.

The SOH prediction model based on TR and AR is expressed as $SOH = c_1\,TR + c_2 AR + c_3$, in which c_1, c_2, c_3 are corresponding parameters. The estimated coefficients and goodness-of-fit results are listed in Table 4.5. The fitting results show high RMSEs for all battery cells for training data, which shows that the model does not fit the data very well. Typically, the model fitting performance is extremely poor for cells at high current rates, such as cells #9 and #14. The performance of the SOH prediction model is evaluated by MAE for these cells, which are 0.0052, 0.0165, and 0.0227, respectively.

Table 4.5
Model fitting coefficients based on voltage features and goodness-of-fit of training data

	c_1	c_2	c_3	R^2	RMSE
Cell #2	0.4793	0.0146	0.4881	0.9799	0.0039
Cell #9	-0.5290	0.2109	0.9546	0.9525	0.0063
Cell #14	-0.0890	0.2532	0.8017	0.9506	0.0063

4.2.3.4. Cycle Number-based Model

The cycle number is a direct indicator of the battery aging, and therefore it can be linked to SOH. A linear regression model can be set up. The cycle number [28] is selected as the only independent variable. The SOH prediction model is expressed as $SOH = d_1\,CN + d_2$, in which

CN is cycle number, and d_1 and d_2 denote corresponding parameters. The model coefficients and goodness-of-fit results for three battery cells #2, #9, and #14 of training data are listed in Table 4.6. The model prediction performance is calculated by MAE for these cells, which are 0.0075, 0.0289, and 0.0124, respectively.

Table 4.6
Model fitting coefficients and goodness-of-fit based on cycle number of training data

	d_1	d_2	R^2	RMSE
Cell #2	-0.0001	0.9918	0.9756	0.0042
Cell #9	-0.0002	0.9923	0.9714	0.0049
Cell #14	-0.0003	0.9945	0.9947	0.0021

4.2.3.5. SOH Prediction Results Comparison

To assess the model performance based on distinct groups of features, MAE is applied to calculate the prediction error of each model for each battery cell, and the results are displayed in Table 4.7. Moreover, the average MAE is provided to demonstrate the overall model performance across all battery cells. The performances of the cycle number-based model and charge voltage-based model are close but poor. The DV curve-based model has a smaller average MAE than the IC curve-based model, and therefore it is the most accurate SOH prediction model among all groups.

Table 4.7
Model prediction performance comparison based on MAE.

Model	MAE			Average MAE
	Cell #2	Cell #9	Cell #14	
Cycle number-based model	0.0075	0.0289	0.0124	0.0163
Charge voltage-based model	0.0052	0.0165	0.0227	0.0148
IC curve-based model	0.0027	0.0055	0.0171	0.0084
DV curve-based model	0.0018	0.0025	0.0031	0.0025

4.2.4. Discussion and Conclusion

The accurate SOH prediction relies on highly correlated features, and the feature selection is determined by specific criteria. In this section, the Pearson correlation test [150] is conducted to

assess the correlation between selected features and SOH. Features from the above four models are listed as CN, TR, AR, DPV, PSP, and CD. The correlation coefficients show all features are highly correlated to SOH with values greater than 0.95.

To further investigate the reason that feature CD extracted from DV curves performs the best among all features. The figure of feature values versus number of cycles is provided. Because the IC curve-based model and DV curve-based model provide small prediction errors, the relevant features, DPV, PSP, and CD are selected for further investigation. In Figs. 4.14(a), (b), and (c), CD has a linear increasing trend for all cells. Although fluctuations are seen in all three lines, the increasing trend is obvious. Since the DV-based model is a linear regression model, the linearity of CD feature contributes to the accurate prediction results.

On the other hand, DPV has a decreasing trend for all cells, but the decreasing rate becomes almost zero in the prediction phase for cells #9 and #14, as shown in Figs. 4.14(e), and (f). Similarly, POTSP includes a few noises to prevent good prediction results, for example, frequent fluctuation is seen in Fig. 4.14(g), and a few abrupt increments are observed in Fig. 4.14(i). The IC curve-based model cannot recognize such pattern changes in features which leads to deficient performance.

Applying the Gaussian filter for IC curves is another reason the IC curve-based model did not outperform the DV curve-based model. Because the parameter selection of the Gaussian filter is based on experience, the smoothing of initial IC curves brings possible curve deformation and loss of important degradation information. The IC curve-based model does not learn well with a filtered dataset. Meanwhile, DV curves include the original information, and features are directly extracted for model fitting and prediction. Overall, the DV curve-based

model achieves the best prediction performance among all models. CD, a novel feature extracted from DV curves, is the most effective for SOH prediction at different current rates.

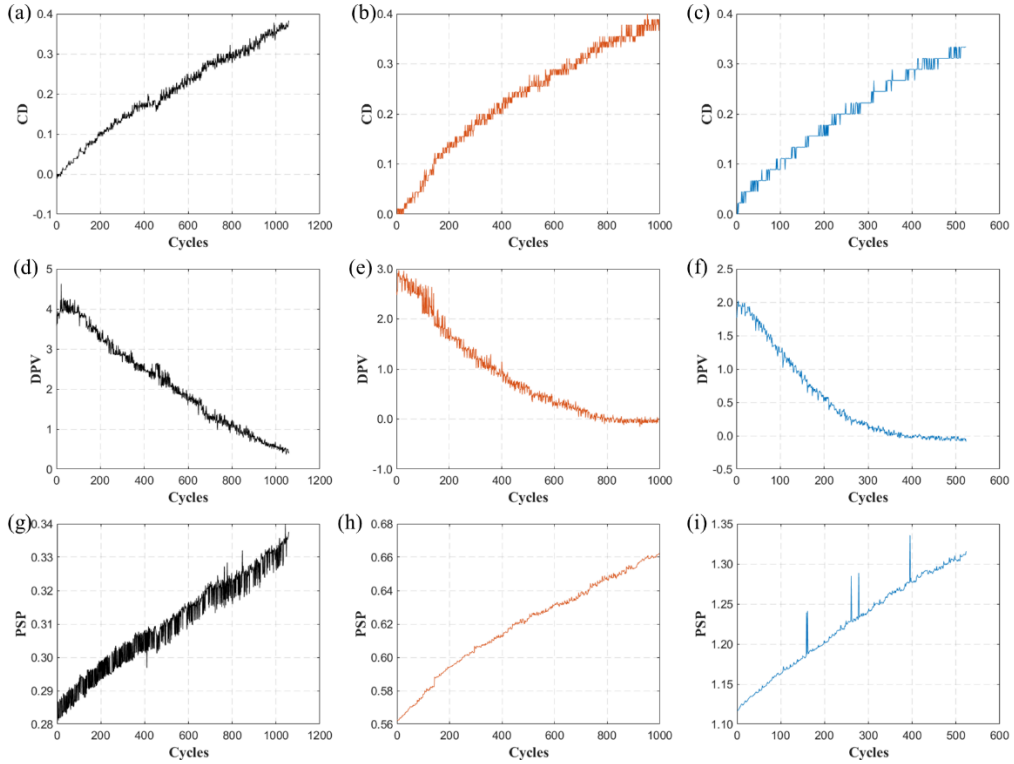

Figure 4.14. Extracted features for different cells: (a) CD for cell #2; (b) CD for cell #9; (c) CD for cell #14; (d) DPV for cell #2; (e) DPV for cell #9; (f) DPV for cell #14; (g) PSP for cell #2; (h) PSP for cell #9; (i) PSP for cell #14.

This study aims to investigate the influences of different current rates on lithium-ion battery degradation behaviors, demonstrate different battery degradation characteristics, and extract a novel feature from DV analysis for SOH prediction at different current rates. An SOH prediction model based on the novel feature is proposed and the model performance is compared with other models using features extracted from IC curves, charge voltage curves, and cycle number. The proposed SOH prediction model with the novel feature shows the best prediction accuracy. As for future study, other battery operation conditions affecting battery degradation will be investigated from the experiment.

CHAPTER 5

5. Lithium-ion Battery Remaining Useful Life Prediction Using A Two-phase Degradation Model with A Dynamic Change Point

5.1. Introduction

An accurate remaining useful life (RUL) prediction plays a crucial role in the prognostics and health management of lithium-ion (Li-ion) batteries. Current studies [19-20, 34-35] on the RUL prediction of Li-ion batteries commonly use single-phase degradation models, which result in inaccurate RUL predictions due to their insufficient capabilities in capturing various degradation patterns. The existing two-phase degradation models [36-38] can divide battery degradation into two phases using a change point, a slowly decreasing phase, and a rapidly decreasing phase.

The change point in the current two-phase degradation models [36-38] is usually modeled in two ways. First, the change point is treated as a random variable, which increases the computational complexity. Second, the change point is treated as a fixed value, which may not be practical due to model simplicity. For example, as seen in Fig. 5.1, the degradation data collected from the experimental tests on Li-ion battery cells strongly supports a two-phase degradation pattern with a dynamic change point, which is different for different battery cells.

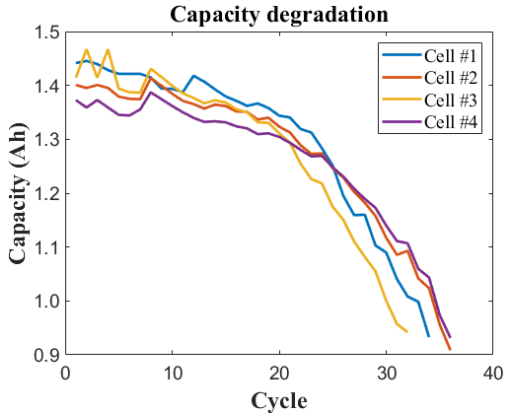

Figure 5.1. Four Li-ion battery cells capacity degradation behaviors from lab experiments.

In addition, variations have been observed in the degradation behaviors of tested battery cells, which could be caused by manufacturing process, measurement, and process noise. Thus, an RUL prediction framework that integrates a two-phase capacity degradation model with a dynamic change point and uncertainties is needed for accurate battery prognostics and health management.

The main contributions of this article are listed as follows.

(1) The binary segmentation [151] is utilized to identify a dynamic change point for separating the battery degradation data into two different phases, in which the detected change point varies for different battery cells.

(2) A two-phase capacity degradation model with a dynamic change point is proposed, which can better capture the battery degradation patterns at both early and later degradation stages.

(3) A particle filtering-based framework incorporating uncertainties is proposed to update coefficients of the proposed two-phase capacity degradation model, generate particles for posterior distribution approximation, and further predict the RULs of battery cells.

(4) The proposed particle filtering-based RUL prediction framework with the two-phase capacity degradation model shows superior performance compared with the existing capacity degradation models using the battery degradation data in the lab and NASA battery data [129].

This chapter is organized as follows. Section 5.2 proposes a two-phase capacity degradation model with a dynamic change point. Section 5.3 addresses the uncertainties in the proposed capacity degradation model and develops a particle filtering-based framework incorporating the two-phase capacity degradation model to update model coefficients and further predict the RULs of battery cells. Section 5.4 includes three subsections. The first subsection

describes the experimental test design in the lab and the collected battery degradation data. The second subsection displays the identified change point for laboratory data and compares the goodness-of-fit for the proposed model with a dynamic change point to the proposed model with fixed change points. Then, the estimated coefficients of the proposed model are displayed, and the goodness-of-fit for the proposed model is compared to other degradation models. Further, the results of RUL predictions of the laboratory data based on the proposed particle filtering-based framework with the two-phase capacity degradation model are displayed and compared with the existing models. The third subsection presents the description of the NASA dataset [129] and then the NASA battery cells RUL prediction results and comparison. Section 5.5 concludes this study and discusses the future direction.

5.2. Battery Capacity Degradation Model Development

The proposed two-phase capacity degradation model consists of two distinct functions to describe two different battery degradation patterns. The logarithm function, as the inverse of the exponential function [6, 19], has a concave shape to be considered in developing the proposed model. However, using one-term or two-term logarithm functions may not be capable of capturing the capacity degradation trend. In addition, the collected degradation data (see Fig. 5.1) show the degradation pattern can be divided into two phases with a dynamic change point. Thus, in the first phase, a logarithm function with a quadratic polynomial function is proposed to describe the capacity trend. In the second phase, two logarithm functions and a quadratic polynomial function are integrated. The proposed two-phase capacity degradation model with a dynamic change point can be formulated as follows:

$$G(x) = \begin{cases} a_1 + a_2 \log(a_3 x + a_4) + a_5 x^2 & , \ x < k \\ b_1 + b_2 \log(b_3 x + b_4) + b_5 \log(b_6 x + b_7) + b_8 x^2, & x \geq k \end{cases} \tag{5.1}$$

where k is the change point of the capacity degradation process of a battery cell, which is unknown and needs to be determined. x denotes the number of cycles. $G(x)$ represents the estimated capacity in terms of x. $\mathbf{a} = [a_1, a_2, a_3, a_4, a_5]$ is the set of coefficients for the first phase degradation model, which is the first function in Eq. (5.1). $\mathbf{b} = [b_1, b_2, b_3, b_4, b_5, b_6, b_7, b_8]$ is the set of coefficients for the second phase degradation model, which is the second function in Eq. (5.1). The values in sets **a** and **b** can be completely distinct because the two degradation models are fitted based on data from different phases.

The change point, *k*, plays a critical role in Eq. (5.1) because it determines when to transit from the first phase to the second phase. In addition, the change point k also splits the data into two phases. The estimated coefficients of degradation functions in Eq. (5.1) thus vary with *k*. Moreover, the RUL prediction accuracy can be affected by the coefficients. Hence, it is important to determine the value of k for accurate prediction. Binary segmentation is utilized, which is a computationally efficient algorithm, to detect and identify the change point of a battery cell [151]. The point k is identified as the change point if a dataset can find a point k to satisfy the constraint in:

$$C(y_{1:k}) + C\left(y_{(k+1):n}\right) + \beta < C(y_{1:n}) \tag{5.2}$$

where $y_{1:n}$ represents the data from the first point to the n^{th} point, $C(\cdot)$ is a statistical cost function, for example, mean, standard deviation, and likelihood. Parameter β is a penalty term, which can prevent overfitting. According to the study [151], the value of β is equivalent to $2p$, in which p represents the number of parameters introduced by adding a change point. In this study, the proposed two-phase capacity degradation model has different forms of degradation functions in these two phases, so it is not reasonable to determine the value of p. The built-in function in MATLAB can detect change points to minimize the left part of Eq. (5.2) when the maximum

number of change points is given. In this study, the maximum number of change points is set as one.

The binary segmentation method can detect the change point not only in the situation where all degradation data are available but also for battery cells in use. As for battery cells in use, limited cycles of battery degradation data are collected, and new degradation data becomes available when the battery cells move to the next charge and discharge cycle. In this case, the binary segmentation method, as shown in Eq. (5.2), can determine the change point to separate the current degradation path into two phases. If the binary segmentation does not provide a change point, it indicates the current degradation data has only one phase. The first phase degradation model with the best results for goodness-of-fit is selected to describe the battery degradation patterns. If the binary segmentation can detect a change point, the current degradation path can be separated into two phases. The detected change point may vary at first but will be steady as more degradation data becomes available. In addition, in case the change point has more than one value, the performance of the goodness-of-fit will be evaluated for the two-phase capacity degradation model with different values of the change point. The value that can provide the best results for the goodness-of-fit is the change point for real-time battery data.

5.3. Particle Filtering-based RUL Prediction Framework

5.3.1. Particle Filtering

In this study, the inconsistencies of capacity degradation trends are observed among four Li-ion battery cells. First, four battery cells show different change points. Besides, the degradation rates of the tested four battery cells are different. The sources of these variations are stated as follows [19]. (1) Due to uncertainties in manufacturing processes and materials properties, batteries may have different initial capacity values. (2) Due to the measurement noise of the calibration units of

the battery tester, the measured capacity can be slightly different from the true capacity. (3) Due to process noise, the coefficients of the proposed model evolve during the degradation process. The estimated coefficients keep changing if new degradation data is obtained.

Particle filtering is utilized to model the uncertainties, which is an algorithm based on Bayesian inference and uses Monte Carlo Simulation to draw weighted random particles from an arbitrary distribution to approximate the posterior distribution. The Bayesian inference includes the state function and the measurement function, which are formulated as:

$$\mathbf{b}^i = f\left(\mathbf{b}^{i-1}\right) + \boldsymbol{\omega}_\mathbf{b} \tag{5.3}$$

$$Y^i = h\left(\mathbf{b}^i\right) + v_Y \tag{5.4}$$

where $\mathbf{b}^i$ is the state vector of estimated coefficients for the second phase degradation model at the i^{th} cycle, and Y^i is the measured battery capacity at the i^{th} cycle. $f(\cdot)$ is the state function that describes the evolution of the state vector over cycles. $h\,(\cdot)$ is the measurement function, which is equivalent to the second phase degradation model of $G(x)$. $\boldsymbol{\omega}_\mathbf{b}$ and v_Y are process noise and measurement noise [6, 36, 110]. As for the process noise $\boldsymbol{\omega}_\mathbf{b}$, Brownian motion is used [152] to model the differences between coefficients from two consecutive charge and discharge cycles. As for the measurement noise v_Y, Brownian motion is also used to model the difference between the measured capacity and the estimated capacity from the proposed two-phase capacity degradation model.

To verify the normality assumption of the process noise, the estimated coefficients of all battery cells at the i^{th} and $(i-1)^{th}$ cycles are obtained to calculate the differences. Similarly, the differences between the estimated capacity and the measured capacity of all four Li-ion battery cells are computed. Jarque-Bera test [153] is utilized to verify the normality of these differences by assessing the skewness and kurtosis of the sample data to match a normal

distribution. Based on the test results, both the process noise and the measurement noise follow normal distributions, which validate my assumptions that use Brownian motion to model these two types of noises.

Using the Bayesian inference process to estimate $\mathbf{b}^i$ is widely applied in many studies [154-155]. It is assumed that the probability density function (PDF) of the initial state of $\mathbf{b}^i$ is available and not dependent on the measured capacity and the variables in $\mathbf{b}^i$ follows the first-order Markov process, which indicates the state vector $\mathbf{b}^i$ can be updated only based on the previous state vector $\mathbf{b}^{i-1}$ without the knowledge of Y^i. The posterior PDF $p(\mathbf{b}^i|Y^{0:i})$ can be obtained by recursively executing two steps, prediction, given in Eq. (5.5), and update, given in Eq. (5.6). Given the PDF $p(\mathbf{b}^{i-1}|Y^{0:i-1})$, the prior PDF $p(\mathbf{b}^i|Y^{0:i-1})$ can be obtained for the prediction step by using the Chapman–Kolmogorov equation. Further, when a measurement Y^i is available, the posterior PDF $p(\mathbf{b}^i|Y^{0:i})$ can be updated in the update step.

$$p(\mathbf{b}^i|Y^{0:i-1}) = \int p(\mathbf{b}^i|\mathbf{b}^{i-1})p(\mathbf{b}^{i-1}|Y^{0:i-1})\, d\mathbf{b}^{i-1} \tag{5.5}$$

$$p(\mathbf{b}^i|Y^{0:i}) = \frac{p(Y^i|\mathbf{b}^i)P(\mathbf{b}^i|Y^{0:i-1})}{p(Y^i|Y^{0:i-1})} \tag{5.6}$$

where $p(Y^i|Y^{0:i-1})$ is the normalized constant, in which $p(Y^i|Y^{0:i-1}) = \int p(Y^i|\mathbf{b}^i)p(\mathbf{b}^i|Y^{0:i-1})\, d\mathbf{b}^i$. The Bayesian estimation shows a conceptual solution to obtain the posterior distribution, but in practice, it is difficult to solve multidimensional integrals. Thus, Monte Carlo simulation is used to assign multiple weighted particles to approximate the posterior distribution. The approximation formula of posterior PDF [6, 19] is written as:

$$P(\mathbf{b}^i|Y^{0:i}) \approx \sum_{m=1}^{M} w^{i,m}\delta(\Delta\mathbf{b}^m) \tag{5.7}$$

where M is assigned as 500 to represent the total number of random points [36] in this study, $\delta(\cdot)$ is dirac delta function with $\Delta\mathbf{b}^m = \mathbf{b}^i - \mathbf{b}^{i,m}$, $\mathbf{b}^{i,m}$ is the m^{th} set of coefficients obtained from random particles at the i^{th} cycle, and $w^{i,m}$ is the weight associated with $\mathbf{b}^{i,m}$.

The weights are used to describe the importance of the random particles, in which the posterior distribution is determined by particles with large weights. The associated weights $w^{i,m}$ can be updated and normalized before being updated in the next cycle. The weights updating function is given below:

$$w^{i,m} = w^{i-1,m}\frac{p(Y^i|\mathbf{b}^{i,m})p(\mathbf{b}^{i,m}|\mathbf{b}^{i-1,m})}{\varphi(\mathbf{b}^{i,m}|\mathbf{b}^{i-1,m}, Y^{0:i})} \tag{5.8}$$

The randomly chosen distribution $\varphi(\mathbf{b}^{i,m}|\mathbf{b}^{i-1,m}, Y^{0:i})$ can generate random particles based on current coefficients and measured capacity data. The generated particles will be utilized to update the mean and variance of the chosen distribution for the next cycle. If $\varphi(\mathbf{b}^{i,m}|\mathbf{b}^{i-1,m}, Y^{0:i}) = p(\mathbf{b}^{i,m}|\mathbf{b}^{i-1,m})$, Eq. (5.8) can be simplified as $w^{i,m} = w^{i-1,m}p\left(Y^i\middle|\mathbf{b}^{i,m}\right)$. The weights for the next cycle are determined by previous weights and the likelihood function $p(Y^i|\mathbf{b}^{i,m})$. The likelihood function is equivalent to the probability obtained from the distribution for the estimated capacity errors, which is calculated in terms of the current random particles. A large probability occurs if the capacity estimation error is small. After several iterations of particle updating, the degeneracy phenomenon can happen [156], in which some weights of particles become extremely large and other weights are close to zero. To mitigate the degeneracy and save computational efforts, the multinomial resampling method [156] is utilized to keep particles with large weights and kill negligible particles.

5.3.2. Proposed RUL Prediction Framework with Degradation Model Using Particle Filtering Method

In this section, we use degradation data from the second phase for updating weights of random particles. The state vector at the i^{th} cycle is $\mathbf{b}^i = \left[b_1^i, b_2^i, b_3^i, b_4^i, b_5^i, b_6^i, b_7^i, b_8^i\right]$. The state function is given as $f(\mathbf{b}^{i-1}) = \mathbf{b}^{i-1}$ so that $\mathbf{b}^{\boldsymbol{i}}$ equals the summation of $\mathbf{b}^{i-1}$ and a normally distributed error term $\boldsymbol{\omega_B}$. The measurement function $h(\mathbf{b}^i)$ is changed to be the second phase degradation model of $G(x)$ for the given $\mathbf{b}^i$. RUL prediction is conducted for all four battery cells. As for each battery, the initial coefficients are obtained from the curve fitting results based on the second phase degradation model (Eq. (5.1)), which is $\mathbf{b}^0 = [b_1^0, b_2^0, b_3^0, b_4^0, b_5^0, b_6^0, b_7^0, b_8^0]$. Thus, the capacity Y^i at the i^{th} cycle can be expressed as:

$$Y^i = \sum_{m=1}^{M} w^{i,m}\left[b_1^{i,m} + b_2^{i,m}\log\left(b_3^{i,m}\cdot i + b_4^{i,m}\right) + b_5^{i,m} log\left(b_6^{i,m}\cdot i + b_7^{i,m}\right) + b_8^{i,m}\cdot i^2\right] \quad (5.9)$$

Then, the h-cycle ahead predicted capacity based on the i^{th} cycle, denoted as Y^{i+h}, can be formulated as:

$$Y^{i+h} = \sum_{m=1}^{M} w^{i,m}\left[b_1^{i,m} + b_2^{i,m}\log\left(b_3^{i,m}(i+h) + b_4^{i,m}\right) + b_5^{i,m}\log\left(b_6^{i,m}(i+h) + b_7^{i,m}\right) + b_8^{i,m}(i+h)^2\right] \quad (5.10)$$

To predict the RULs of battery cells, the failure threshold is first set up, which is usually 60% - 80% of a battery cell's initial capacity [6, 19]. In this study, the failure threshold for laboratory batteries is set as 70% of battery initial capacities. Let Y^0 be the initial capacity measured by the battery tester. The predicted RUL at the i^{th} cycle based on the m^{th} set of random particles, denoted as $RUL^{i,m}$, can be solved using the following equation.

$$0.7Y^0 = b_1^{i,m} + b_2^{i,m} log(b_3^{i,m}(i + RUL^{i,m}) + b_4^{i,m}) + b_5^{i,m} log(b_6^{i,m}(i + RUL^{i,m}) + b_7^{i,m}) + b_8^{i,m}(i + RUL^{i,m})^2 \quad (5.11)$$

Further, the expectation of RUL at the i^{th} cycle, denoted as RUL^i, is shown in Eq. (5.12), and the estimated PDF of RUL at the i^{th} cycle, denoted as $p(RUL^i|Y^i)$, shown in Eq. (5.13), where $\Delta RUL^{i,m} = RUL^i - RUL^{i,m}$.

$$RUL^i = \sum_{m=1}^{M} w^{i,m} RUL^{i,m} \tag{5.12}$$

$$p\left(RUL^i \middle| Y^i\right) \approx \sum_{m=1}^{M} w^{i,m}\, \delta\left(\Delta RUL^{i,m}\right) \tag{5.13}$$

Summating the procedures described above, Fig. 5.2 describes the proposed RUL prediction framework based on the proposed two-phase capacity degradation model using particle filtering method. The change points for battery cells are first determined based on Eq. (5.2) to establish two-phase degradation models. Then, state and measurement functions are built in terms of Eqs. (5.3) and (5.4). Coefficients of the degradation model are sampled by random particles and their weights are updated recursively where *j* is the total number of measurements and i is the current updating cycle. The particle filtering algorithm keeps updating all parameters in the second phase degradation model until all available degradation data is used. Then, RUL and the PDF of RUL are calculated based on Eq. (5.12) and (5.13).

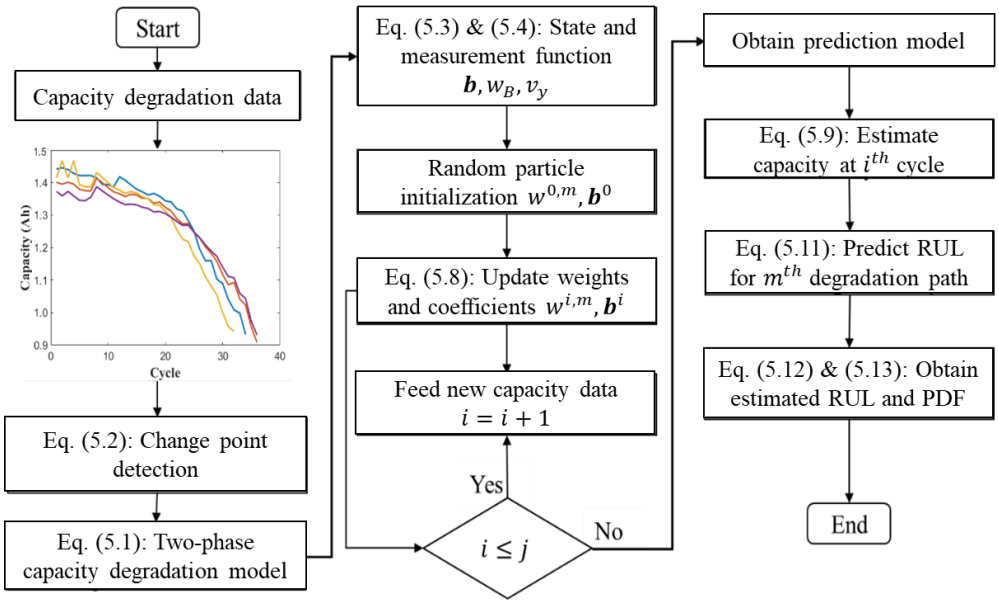

Figure 5.2. The RUL prediction framework based on the proposed two-phase capacity degradation model using particle filtering method.

Note that in general the first phase degradation model is used to describe the degradation trend at the early stage while the second phase degradation model is applied for RUL prediction because batteries usually move to the second phase before the capacity drops too low, as seen in Fig. 5.1. Thus, the degradation data from the second phase is used to predict RUL in the proposed RUL prediction framework. There are also cases in which some batteries stay in a steady degradation status for most of their lifetimes and move to a fast degradation phase after a certain point [36]. For example, if the change point is below the defined failure threshold, in this case, the degradation data from the first phase is used to predict RUL based on the proposed RUL prediction framework.

5.4. Results and Discussion

5.4.1. Experiments and Data Collection

The battery test platform in the lab, shown in Chapter 3, consists of battery testers and a monitoring computer. The battery tester is composed of multiple built-in circuits that can conduct all types of battery tests, such as CCC, CCD, and CVC. The battery tester allows two types of battery connections so that the tested battery cells can be linked by the cell or wire channels.

In this study, the cylindrical battery cells produced by EBL are applied for battery capacity tests. The specifications for the tested battery cells are given in Chapter 3. For each cycle, tests under CCC and CCD with 1.25 C rate (2 A) are conducted at 25°C ambient temperature. The cut-off voltages for the charge and discharge process are 4.25V and 2.75V, respectively. The battery cells are rested for one minute between each charge and discharge cycle. The rest time can be varied depending on the design of the experiment. For example, study [43] applied a rest time of 30 minutes for 1 C charge and discharge battery tests at 25°C ambient

temperature while study [125] used a rest time of 10 minutes for 0.5 C charge and 3 C discharge battery tests at 30°C ambient temperature. In this study, the accelerated battery degradation data needs to be obtained so that the rest time is set as one minute. Similar experimental settings can be found in studies [131, 157]. For example, study [157] applied batteries with a nominal capacity of 3.05 Ah and set the rest time as 1 minute for each charge and discharge cycle. The batteries were charged at 1/3 C in each cycle and discharged at 1 C for 30 cycles and 4 C for another 40 cycles. On the other hand, the rest time of 1 minute simulates Li-ion battery practical applications. For instance, battery cells in electric vehicles can be charged and discharged randomly (e.g., no rest time).

The battery tester automatically calculates the capacity by taking the integration of the current over time. As seen in Fig. 5.1, there exist fluctuations in capacity, particularly for cells #2-4 at the early stage of testing. Such capacity fluctuations are caused by the capacity regeneration phenomenon [158]. Moreover, due to the higher charge/discharge current rate, the quality of the commercial battery cells, and the short rest time that limits the residual reactions between the electrodes and electrolyte to provide more capacity for the next cycles, the capacities of all battery cells drop below 70% of their initial capacities after 35 cycles. The degradation rates of battery cells under such settings may be much faster than in experiments conducted in other studies. Thus, the data collected in the lab have a relatively smaller size compared with other studies.

The charge and discharge curves with time (seconds) of four battery cells are displayed in Figs. 5.3(a)-(d). Although the nominal capacity from the manufacturer is 1.6 Ah, the laboratory data shows the discharge capacity for the first cycle is around 1.4 Ah for all four cells. Thus, in

this study, the initial capacity for each battery is the measured discharge capacity at the beginning of testing.

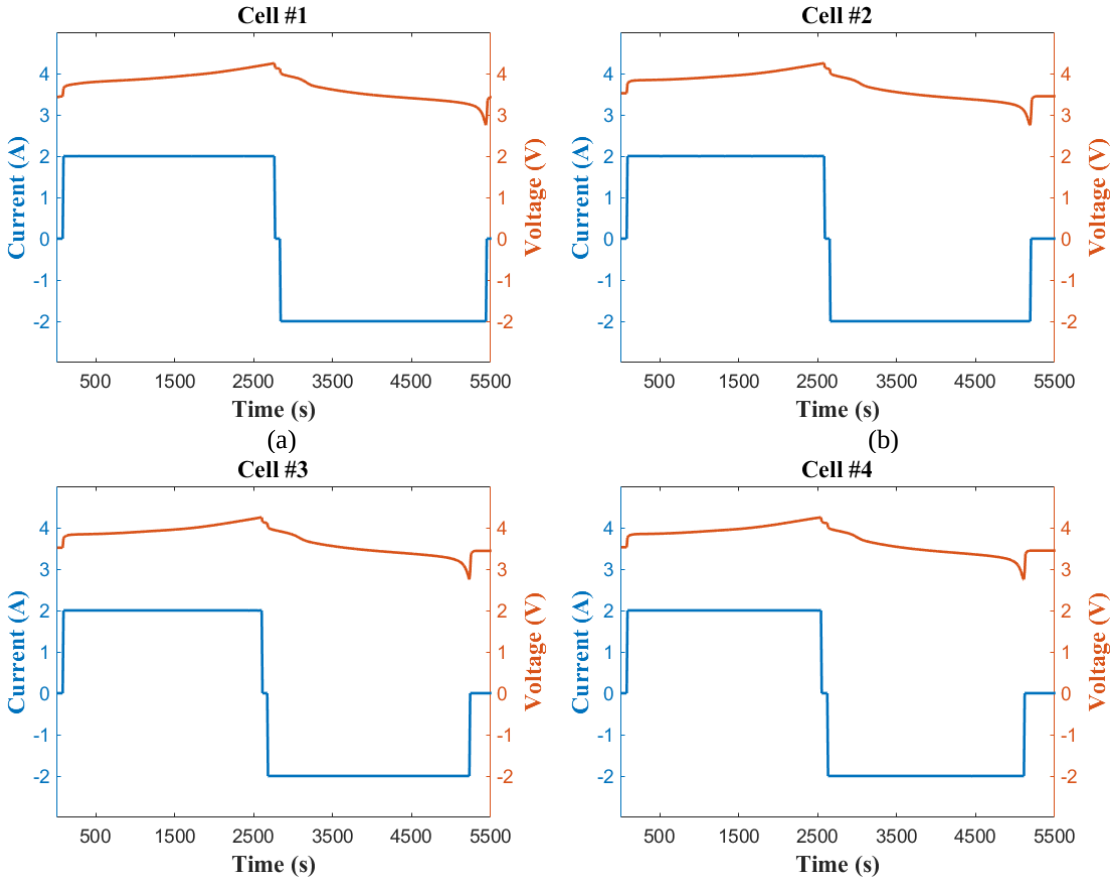

Figure 5.3. Profiles of voltage and current in charge and discharge processes for four cells: (a) cell #1; (b) cell #2; (c) cell #3; (d) cell #4.

To show the trend of the capacity released in the battery discharging process, as an example, the capacity released data every 300 seconds for different discharge cycles of battery cell #1 is present for Cycle 1, Cycle 10, Cycle 20, and Cycle 30, in Table 5.1. Because the measured capacity is the integration of discharge current in terms of the testing time, thus the capacity released in Table 5.1 is listed in ascending order for each cycle. The number in the last row for each cycle represents the specific time when the battery cell is fully discharged, and the total released capacity. Overall, the capacity of a battery cell will decrease as the number of

testing cycles increases, which means less time will be required to fully discharge a cell under CCD compared with early testing cycles.

Table 5.1
Capacity released for different cycles of battery cell #1

Cycle #1		Cycle #10		Cycle #20		Cycle #30	
Time (Seconds)	Capacity released (Ah)	Time (Seconds)	Capacity released (Ah)	Time (Seconds)	Capacity released (Ah)	Time (Seconds)	Capacity released (Ah)
0	0	0	0	0	0	0	0
300	0.167	300	0.167	300	0.167	300	0.167
600	0.333	600	0.333	600	0.333	600	0.333
900	0.500	900	0.500	900	0.500	900	0.500
1200	0.667	1200	0.667	1200	0.667	1200	0.667
1500	0.833	1500	0.833	1500	0.833	1500	0.833
1800	1.000	1800	1.000	1800	1.000	1800	1.000
2100	1.167	2100	1.167	2100	1.167	1962	1.090
2400	1.333	2400	1.333	2400	1.333	-	-
2595	1.442	2509	1.394	2419	1.344	-	-

5.4.2. Laboratory Data RUL Prediction and Evaluation

5.4.2.1. Change Point Identification

The cycle life of a battery cell is defined as the number of cycles that a battery cell degrades from 100% to 70% of the initial capacity for the laboratory data. The cycles of life for battery cells #1-4 are 31, 34, 30, and 35, respectively. The numbers of cycles for battery cells #1-4 degrading from 100% to 80% of the initial capacity are 29, 29, 28, and 32, respectively.

To show the effectiveness of binary segmentation for obtaining good fitting accuracy of the proposed model via dynamic change points, as an example, two fixed change points, $k = 10 \text{ and } 15$, are selected to compare the goodness-of-fit statistics for the proposed model using root mean square error (RMSE) and coefficient of determination, R^2. As seen in Table 5.2, the proposed model with the dynamic change point provides the smallest RMSE and largest R^2 compared with the fixed change points for all battery cells. Thus, the proposed model with a

dynamic change point can better capture battery degradation trends compared with degradation models with a fixed change point.

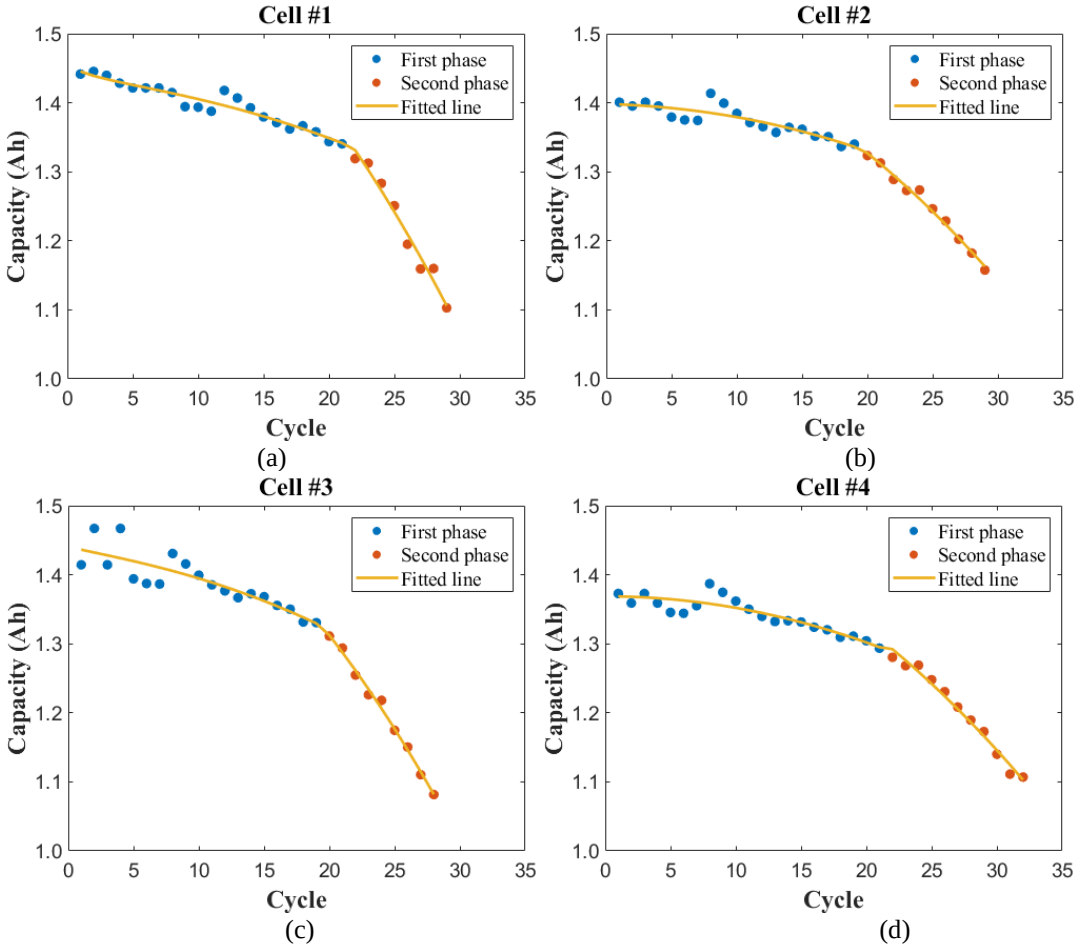

Figure 5.4. Fittings of two-phase capacity degradation model with a change point: (a) cell #1; (b) cell #2; (c) cell #3; (d) cell #4.

Table 5.2

Comparison of the goodness-of-fit for the proposed two-phase capacity degradation model with dynamic and fixed change points

Proposed degradation model with fixed and dynamic change points	RMSE				R^2			
	Cell #1	Cell #2	Cell #3	Cell #4	Cell #1	Cell #2	Cell #3	Cell #4
Fixed change point ($k = 10$)	0.023	0.013	0.023	0.015	0.937	0.963	0.951	0.965
Fixed change point ($k = 15$)	0.018	0.011	0.018	0.013	0.960	0.977	0.969	0.971
Dynamic change point	0.010	0.010	0.016	0.003	0.989	0.991	0.980	0.990

Based on the binary segmentation, the change points of battery cells #1-4 are 22, 20, 20, and 22, respectively. The fitted capacity degradation curves for all battery cells are displayed in

Figs. 5.4(a)-(d) to show the capacity degradation from 100% to 80%. In Figs. 5.4(a)–(d), each battery cell has a two-phase degradation behavior that is determined by the proposed model. As for each battery cell, the degradation rate in the first phase is small but becomes large in the second phase.

5.4.2.2. Proposed Degradation Model Goodness-of-fit Evaluation and Comparison

The goodness-of-fit statistics are employed to assess the fitting accuracy of the proposed two-phase degradation model. Table 5.3 displays all estimated coefficients of the first phase degradation model for battery cells #1-4 and the corresponding RMSE and R^2. The first phase degradation model has a good fitting performance according to RMSE and R^2. Similarly, the goodness-of-fit for the second phase degradation model is displayed in Table 5.4, which proves the second phase degradation model also fits the data well.

Table 5.3
The coefficients estimation and goodness-of-fit of the first phase degradation model for laboratory data

Cell No.	a_1	a_2	a_3	a_4	a_5	RMSE	R^2
1	1.485	-0.014	7.768	7.559	-1.57e-4	0.010	0.925
2	1.399	-5.49e-4	8.810	29.010	-1.72e-4	0.012	0.823
3	1.463	-0.025	0.437	2.508	-2.06e-4	0.022	0.743
4	1.372	-8.41e-7	0.527	2.892	-1.84e-4	0.012	0.879

Table 5.4
The coefficients estimation and goodness-of-fit of the second phase degradation model for laboratory data

Cell No.	b_1	b_2	b_3	b_4	b_5	b_6	b_7	b_8	RMSE	R^2
1	1.672	-0.013	0.250	0.499	-0.014	0.700	0.899	-5.83e-4	0.039	0.975
2	1.551	-0.012	0.250	0.433	-0.013	0.700	1.068	-3.96e-4	0.016	0.986
3	1.559	-0.013	0.249	0.500	-0.014	0.705	0.899	-5.70e-4	0.014	0.995
4	1.548	-0.012	0.250	0.451	-0.013	0.700	1.023	-3.77e-4	0.011	0.993

The fitting results of the proposed model are compared with existing capacity degradation models based on RMSE and R^2. The overall RMSE and R^2 of the proposed model is calculated

based on the goodness-of-fit statistics of the first and second phase degradation models. Four models are selected for comparison, the one-term exponential model [20], denoted as model 1, the two-term exponential model [19], denoted as model 2, the ensemble model [35], denoted as model 3, and the sigmoidal model [159], denoted as model 4. Comparison results are shown in Table 5.5. The RMSE value of the proposed model is the smallest among all models for all cells. The R^2 value is the largest among all models for all cells. Thus, the proposed model fits the degradation trend best among all battery degradation models above.

Table 5.5
Comparison of the goodness-of-fit among battery capacity degradation models

Battery capacity degradation model	RMSE				R^2			
	Cell #1	Cell #2	Cell #3	Cell #4	Cell #1	Cell #2	Cell #3	Cell #4
Model 1 [20]	0.048	0.047	0.049	0.043	0.785	0.807	0.819	0.805
Model 2 [19]	0.014	0.011	0.018	0.010	0.983	0.990	0.976	0.989
Model 3 [35]	0.013	0.012	0.018	0.020	0.985	0.989	0.977	0.963
Model 4 [159]	0.015	0.010	0.017	0.011	0.975	0.982	0.974	0.978
Proposed model	0.010	0.010	0.016	0.003	0.989	0.991	0.980	0.990

5.4.2.3. RUL Prediction and Comparison for Laboratory Data

For the laboratory data, RUL of a battery cell is defined as the remaining number of charge and discharge cycles until the capacity reaches the failure threshold (70% of initial capacity). Thus, the true RULs of battery cells #1-4 are 2, 5, 2, and 3 cycles. In this section, the RULs of battery cells #1-4 are predicted based on the framework proposed in Section 5.3. Estimation error of cycles and absolute estimation error percentage are two metrics utilized to measure prediction accuracy [6, 36].

The prediction results of RULs of battery cells #1-4 based on the proposed framework are displayed in Figs. 5.5(a)-(d). Taking Fig. 5.5(a) as an example, the solid red line and dashed red line respectively represent the first and the second phase of the degradation paths, while the yellow dots indicate the true capacity degradation data after 80% capacity. The particle update

paths shown as blue lines display all possible degradation paths until the failure threshold (70% of the cell's initial capacity). Using the proposed RUL prediction framework in Section 5.3, the predicted RULs (in cycles) of four cells are 2, 7, 2, and 5, respectively.

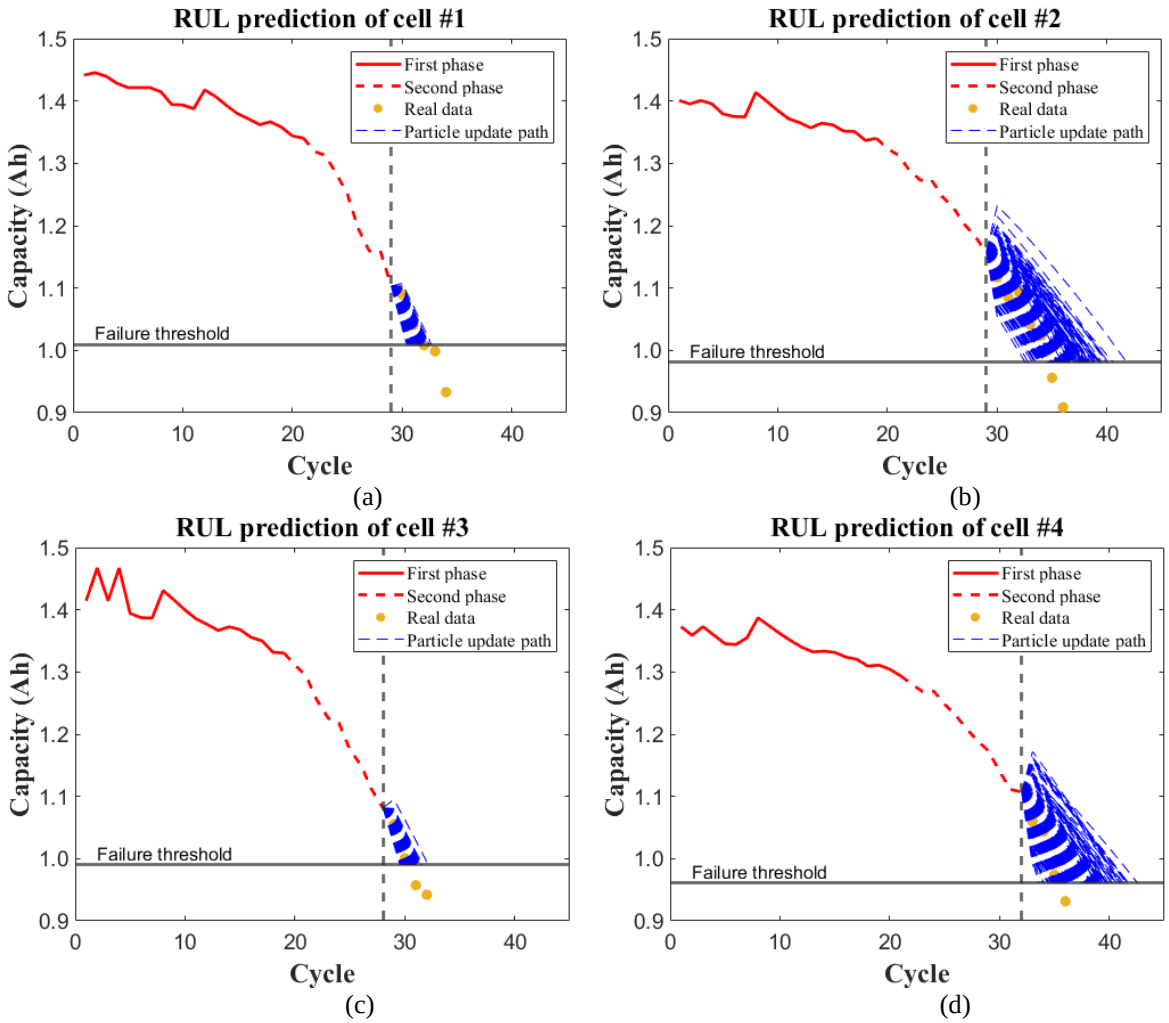

Figure 5.5. RUL prediction for laboratory data: (a) cell #1; (b) cell #2; (c) cell #3; (d) cell #4.

Because the RUL prediction of cell #1 is equivalent to the true RUL of cell #1, in this case, the estimation error of cycles is zero. Similarly, the estimation error of cycles for cell #2 is 2 and the absolute estimation error percentage is 40%. As for cell #3, the estimation error of cycles is 0. As for cell #4, the estimation error of cycles is 2 and the absolute estimation error percentage is 67%. The average absolute estimation error percentage for cells #1-4 based on the

proposed framework is 27%. The 95% confidence intervals of predicted RULs for all four battery cells are [1.7, 3.2], [4.4, 10.7], [1.8, 3.5], and [2.2, 8.7], respectively.

The RUL prediction results of the proposed framework are compared with the existing battery degradation models using the particle filtering method, and the comparison results are displayed in Tables 5.6 and 5.7. The one-term exponential model (model 1) [20] is not included in the comparison because it shows poor fitting in capturing the nonlinear capacity degradation trends for all battery cells. In addition, the proposed model with a fixed change point for RUL prediction is not considered because the goodness-of-fit is worse than that of the proposed model with a dynamic change point. As for the two-term exponential model (model 2) [19] with particle filtering, the predicted RULs of four cells are 1, 4, 1, and 3 cycles, respectively, which indicates the estimation errors of cycles are -1, -1, -1, and 0, accordingly. The absolute estimation error percentages for four cells are 50%, 20%, 50%, and 0%, respectively, and the average absolute estimation error percentage is 30%. As for the ensemble model (model 3) [35] with particle filtering, the predicted RULs of four cells are also 1, 4, 1, and 3 cycles, and the estimation errors of cycles are -1, -1, -1, and 0, respectively. The absolute estimation error percentages for four battery cells are 50%, 20%, 50%, and 0%, which also provides an average absolute estimation error percentage of 30%. As for the sigmoidal model (model 4) [159] with particle filtering, the predicted RULs of four cells are 3, 6, 2, and 6, which indicates the estimation errors of cycles are 1, 1, 0, and 3, respectively. The absolute estimation error percentages for four battery cells are 50%, 20%, 0%, and 100%, which provides an average absolute estimation error percentage of 43%. Based on the comparison results, the proposed framework achieves the best accuracy in predicting battery RULs among all models.

Table 5.6
Comparison of cell #1-2 RUL prediction among different degradation models with particle filtering for laboratory data

RUL prediction framework	Actual RUL		Predicted RUL		Estimation error (Cycle)		Absolute estimation error (%)	
	Cell #1	Cell #2	Cell #1	Cell #2	Cell #1	Cell #2	Cell #1	Cell #2
Model 2 [19] with particle filtering	2	5	1	4	-1	-1	50%	20%
Model 3 [35] with particle filtering	2	5	1	4	-1	-1	50%	20%
Model 4 [159] with particle filtering	2	5	3	6	1	1	50%	20%
Proposed framework	2	5	2	7	0	2	0%	40%

Table 5.7
Comparison of cell #3-4 RUL prediction among different degradation models with particle filtering for laboratory data

RUL prediction framework	Actual RUL		Predicted RUL		Estimation error (Cycle)		Absolute estimation error (%)	
	Cell #3	Cell #4	Cell #3	Cell #4	Cell #3	Cell #4	Cell #3	Cell #4
Model 2 [19] with particle filtering	2	3	1	3	-1	0	50%	0%
Model 3 [35] with particle filtering	2	3	1	3	-1	0	50%	0%
Model 4 [159] with particle filtering	2	3	2	6	0	3	0%	100%
Proposed framework	2	3	2	5	0	2	0%	67%

The reasons that the proposed framework outperforms the other models are as follows. First, the goodness-of-fit results from the proposed two-phase degradation model show a relatively low RMSE and a high R^2 compared with other degradation models, which indicates the proposed two-phase degradation model is more accurate in describing the nonlinear battery degradation patterns. Second, the proposed two-phase degradation model has two independent regression functions to fit the slow degradation phase and the sharp degradation phase. If new data is given, the second phase degradation model can directly capture the degradation trend without affecting the fitted model in the first phase. As for other models, the trade-off between

the overall fitting performance and the real degradation trends occurs, which may lead to poor estimation.

5.4.3. NASA Data RUL Prediction and Comparison

5.4.3.1. Description of Dataset

The battery data labeled “B0005” and “B0007” is selected from NASA's Prognostics Center of Excellence [129] to validate the proposed RUL prediction framework. The capacities of both battery cells are 2 Ah. The dataset recorded three operation modes (discharge, charge, and impedance test) at ambient temperature. The charge process was conducted under CCC mode at 1.5 A (0.75 C) until the battery voltage increased to 4.2 V and under CVC mode until the current dropped to 20 mA. The discharge process for two battery cells was carried out in CCD mode at 2 A (1 C) until the voltage dropped to 2.7 V and 2.2 V, respectively.

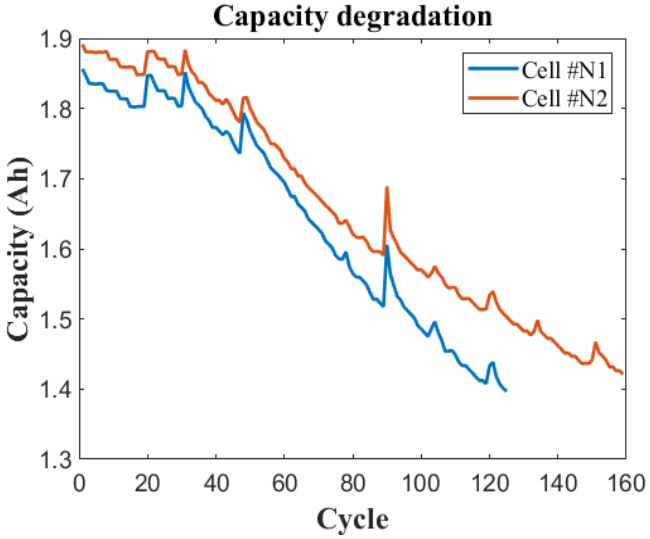

Figure 5.6. Battery degradation behaviors from NASA data repository [129].

The discharge capacity data of both battery cells are extracted to visualize the degradation patterns, as seen in Fig. 5.6. For simplicity, cells #N1 and #N2 are used to label the selected battery cells “B0005” and “B0007”. Overall, cell #N1 takes 125 cycles to degrade to 75% capacity while battery cell #N2 takes 159 cycles. During the first few cycles, both battery

cells have a steadily slow degradation rate. Then, both cells move to fast degradation phases and degrade to 80% of their initial capacities, in which the number of cycles is 100 and 123 cycles, respectively. All pulses shown in Fig. 5.6 during the degradation process for both battery cells are related to capacity regeneration [158].

5.4.3.2. RUL Prediction and Comparison for NASA Data

Based on the binary segmentation, change points for cells #N1 and #N2 are obtained, which are 31 and 56 cycles. The proposed model with dynamic change point is evaluated to be the best model for RUL prediction for the laboratory data, thus in this section, the proposed model with dynamic change point is utilized to predict RULs for NASA data. For NASA data, the RUL of both battery cells is defined as the remaining number of charge and discharge cycles until the capacity drops to a certain threshold (75% of their initial capacities). The RULs of battery cells are predicted based on the proposed framework in Section 5.3 using battery capacity data ranging from 80 % - 100% of their initial capacities. The true RULs of cells #N1 and #N2 are 25 and 36 cycles. Similarly, the estimation error of cycles and absolute estimation error of percentage are utilized to assess prediction accuracy [6, 36].

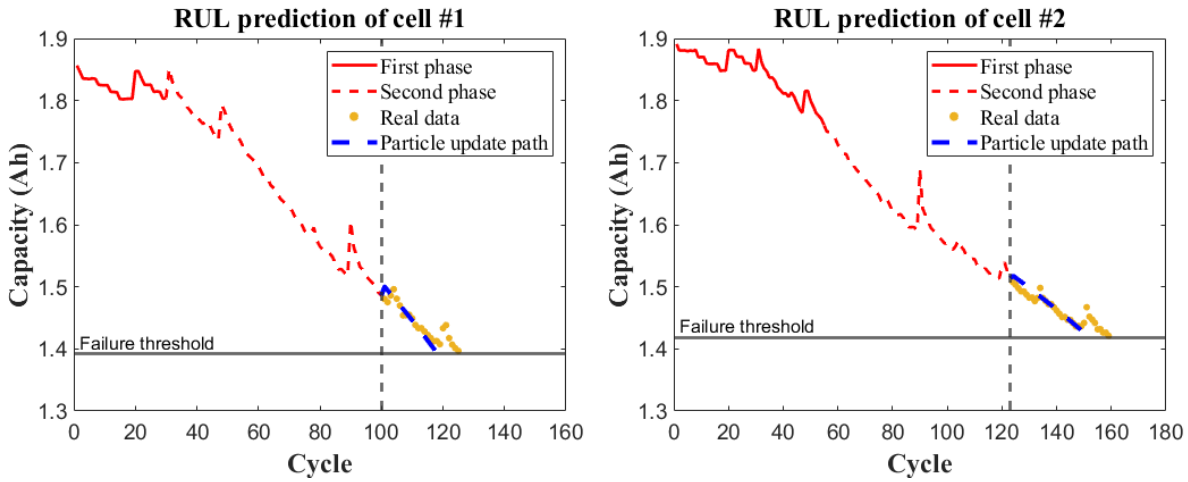

(a) (b)

Figure 5.7. RUL prediction for NASA data: (a) cell #N1; (b) cell #N2.

The results of RUL predictions for cells #N1 and #N2 are obtained and displayed in Figs. 5.7(a)-(b). The solid and dashed red lines represent the first and the second phases of the degradation paths, while the yellow dots indicate the true capacity degradation data after 80% capacity. The predicted RUL of cell #N1 is 18 cycles so the estimation error of cycles is -7 cycles, and the absolute estimation error percentage is 28%. The predicted RUL of cell #N2 is 29 cycles so the estimation error of cycles is -7 cycles, and the absolute estimation error percentage is 19%. The average absolute estimation error percentage for cells # N1 and N2 based on the proposed framework is 24%. The 95% confidence intervals of the predicted RULs for both battery cells are very small because the coefficients from different sets in particle filtering are updated to very similar values. The potential degradation paths overlap with each other in both Figs. 5.7(a)-(b).

Table 5.8
Comparison of RUL prediction among different degradation models with particle filtering for NASA data

RUL prediction framework	Actual RUL		Predicted RUL		Estimation error (Cycle)		Absolute estimation error (%)	
	Cell #N1	Cell #N2	Cell #N1	Cell #N2	Cell #N1	Cell #N2	Cell #N1	Cell #N2
Model 2 [19] with particle filtering	25	36	42	31	17	-5	68%	14%
Model 3 [35] with particle filtering	25	36	10	14	-15	-22	60%	61%
Model 4 [159] with particle filtering	25	36	35	40	10	4	40%	11%
Proposed framework	25	36	18	29	-7	-7	28%	19%

The RUL prediction performance for the proposed framework is compared with other degradation models with particle filtering, and the results are shown in Table 5.8. The one-term exponential model (model 1) [20] is not included in the comparison due to poor performance in capturing the nonlinear capacity degradation patterns for all battery cells. As for the two-term exponential model (model 2) [19] with particle filtering, the predicted RULs of cells #N1 and

#N2 are 42 and 31 cycles, respectively, which indicates the estimation errors of cycles are 17 and -5. Thus, the absolute estimation error percentages for cells #N1 and #N2 are 68% and 14%, respectively, and the average absolute estimation error percentage is 41%. As for the ensemble model (model 3) [35] with particle filtering, the predicted RULs of cells #N1 and #N2 are 10 and 14 cycles, which indicates the estimation errors of cycles are -15 and -22, respectively. The absolute estimation error percentages for cells #N1 and #N2 are 60% and 61%, which provide an average absolute estimation error percentage of 61%. As for the sigmoidal model (model 4) [159] with particle filtering, the predicted RULs of cells #N1 and #N2 are 35 and 40 cycles, which indicates the estimation errors of cycles are 10 and 4, respectively. The absolute estimation error percentages for cells #N1 and #N2 are 40% and 11%, which provide an average absolute estimation error percentage of 26%. In conclusion, the proposed framework provides the best predicted RULs among all models for NASA data.

5.5. Conclusion

Battery capacity degradation is a complex process with nonlinear behaviors. Single-phase degradation models cannot accurately describe various degradation patterns. The existing two-phase degradation models have drawbacks, for example, the models are computationally complex or the models are not realistic due to simplicity. The battery cells tested in the lab show the two-phase degradation pattern with different change points. Motivated by the Li-ion battery degradation data in the lab, binary segmentation is first applied to identify the change point for battery cells and then propose a two-phase capacity degradation model with a dynamic change point. Besides, variations of degradation behaviors among different battery cells are observed. Thus, a particle filtering-based framework considering uncertainties is proposed to integrate the proposed two-phase degradation model for RUL prediction. The proposed framework shows

superior performance in RUL predictions compared to other models using both laboratory data and NASA battery data. For future studies, I plan to conduct experiments for Li-ion battery cells under various operating conditions and further develop new methods for battery prognostics and health management.

CHAPTER 6

6. A Wiener Process Degradation Model with Identified Change Point for Lifetime Assessment and Maintenance on Lithium-ion Batteries

6.1.Introduction

As an energy storage system, Lithium-ion (Li-ion) batteries are commonly used in real-life applications, for example, electric vehicles [160-161]. Li-ion batteries have advantages such as low weight, long lifespan, and low self-discharge rate [9, 160-161]. However, their capacities continue to degrade and eventually fail to meet the operational demand of battery systems. The failure of batteries can cause catastrophic consequences, such as the recall of notebook computers in 2018 by Hewlett-Packard company [162]. Battery RUL prediction can monitor the battery health states to ensure the functionalities of batteries in real applications, in which RUL is the period from the current degradation state until the battery capacity degrades below a failure threshold [19-20, 149, 163]. In addition, appropriate battery replacement policies based on lifetime prediction models can benefit system management (e.g., maintenance cost and system reliability) in the long run. [136, 147, 164-165]. Therefore, RUL prediction and the replacement policy are critical to manage battery health [136, 147, 164-165].

The existing battery degradation models for RUL prediction have two frameworks, the one stage [5-6] and the two-stage degradation models [9, 36, 112, 117]. The two-stage degradation models generally perform better than single stage degradation models. However, change point (CP) is not well addressed in current two-stage degradation models. One way is to consider CP is fixed to simplify the degradation model [36]. Another way is to treat CP as a random variable; however, this results in complex modeling and high computational costs [112]. This is because a transition probability function is needed to approximate the degradation status

at CP in the RUL prediction, which is an extra term compared with the RUL prediction with a deterministic CP [38]. Besides, CP and other model parameters are obtained using the maximum likelihood estimation (MLE), which increases the total number of estimated parameters and causes extra computational costs [38, 112]. In these cases, research efforts are required to reduce model complexity or computational costs. Lastly, the majority of existing studies [9, 166] detected CP by using battery capacity data with specific algorithms. However, the capacity data may not be easily obtained when the battery is not fully charged or discharged, and this situation commonly exists in real applications [79, 167-168]. In addition, the capacity data has a non-monotonic degradation pattern, which makes it hard to use in determining CP.

A CP can separate the capacity degradation process into two different drop patterns, where the voltage data can be applied for CP detection. Specifically, the voltage curves at different cycles usually vary, representing different degradation stages, which are related to the degradation levels of the battery and its lifetime [59, 167-170]. For example, the time for equal voltage interval [168] decreases as the battery degrades. Meanwhile, in the laboratory battery data, the discharge voltage curves vary along with the degradation process and show two distinct drop patterns at the early and late degradation stages. The discharge voltage curves take much less time to reach cut-off voltage at the late degradation stage than at the early stage. Since the discharge voltage curves and the capacity degradation process are correlated [167-169], CP can be detected by differentiating two drop patterns from the discharge voltage data.

The contributions of this study are summarized as follows:

(1) A hybrid method that combines dynamic time warping (DTW) [171-172] and nonnegative matrix factorization (NMF) [173-174] is proposed to detect the CP of capacity degradation by using discharge voltage data.

(2) A two-stage Wiener process incorporating CP detection (TSWP-CP) model that combines the two-stage Wiener process (TSWP) and CP detection method is proposed to capture the battery degradation process.

(3) The RUL analytic expressions of TSWP-CP are derived in terms of the identified CP which reduces the model complexity, compared with the two-stage degradation models that consider a CP as a random variable [38].

(4) Two replacement policies with simulated parameters are applied to minimize the maintenance cost for Li-ion batteries in the long term, which can be used for a variety of batteries.

The paper structure is listed below. Section 6.2 first introduces concepts for DTW and NMF for identifying the CP, and then proposes the TSWP-CP model. Finally, the maintenance models with different replacement policies are provided. Section 6.3 displays the battery RUL prediction results using laboratory data and NASA data [129]. The optimal long-term cost rate of the maintenance model is calculated, and the replacement actions are determined. Section 6.4 gives conclusions and the future study.

6.2. Li-ion Battery Lifetime Prediction and Maintenance Using Proposed TSWP-CP

A complete procedure for battery lifetime prediction and maintenance is proposed, shown in Fig. 6.1. The battery degradation data including both capacity profile and voltage profile is collected by the battery testing platform, which consists of a control computer and battery testers. Then, DTW is utilized to obtain the similarity matrix for each battery cell using discharge voltage curves. Then, the CP of the battery cell is identified by NMF, which separates the similarity matrix into two factorized matrices. A TSWP-CP model is proposed, and model parameters are estimated by MLE. The RUL analytic expressions under different cases based on the proposed

TSWP-CP are obtained. Finally, the inspection replacement policy and the age replacement policy are applied to minimize the average long-term maintenance cost rate for Li-ion batteries. The following subsections provide details of each step proposed in Fig. 6.1.

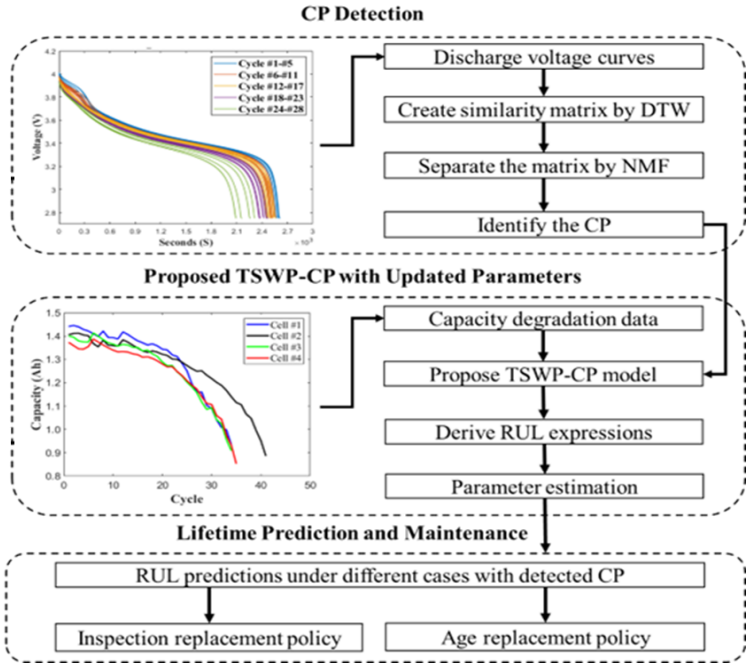

Figure 6.1. Diagram of battery lifetime prediction and maintenance based on the proposed TSWP-CP model.

6.2.1. CP Detection Based on Discharge Voltage Data

In this section, CP is detected by using discharge voltage data, which is a group of curves based on the number of discharge cycles. The discharge voltage drop patterns are correlated to battery capacity degradation stages. Because a two-stage capacity degradation model is considered, only one CP needs to be detected. Therefore, two different drop patterns need to be identified. A hybrid method including DTW and NMF is applied to obtain distance-based information from voltage curves to form a similarity matrix and then separate the original matrix into two factorized matrices to detect CP.

6.2.1.1. Voltage Curves Similarity by DTW

The similarity matrix, in which each element of the matrix represents the relevance between two discharge voltage curves, is established by using DTW. It finds the optimal path that has the minimum distance between two time series by matching data points nonlinearly [172]. Give two time series of $Q = \{Q_1, Q_2, \dots, Q_{e1}, \}$ and $P = \{P_1, P_2, \dots, P_{e2}, \}$ with lengths $e1$ and $e2$, DTW can obtain the minimum Minkowski distance under l_p norm based on the paired points from two time series. An $e1$-by- $e2$ distance matrix can include all possible alignments between points Q_n and P_m. As for each alignment (n, m) in the matrix, it represents the distance between two points and is defined by $d(n, m) = \|Q_n - P_m\|_p$, in which $\|\cdot\|_p$ represents the l_p norm. For instance, if $p = 2$, the distance is measured by Euclidean distance. After the distance matrix is obtained, the expressions for the shortest distance between two time series can be written in Eq. (6.1), in which S represents path length.

$$DTW_p(Q, P) = min\left\{\sqrt[p]{\sum_{l=1}^{S} d_l(n, m)}\right\} \tag{6.1}$$

There are several constraints given in the point-matching process of the distance matrix before. First, the first and the last matches must be (Q_1, P_1) and (Q_{e_1}, P_{e_2}). Second, jumping is not allowed in the path. The next step of alignment (Q_n, P_m) must go to alignments (Q_n, P_{m+1}), (Q_{n+1}, P_m), or (Q_{n+1}, P_{m+1}). Third, the indices of n and m can stay the same or monotonically increase in the warping path. For example, given $d_l(n, m)$, I have $d_{l-1}(n', m')$, $n \geq n'$ and $m \geq m'$.

Let M denote the total discharge cycle numbers of the battery cell and $D_{i,j} = DTW_p(i, j)$, which denotes the shortest distance between the i^{th} and the j^{th} discharge voltage curves. A M-by-M similarity matrix can be written in Eq. (6.2). The diagonal of the similarity matrix is zero because it measures the shortest distance between two same discharge voltage curves.

$$D = \begin{bmatrix} 0 & D_{1,2} & \dots & D_{1,M} \\ D_{2,1} & 0 & \dots & D_{2,M} \\ \vdots & \vdots & \ddots & \vdots \\ D_{M,1} & D_{M,2} & \dots & 0 \end{bmatrix} \tag{6.2}$$

6.2.1.2. CP Detection via NMF

The similarity matrix includes the distance-based information among all discharge voltage curves, which requires a specific method to extract matrix representatives with classification properties for differentiating battery degradation stages. NMF is a dimensionality reduction method with advanced abilities in representing the original matrix [175]. The main concept is to use a product of two factorized matrices to replace the original matrix. Give a nonnegative matrix $Y \in R^{m \times n}$ and a positive integer δ, where $\delta < \min\{m, n\}$, a function of two nonnegative factorized matrices $V \in R^{m \times \delta}$ and $U \in R^{\delta \times n}$ can be minimized based on Eq. (6.3).

$$f(V, U) = \frac{1}{2}\|Y - VU\|_F^2 \tag{6.3}$$

where $\|\cdot\|_F$ represents the Frobenius norm of a matrix. The product of VU is the NMF of matrix Y. V is the base matrix in which each column represents a specific classification group. U is the coefficient matrix, in which values of every column represent the weights to approximate the corresponding column of Y in terms of V. The selection of δ is critical for factorization. In practice, the value is dependent on the problem of obtaining a compressed form of the original dataset [174].

The coefficient matrix U can be used for CP detection for battery capacity degradation process by using its classification property [176]. First, matrix $Y \in R^{M \times M}$ is the similarity matrix obtained in Eq. (6.2). In this study, I consider a two-stage degradation process, therefore, only one change point needs to be detected. Thus, δ is 2. Then, based on Eq. (6.3), the factorized matrices $V \in R^{M \times 2}$ and $U \in R^{2 \times M}$ can be obtained by minimizing the mean square residual

between the matrix Y and the product of factorized matrices. Then, for any column i of matrix U, two elements are assigned in two rows, denoted as $U_{1,i}$, and $U_{2,i}$. They can be used to separate degradation data into two groups based on cycles. Starting from the first column, if the value of the first row is greater than that of the second row, e.g., $U_{1,i} \geq U_{2,i}$, the i^{th} cycle is assigned to the first group. Otherwise, it is assigned to the second group. The CP is detected when the $(i+1)^{th}$ cycle is in a different group compared with i^{th} cycle, and CP is the i^{th} cycle.

6.2.2. Battery RUL Analytic Expressions of TSWP-CP with Estimated Parameters

By combining a TSWP model and the proposed CP detection method, the proposed TSWP-CP can model the non-monotonic behaviors of battery degradation process and efficiently detect the CP. In addition, the analytical expression of RUL under three cases based on the proposed TSWP-CP can be obtained, which reduces the computational cost of RUL prediction compared with the degradation models that consider CP as a random variable.

6.2.2.1. Two-stage Wiener Process Model for RUL Prediction

Let $X(t)$ represent the capacity degradation status with t. Note that t can be time or cycle. In this study, t denotes time. The battery degradation process is described by a TSWP model. According to studies [117, 177], the nonlinear drift coefficients are used in the proposed model. The TSWP-CP model is as follows:

$$X(t) = \begin{cases} X(0) + \alpha_1 \int_0^t u_1(t_1, \theta_1) dt_1 + \sigma_1 B(t), 0 < t < \tau \\ X(\tau) + \alpha_2 \int_\tau^t u_2(t_2 - \tau, \theta_2) dt_2 + \sigma_2 B(t - \tau), t \geq \tau \end{cases} \tag{6.4}$$

where $X(0) = 0$ is the initial degradation value, τ is the time at CP, and CP is the number of cycles that separate the dataset into two stages. $X(\tau)$ is the degradation amount at τ. $B(t)$ is the standard Brownian motion. $\alpha_1 \int_0^t u_1(t_1, \theta_1) dt_1$ and σ_1 represent the drift and diffusion coefficients in the first stage. $\alpha_2 \int_\tau^t u_2(t_2 - \tau, \theta_2) dt_2$ and σ_2 represent the drift and diffusion

coefficients in the second stage. All parameters in Eq. (6.4) are assumed to be independent. α_1 and α_2 are treated as two random variables. θ_1 and θ_2 are parameters in the drift coefficients.

The first hitting time (FHT) is applied for battery health assessment, which is the time when $X(t)$ first hits a critical threshold. The expression is given in Eq. (6.5) where ω is a predefined failure threshold.

$$T = \inf\{t: X(t) \geq \omega | X(0) < \omega\} \tag{6.5}$$

Let a data set $X_{0:m} = \{X_0, X_1, \ldots, X_m\}$ be the capacity degradation data measured at discrete time points t_0, t_1,…, and t_m. Then the RUL is denoted as L_m at time t_m can be written in Eq. (6.6) where l_m represents the period between the predicted time t_m and the failure time.

$$L_m = \inf\{l_m: X(l_m + t_m) \geq \omega | X(t_m) < \omega\} \tag{6.6}$$

By using a time-space transformation, the Kolmogorov equation of a diffusion process can be transformed into the Kolmogorov equation of standard Brownian motion [177]. The probability density function (PDF) of FHT for the original diffusion process can be obtained by using the PDF of FHT of the transformed standard Brownian motion. By using Theorem 2 developed in [177], The expressions of the PDF of a battery lifetime based on TSWP-CP are given in Eq. (6.7).

$$f_T(t|a_i) =$$

$$\begin{cases} \frac{\omega - \alpha_1\left(\int_0^t u_1(t_1,\theta_1)dt_1 - u_1(t,\theta_1)t\right)}{\sigma_1 t\sqrt{2\pi t}} \times \exp\left(-\frac{\left(\omega - \alpha_1 \int_0^t u_1(t_1,\theta_1)dt_1\right)^2}{2\sigma_1^2 t}\right), 0 < t < \tau \\ \frac{\omega - x_\tau - \alpha_2\left(\int_\tau^t u_2(t_2-\tau,\theta_2)dt_2 - u_2(t-\tau,\theta_2)(t-\tau)\right)}{\sigma_2(t-\tau)\sqrt{2\pi(t-\tau)}} \times \exp\left(-\frac{\left(\omega - x_\tau - \alpha_2 \int_\tau^t u_2(t_2-\tau,\theta_2)dt_2\right)^2}{2\sigma_2^2(t-\tau)}\right), t \geq \tau \end{cases} \tag{6.7}$$

in which $\alpha_1 \sim N(u_{a_1}, \sigma_{a_1}^2)$ and $\alpha_2 \sim N(u_{a_2}, \sigma_{a_2}^2)$ represent the random effects on the degradation process. The PDF of the lifetime of a battery cell with two stages can be further obtained by using Theorem 3 in study [177], shown in Appendix A.

The exponential functions $u_1(t,\theta_1) = \theta_1 \exp(\theta_1 t)$ and $u_2(t,\theta_2) = \theta_2 \exp(\theta_2 t)$ are used for the nonlinear functions for the drift coefficients in the proposed TSWP-CP. The RUL expressions based on FHT can be obtained by establishing a new diffusion process using Theorem 4 from Si et al. [177]. The expressions for all three cases are derived as follows, in which the PDF of RUL of a battery cell is denoted as $f(l_m)$.

In Case I, the current time t_m is less than τ, and the summation t_m and its RUL is less than τ. The RUL at time t_m is equal to the FHT of the diffusion process $Y(l_m)$, where $Y(l_m) = X(l_m + t_m) - X(t_m)$ crossing the threshold $\omega - x_{t_m}$.

Case I: If $0 < t_m < \tau$ and $l_m < \tau - t_m$, then

$$f(l_m) = \frac{1}{\sqrt{2\pi l_m^2\left(\sigma_{a_1}^2 {\gamma_1}^2(l_m) + \sigma_1^2 l_m\right)}} \times \left(\omega - x_{t_m} - \beta_1(l_m) \times \frac{(\omega - x_{t_m})\sigma_{a_1}^2 \gamma_1(l_m) + u_{a_1}\sigma_1^2 l_m}{\sigma_{a_1}^2 {\gamma_1}^2(l_m) + \sigma_1^2 l_m}\right) \times \exp\left(-\frac{\left(\omega - x_{t_m} - u_{a_1}\gamma_1(l_m)\right)^2}{2\left(\sigma_{a_1}^2 {\gamma_1}^2(l_m) + \sigma_1^2 l_m\right)}\right) \quad (6.8)$$

where $\gamma_1(l_m) = \exp\big(\theta_1(l_m + t_m)\big) - \exp(\theta_1 t_m)$ and $\beta_1(l_m) = (1 - \theta_1 l_m)\exp\big(\theta_1(l_m + t_m)\big) - \exp(\theta_1 t_m)$.

In Case II, the current time t_m is less than τ, and the summation of t_m and its RUL is greater than τ. The chance of the degradation path passing the threshold before the CP is negligible [117]. In this case, a lifetime PDF, denoted as $g(v)$, of a new diffusion process $G(v) = X(v + \tau) - X(\tau)$ crossing the threshold $\omega - x_\tau$ can be first obtained. Then the PDF of RUL $f(l_m)$ at time t_m can be obtained, which has the same expression as $g(l_m + t_m - \tau)$.

Case II: If $0 < t_m < \tau$ and $l_m \geq \tau - t_m$, then

$$f(l_m) = \frac{1}{\sqrt{2\pi(l_m + t_m - \tau)^2\left(\sigma_{a_2}^2 {\gamma_2}^2(l_m) + \sigma_2^2(l_m + t_m - \tau)\right)}}$$

$$\times\left(\omega-x_{\tau}-\beta_2(l_m)\times\frac{(\omega-x_{\tau})\sigma_{a_2}^2\gamma_2(l_m)+u_{a_2}\sigma_2^2(l_m+t_m-\tau)}{\sigma_{a_2}^2{\gamma_2}^2(l_m)+\sigma_2^2(l_m+t_m-\tau)}\right)\times\exp\left(-\frac{\left(\omega-x_{\tau}-u_{a_2}\gamma_2(l_m)\right)^2}{2\left(\sigma_{a_2}^2{\gamma_2}^2(l_m)+\sigma_2^2(l_m+t_m-\tau)\right)}\right) \quad (6.9)$$

where $\gamma_2(l_m)=\exp\big(\theta_2(l_m+t_m-\tau)\big)-1$ and $\beta_2(l_m)=(1-\theta_2(l_m+t_m-\tau))\exp\big(\theta_2(l_m+t_m-\tau)\big)-1$.

Case III: If $t_m \geq \tau$, then

$$f(l_m)=\frac{1}{\sqrt{2\pi l_m^2\left(\sigma_{a_2}^2{\gamma_3}^2(l_m)+\sigma_2^2 l_m\right)}}$$

$$\times\left(\omega-x_{t_m}-\beta_3(l_m)\times\frac{(\omega-x_{t_m})\sigma_{a_2}^2\gamma_3(l_m)+u_{a_2}\sigma_2^2 l_m}{\sigma_{a_2}^2{\gamma_3}^2(l_m)+\sigma_2^2 l_m}\right)\times\exp\left(-\frac{\left(\omega-x_{t_m}-u_{a_2}\gamma_3(l_m)\right)^2}{2\left(\sigma_{a_2}^2{\gamma_3}^2(l_m)+\sigma_2^2 l_m\right)}\right) \quad (6.10)$$

where $\gamma_3(l_m)=\exp\big(\theta_2(l_m+t_m-\tau)\big)-\exp\left(\theta_2(t_m-\tau)\right)$ and $\beta_3(l_m)=(1-\theta_2 l_m)\exp\big(\theta_2(l_m+t_m-\tau)\big)-\exp\left(\theta_2(t_m-\tau)\right)$.

6.2.2.2. Model Parameter Estimation

All parameters in the RUL functions for the above three cases can be obtained based on MLE [38]. Let $\emptyset_i$ denote the parameter set $\{u_{a_i},\sigma_{a_i},\sigma_i,\theta_i\}$, $X_{n,0:m}=\{X_{n,1},X_{n,2},\dots,X_{n,m}\}$ denote the capacity degradation data of the n^{th} battery cell with a total number of measurements as m, and $t_{n,0:m}=\{t_{n,1},t_{n,2},\dots,t_{n,m}\}$ denote the specific degradation time for the n^{th} battery cell. For the n^{th} battery cell, let $k_{1,n}$ represent the total number of observations in the first stage and $k_{2,n}$ represent the total number of observations in the second stage. The log-likelihood function for the parameter set can be derived in Eq. (6.11) [38]:

$$G(\emptyset_i|\Delta X)=\begin{cases}-\frac{\ln(2\pi)\sum_{n=1}^{N}k_{1,n}}{2}-\frac{1}{2}\sum_{n=1}^{N}\ln\left|O_{1,n}\right|-\frac{1}{2}\sum_{n=1}^{N}(\Delta X_{1,n}-J_{1,n})'\,O_{1,n}^{-1}(\Delta X_{1,n}-J_{1,n})\\ -\frac{\ln(2\pi)\sum_{n=1}^{N}k_{2,n}}{2}-\frac{1}{2}\sum_{n=1}^{N}\ln\left|O_{2,n}\right|-\frac{1}{2}\sum_{n=1}^{N}(\Delta X_{2,n}-J_{2,n})'\,O_{2,n}^{-1}(\Delta X_{2,n}-J_{2,n})\end{cases} \quad (6.11)$$

where ΔX denotes a matrix for the degradation difference between two consecutive observation times, specifically, $\Delta X_{1,n} = [X_{n,1} - X_{n,0}, X_{n,2} - X_{n,1}, \dots, X_{n,k_1} - X_{n,k_{1,n}-1}]$, and $\Delta X_{2,n} = [X_{n,k_{1,n}+1} - X_{n,k_{1,n}}, X_{n,k_{1,n}+2} - X_{n,k_{1,n}+1}, \dots, X_{n,k_{2,n}+k_{1,n}} - X_{n,k_{2,n}+k_{1,n}-1}]$. The increment $\Delta X_{i,n}$ follows a multivariate normal distribution with mean $J_{i,n}$ and variance $O_{i,n}$. The expressions for $J_{i,n}$ and $O_{i,n}$ are given in Appendix B. To maximize the log-likelihood function, the MATLAB function "fminsearch" is applied, which can use simplex search algorithms for multi-dimensional search purposes [38].

6.2.3. Replacement Policies

A maintenance model is to determine the appropriate replacement strategies by balancing the maintenance requirements and resources and a high-level system reliability [136, 164]. As for the Li-ion battery system, an appropriate maintenance model can assist the management team to plan maintenance schedules to prevent system failure by replacing failed battery cells, meanwhile, minimizing the long-term system maintenance cost (e.g., material costs and labor costs). In this section, two replacement policies are studied.

Inspection replacement policy: The periodical inspection allows a constant inspection interval on the system, in which the system only gets replaced if a failure is inspected. If the system does not fail, no replacement is needed. Three types of costs are considered for this maintenance model, inspection cost, downtime cost, and replacement cost. The optimal inspection period can be calculated and determined by minimizing the average long-term maintenance cost rate $CR_I(t)$ [164].

$$CR_I(t) = \frac{C_I E[NUM_I] + C_p E[p] + C_R}{E[TK]} \tag{6.12}$$

where C_I is each inspection cost, C_R is the replacement cost, C_p is the cost associated with the system downtime, $E[p]$ is the expected downtime of the system, and $E[TK]$ is the expected time between two replacements. The expected number of inspections NUM_I, $E[NUM_1]$, is:

$$E[NUM_I] = \sum_{i=1}^{\infty} i(F_T(i\partial) - F_T((i-1)\partial) \quad (6.13)$$

where $F_T(t)$ is the cumulative distribution function (CDF) of the failure time. ∂ is the inspection interval. Based on Eq. (6.12), I can search for a value that minimizes the average long-term maintenance cost rate for a given inspection interval.

Age replacement policy: The battery system is replaced at a constant age t. If the system fails before t, the replacement is to replace the failed battery, otherwise, it is a preventive replacement. The long-term maintenance cost rate $CR_A(t)$ is calculated by the ratio of the expected cost between two replacements to the expected time between two replacements [164], shown in Eq. (6.14), and the optimal replacement age is obtained by minimizing $CR_A(t)$.

$$CR_A(t) = \frac{C_F(1-R(t))+C_R}{tR(t)+\int_0^t sf(s)ds} \quad (6.14)$$

where C_F is the cost due to failure, C_R is the cost of replacement, $R(t)$ represents the system reliability function, and $f(t)$ is the PDF of system lifetime.

6.3.Results

6.3.1. Design of Experiments

The cylindrical Li-ion battery cells from EBL company are applied for battery capacity tests. The details of battery specifications and experiment settings can be referred to study [9]. The initial capacity indicated by the manufacturer is 1.6 Ah. The battery cells are charged at a constant current 1.25 C rate (2A) and then discharged at 1.25 C rate (2A) under 25°C ambient temperature. The reason for using constant current charge and discharge mode is that some battery applications in real-world require constant current for their operations, such as wireless sensors

for indoor harmful gas monitoring [178] and wearable electronics for health monitoring [179]. Besides, electronic devices such as mobile phones, laptops, and digital cameras need constant current during certain operations [180]. From this point of view, the proposed model is applicable in real-world uses. Other experiment settings are given as Chapter 3 mentions.

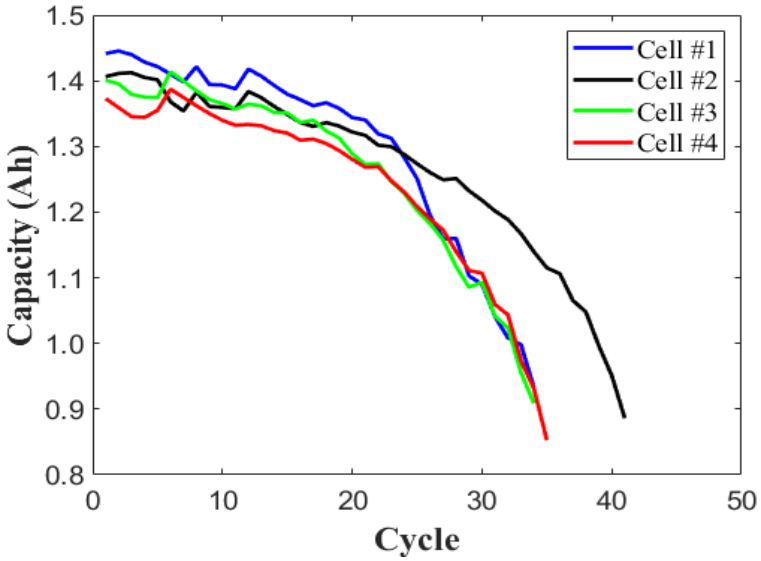

Figure 6.2. Four battery cell capacity degradation patterns from the lab experiments.

Under the experiment setting, the capacity drops with the number of cycles, as shown in Fig. 6.2. A capacity regeneration phenomenon [181] is observed at the early degradation stage, especially for cells #3 and #4. All battery cells first experience a slow degradation rate and then enter a fast degradation stage. Due to the battery cells' quality, the short rest period, and the relatively high charge and discharge C rate, all cells' capacities degrade below 70% after 40 cycles, which is much faster than the experimental data collected from other studies.

6.3.2. RUL Prediction

6.3.2.1. Laboratory Data

The battery lifetime is the total cycle number as the battery capacity decreases from 100% to 70%. The proposed model uses the 100% - 80% degradation data to estimate parameters and the 80% - 70% degradation data is used for RUL prediction. The voltage curves of 100% - 80%

degradation data for four battery cells are displayed in Fig. 6.3. Similar drop patterns can be observed from different voltage curves if they are at the same degradation stage. For example, any two voltage curves from the first degradation stage spend approximately equivalent time to reach the voltage threshold. The discharge voltage curves from the second stage take less and less time to reach the voltage threshold as cycle numbers increase.

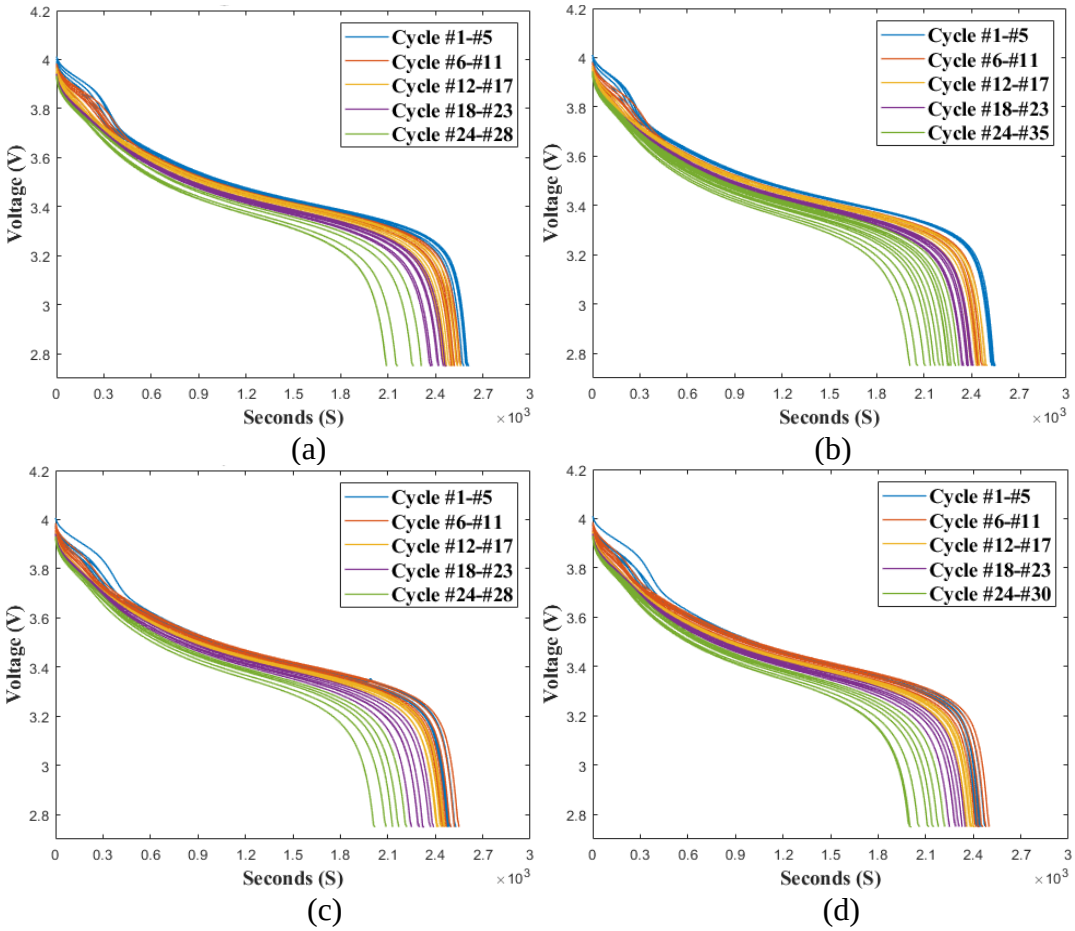

Figure 6.3. Voltage discharge profiles from the lab experiments for cells: (a) #1; (b) #2; (c) #3; (d) #4.

DTW is first used to measure the similarity among different discharge voltage curves and generate the similarity matrix for each battery cell. Then, NMF is applied to detect CP for each battery cell. Eq. (6.3) has two rows with M columns, in which M represents the total number of cycles. Starting from the first column, if the value in the first row is greater than that in the second row, the corresponding cycle is assigned to the first group. Otherwise, it is assigned to the

second group. CP is obtained when a cycle is first assigned in a different group compared with the previous cycle. CPs for laboratory battery cells #1-4 are the last cycle in the first stage, which are 22, 23, 20, and 22, respectively.

Fig. 6.4 displays the values of all rows for each column in U for cells #2 and #4. $U_{1,i}$ and $U_{2,i}$ are used to represent elements in the first and second row of the i^{th} column. They are used to indicate a data point ($U_{1,i}$, $U_{2,i}$) in a two-dimensional coordinate. A line can be drawn to link this data point with the origin coordinate. Multiple lines can be obtained based on different data points from different columns of U. A diagonal line is given as a reference line to separate all lines into two stages. Any line with a larger slope than the reference line belongs to the first stage, which has a blue color in Fig. 6.4. The corresponding cycle is assigned to the first stage. Otherwise, the line has a red color in Fig. 6.4, and the corresponding cycle is assigned to the second stage.

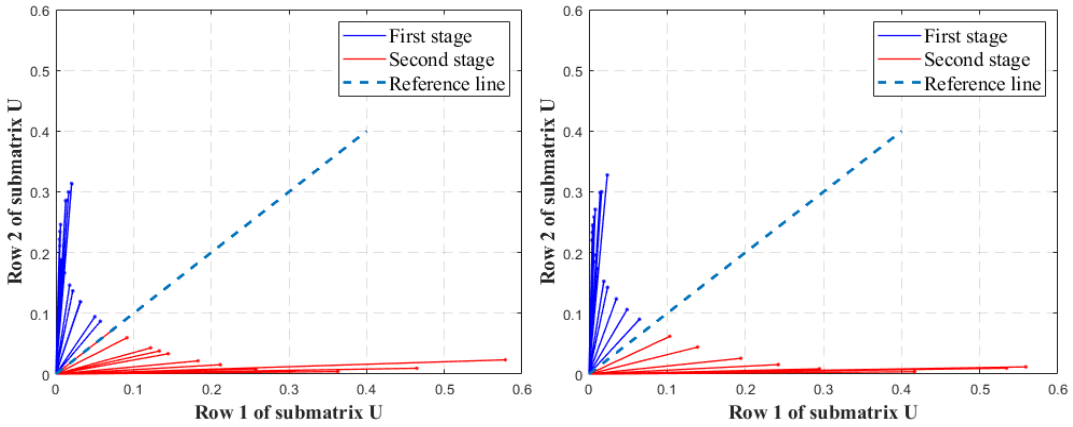

(a) (b)

Figure 6.4. Visualization of U based on different columns for cells: (a) #2; (b) #4.

The proposed TSWP-CP model, shown in Eq. (6.4), has two stages with the identified CPs from NMF. To obtain the specific expressions for two stages, parameters $\{u_{a_i}, \sigma_{a_i}, \sigma_i, \theta_i\}$ need to be estimated by MLE using Eq. (6.11). The first 20% degradation data is separated into two stages for estimating the corresponding parameters. By applying the "fminsearch" algorithm

from MATLAB, the optimal values for all parameters for both stages can be obtained: as for the first stage, $u_{a_1} = 0.6, \sigma_{a_1} = 0.08, \sigma_1 = 8e-9, \theta_1 = 3e-6$; as for the second stage, $u_{a_2} = 0.13, \sigma_{a_2} = 0.13, \sigma_2 = 8e-6, \theta_2 = 2.3e-5$.

Based on the estimated parameters, the specific expressions for Eqs. (6.8), (6.9), and (6.10) are obtained. Various values of the predicted time t_m are assigned for predicting RUL to assess the reliability of the proposed model. The corresponding sample cycles at t_m to predict RUL are $5, 10, 15, 20, 25,$ and lc, in which lc denotes the number of cycles when the battery capacity drops to 80%. The value of lc varies for different battery cells. The PDFs of RULs and the predicted RULs for cells #1-4 are displayed in Figs. 6.5(a)-(d).

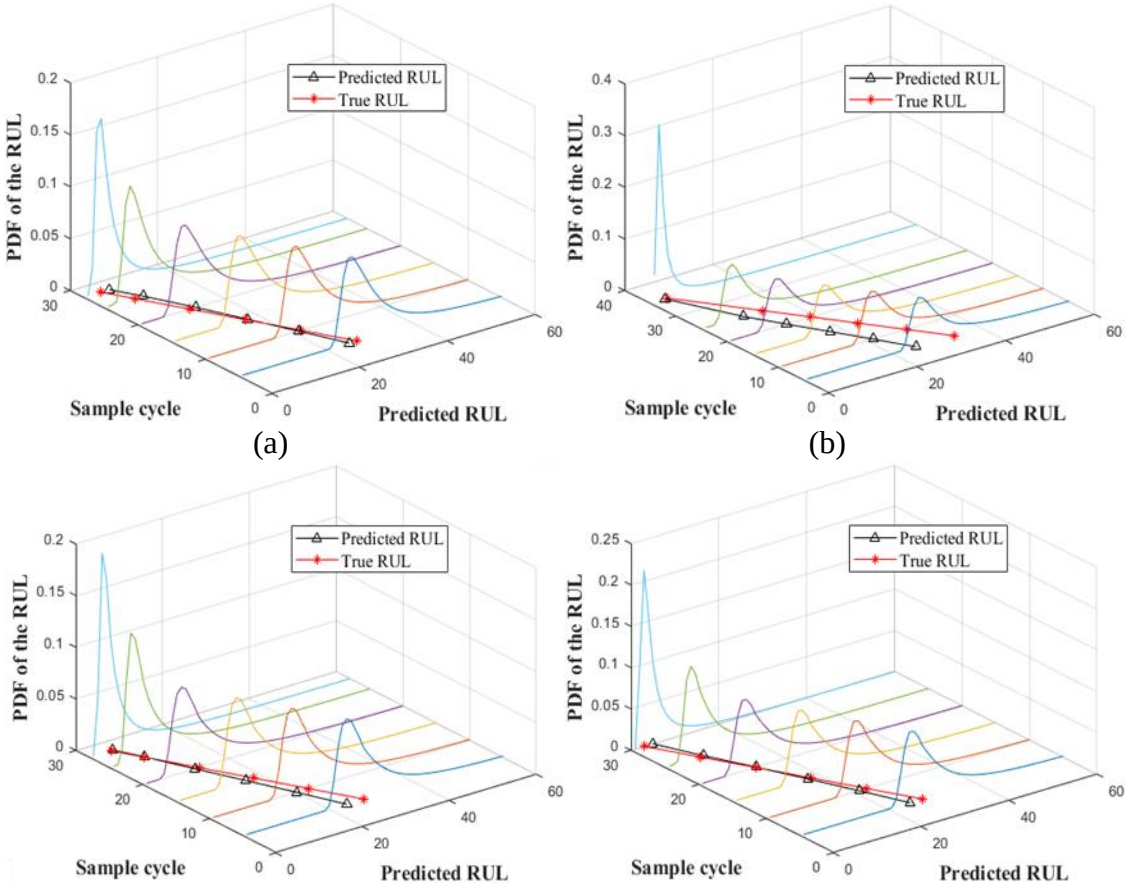

Figure 6.5. PDFs of RUL for cells: (a) #1; (b) #2; (c) #3; (d) #4.

In the horizontal panel of these figures, the red line represents the true RUL of each cell. The black line shows the predicted RUL based on the PDF of each cell's RUL. In each graph, as the sampled cycle increases, the peak of the PDF of the RUL increases, and the mean of the predicted RUL keeps shifting. To evaluate the prediction performance of the proposed model, the estimation errors in cycles (EEC) and the absolute estimation errors in percentages (AEEP) are applied to calculate the prediction accuracy. Another two prediction models, one stage Wiener process model [177], and the TSWP model with fixed CP are utilized to compare the performance to the proposed model. All three prediction models use the first 20% degradation data for parameter estimation and the next 10% degradation data for prediction.

Table 6.1
Models' performance of RUL prediction for cells #1-2

Models	Sampled cycle	Actual RUL		Predicted RUL		EEC		AEEP	
		#1	#2	#1	#2	#1	#2	#1	#2
One stage Wiener process model [177]	5	27	34	19	19	-8	-15	30%	44%
	10	22	29	17	16	-5	-13	23%	45%
	15	17	24	16	15	-1	-9	6%	38%
	20	12	19	14	13	2	-6	17%	32%
	25	7	14	10	11	3	-3	43%	21%
	l_c	4	4	7	5	3	1	75%	25%
TSWP model with fixed CP ($CP = 15$)	5	27	34	26	25	-1	-9	4%	26%
	10	22	29	19	19	-3	-10	14%	34%
	15	17	24	12	12	-5	-12	29%	50%
	20	12	19	10	10	-2	-9	17%	47%
	25	7	14	7	7	0	-7	0%	50%
	l_c	4	4	6	3	2	-1	50%	25%
Proposed TSWP-CP model	5	27	34	25	25	-2	-9	7%	26%
	10	22	29	21	21	-1	-8	5%	28%
	15	17	24	17	17	0	-7	0%	29%
	20	12	19	13	13	1	-6	8%	32%
	25	7	14	8	9	1	-5	14%	36%
	l_c	4	4	5	3	1	-1	25%	25%

Tables 6.1 and 6.2 show the comparison of model performance for cells #1-4 using different models. The predicted RULs can be decimal numbers and they are rounded to the nearest integers less than the predicted values. As for the one stage Wiener process model [177], the average AEEPs for cells #1-4 are 32%, 34%, 23%, and 33%. The overall AEEP for this

model is 31%. As for the TSWP model with fixed CP ($CP = 15$), the average AEEPs for cells #1-4 are 19%, 39%, 15%, and 24%. The overall AEEP for this model is 24%. As for the proposed model, the average AEEPs are 10%, 29%, 8%, and 10% for four cells. The overall AEEP is 14%. The comparison results show the proposed model has the best RUL prediction performance at different sampled cycles for the laboratory data.

Table 6.2
Models' performance of RUL prediction for cells #3-4

Models	Sampled cycle	Actual RUL		Predicted RUL		EEC		AEEP	
		#3	#4	#3	#4	#3	#4	#3	#4
One stage Wiener process model [177]	5	28	28	20	19	-8	-9	29%	32%
	10	23	23	19	17	-4	-6	17%	26%
	15	18	18	18	15	0	-3	0%	17%
	20	13	13	15	13	2	0	15%	0%
	25	8	8	11	10	3	2	38%	25%
	l_c	5	3	7	6	2	3	40%	100%
TSWP model with fixed CP ($CP = 15$)	5	28	28	26	26	-2	-2	7%	7%
	10	23	23	20	19	-3	-4	13%	17%
	15	18	18	13	13	-5	-5	28%	28%
	20	13	13	10	10	-3	-3	23%	23%
	25	8	8	8	8	0	0	0	0%
	l_c	5	3	6	5	1	2	20%	67%
Proposed TSWP-CP model	5	28	28	24	25	-4	-3	14%	11%
	10	23	23	20	21	-3	-2	13%	9%
	15	18	18	16	17	-2	-1	11%	6%
	20	13	13	12	13	-1	0	8%	0%
	25	8	8	8	8	0	0	0%	0%
	l_c	5	3	5	4	0	1	0%	33%

6.3.2.2. NASA Data

The proposed model is also applied to NASA dataset [129]. I select battery cells labeled "B0005" and "B0007" from the dataset, and the capacities of these cells are 2 Ah. The battery cells are first charged at constant current at 1.5 A (0.75 C) until the voltage reaches 4.2 V and charged under constant voltage until the current drops to 20 mA, then discharged under constant current at 2 A (1 C) until the voltage decreases to 2.7 V and 2.2 V, respectively. The discharged capacities of battery cells are shown in Fig. 6.6, which includes battery degradation data from

100% to 75%. Cell "B0005" takes 125 cycles to 75% degradation and 100 cycles to 80% degradation. Cell "B0007" takes 159 cycles to 75% and 123 cycles to 80%. The first 20% degradation data is used for CP detection and model parameter estimation and the next 5% degradation data is used for RUL prediction.

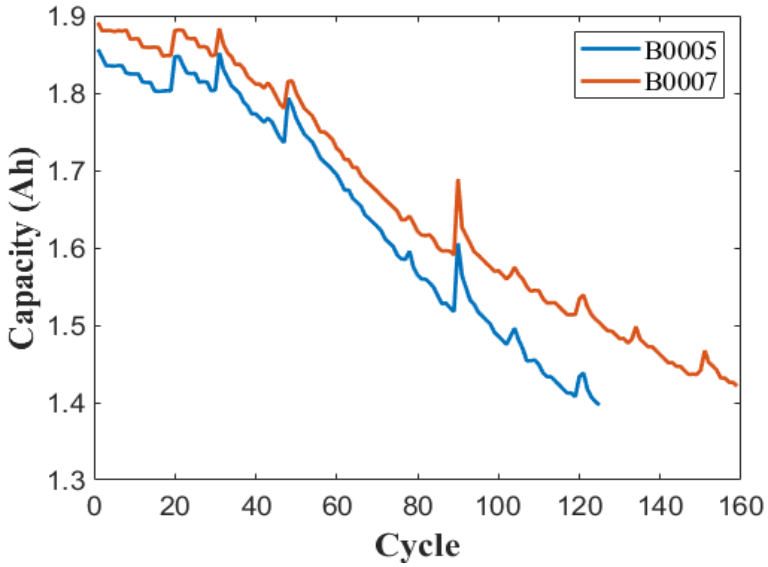

Figure 6.6. Two battery cell capacity degradation patterns from NASA dataset [129].

From Fig. 6.6 above, the battery cells show a slow drop rate at first and a fast rate later. Because the discharge voltage curves of both cells from the first 20% degradation data have too many cycles, it is difficult to distinguish these curves. Thus, a group of cycles is selected from these battery cells and shown in Fig. 6.7. As the number of cycles increases, the voltage curve decreases faster to the voltage threshold. CPs of two cells are identified as 30 and 30 by using NMF. The optimal values for all parameters for the two stages are calculated in the proposed model by applying the "fminsearch" algorithm from MATLAB. The parameters in the first stage are: $u_{a_1} = 1.5, \sigma_{a_1} = 0.01, \sigma_1 = 4e-4, \theta_1 = 5e-8$. The parameters in the second stage are: $u_{a_2} = 0.7, \sigma_{a_2} = 0.08, \sigma_2 = 9e-6, \theta_2 = 1.35e-6$. Based on the estimated parameters, the specific expressions for RUL are obtained according to Eqs. (6.8), (6.9), and (6.10). Various values of the predicted time t_m are assigned to access model performance. The corresponding

sample cycles at t_m to predict RUL are $20, 40, 60, 80,$ and lc, in which lc denotes the number of cycles as the battery capacity reaches 80%.

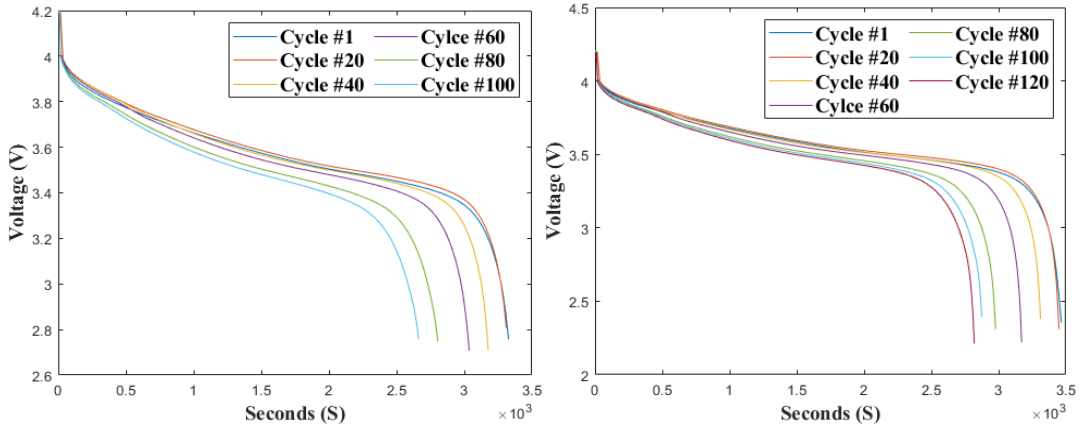

(a) (b)

Figure 6.7. Voltage discharge profiles for NASA battery cells: (a) B0005; (b) B0007.

The PDFs of RULs and the predicted RULs for both cells are displayed in Figs. 6.8(a)-(b). The EEC and AEEP are model performance metrics, and the prediction results are shown in Table 6.3. The average AEEPs for two cells are 23% and 20%. The overall AEEP is 22%. The proposed model is further compared to four existing RUL prediction models using NASA battery dataset, which are PF [105, 182], unscented particle filtering (UPF) [105, 182], support vector machine (SVM) [183], and back-propagation neural network (BPNN) [183]. Using cell B0005 as an example, I first compare the proposed model to PF and UPF based on results in study [182]. Three training datasets are used for cell B0005 in study [182], which are 60, 80, and 100 cycles. The actual RULs for these three datasets are 68, 48, and 28 cycles, respectively. The proposed model provides the EEC of 9, 8, and 1 for the three datasets. Moreover, the RUL prediction error from the proposed model is the smallest compared to PF and UPF in study [182] for all three datasets. Similarly, the proposed model provides the EEC of 2 using the same training dataset of cell B0005 in study [105], and the RUL prediction results are more accurate than PF and UFP.

Finally, the proposed model is compared with SVM and BPNN in study [183], showing a superior performance by providing the smallest EEC of 1.

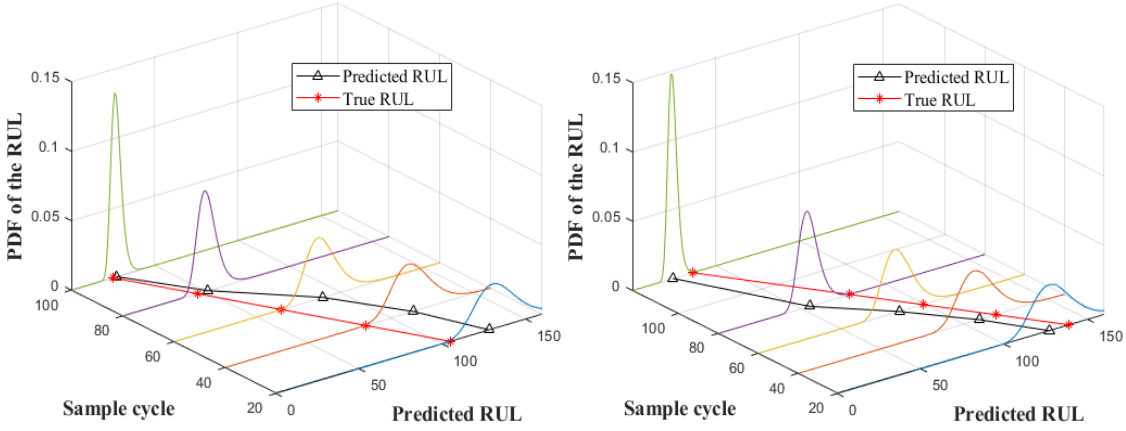

Figure 6.8. PDFs of RUL for NASA battery cells: (a) B0005; (b) B0007.

Table 6.3
Model performance of RUL prediction for cells B0005 and B0007

Models	Sampled cycle	Actual RUL		Predicted RUL		EEC		AEEP	
		B0005	B0007	B0005	B0007	B0005	B0007	B0005	B0007
Proposed TSWP-CP model	20	105	139	128	127	23	-12	22%	9%
	40	85	119	113	108	28	-11	33%	9%
	60	65	99	89	84	24	-15	37%	15%
	80	45	79	51	54	6	-25	13%	32%
	l_c	25	36	27	24	2	-12	8%	33%

6.3.3. Maintenance Cost Determination for Laboratory Cells

The maintenance model with the inspection replacement policy has three different costs, the inspection cost C_I, the cost associated with downtime C_p, and replacement cost C_R, which are given as \$30, \$2, and \$50, respectively. The maintenance model with the age replacement policy has two different costs, the failure cost C_F, and the replacement cost C_R, which are given as \$100, and \$50. Batteries are considered a failure when their capacities decrease below 70% of the initial capacities. The average long-term maintenance cost rates in terms of the number of the cycle for cells #1-4 are calculated under these two policies, shown in Figs. 6.9(a) and (b).

The optimal inspection intervals for cells #1-4 are 26, 27, 25, and 26 cycles under the inspection replacement policy. The minimal cost rates for cells #1-4 are $3.74/cycle, $3.47/cycle, $4.17/cycle, and $3.74/cycle, accordingly. The optimal age intervals for cells #1-4 are 27, 28, 25, and 27 cycles under the age replacement policy. The minimal cost rates for cells #1-4 are $1.89/cycle, $1.83/cycle, $2.02/cycle, and $1.89/cycle, respectively. Different minimal cost rates are obtained under different replacement policies, which are caused by different values of parameters assigned. The optimal cost rates for different cells are close to each other in this case study. Overall, both policies can minimize the long-term maintenance cost, and the management team may select the policy according to their maintenance resources.

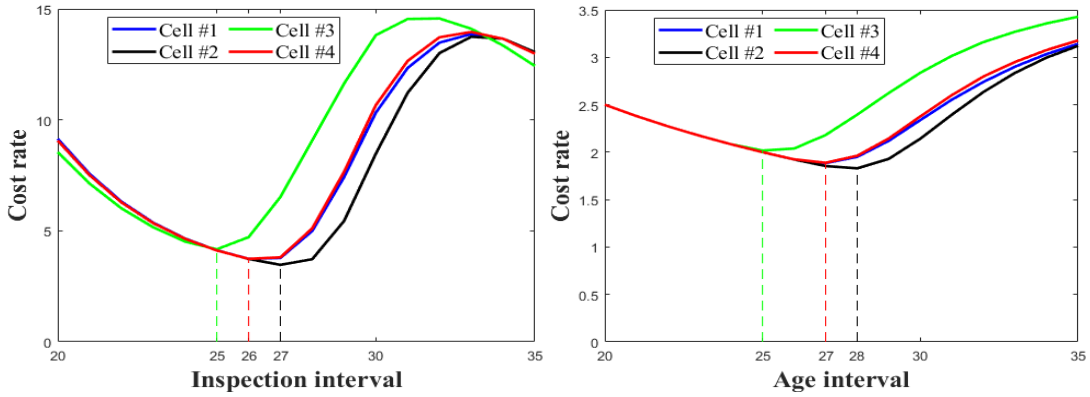

(a) (b)

Figure 6.9. The average long-term maintenance cost rate: (a) inspection replacement policy; (b) age replacement

6.4. Conclusion

The CP detection is critical to ensure an accurate RUL prediction using two-stage battery degradation models. In this study, a new method that combines DTW and NMF is developed to detect the CP of the battery degradation processes using voltage discharge profiles. Then, a TSWP-CP model that combines a TSWP and the proposed CP detection method is proposed to describe the capacity degradation behaviors. In addition, the RUL analytic expressions of TSWP-CP are derived. Lastly, RUL predictions and long-term maintenance costs are provided for both

laboratory data and NASA. The limitation of this study is that the influence of temperature on battery degradation is not considered in the model. I plan to study temperature effects on battery capacity model in future work.

CHAPTER 7

7. Conclusion and Future Study

This dissertation aims to propose battery SOH and RUL prediction models that address the existing problems in battery PHM. I am first motivated by the issues of investigating the influences of current rates on the battery degradation process, in which mathematical models for predicting SOH and RUL in terms of current rates are missing. Thus, Peukert's law-based model and DV analysis-based model are proposed in Chapter 4, the performance of these two models is evaluated based on the lab data by showing accurate prediction results. Later, I notice that the existing battery degradation models have a CP detection issue. Then, A particle filtering-based RUL prediction model incorporating CP detection model is proposed in Chapter 5. The proposed model is validated by both the lab data and NASA data, which returns superior performance compared to other existing two-phase degradation models. At last, to take advantage of the voltage data and address the nonmonotonic degradation patterns, A two-phase Wiener process model with CP detection based on voltage data is proposed in Chapter 6. The model performance is evaluated by both lab data and NASA data, which outperforms other battery RUL prediction models. As for future studies, I will focus on machine learning methods to propose new models for battery SOH and RUL prediction.

REFERENCES

[1] Yao, J., & Han, T. (2023). Data-driven lithium-ion batteries capacity estimation based on deep transfer learning using partial segment of charging/discharging data. *Energy*, *271*, 127033.

[2] Zhang, Y., & Li, Y. F. (2022). Prognostics and health management of Lithium-ion battery using deep learning methods: A review. Renewable and Sustainable Energy Reviews, *161*, 112282.

[3] Deng, Z., Lin, X., Cai, J., & Hu, X. (2022). Battery health estimation with degradation pattern recognition and transfer learning. Journal of Power Sources, *525*, 231027.

[4] Mohammadi, F., & Saif, M. (2023). A comprehensive overview of electric vehicle batteries market. E-Prime-Advances in Electrical Engineering. *Electronics and Energy*, *3*, 100127.

[5] Mahmud, M. P., Huda, N., Farjana, S. H., & Lang, C. (2019). Comparative life cycle environmental impact analysis of lithium-ion (LiIo) and nickel-metal hydride (NiMH) batteries. *Batteries*, *5(1)*, 22.

[6] Miao, Q., Xie, L., Cui, H., Liang, W., & Pecht, M. (2013). Remaining useful life prediction of lithium-ion battery with unscented particle filter technique. *Microelectronics Reliability*, *53(6)*, 805-810.

[7] Ren, L., Zhao, L., Hong, S., Zhao, S., Wang, H., & Zhang, L. (2018). Remaining useful life prediction for lithium-ion battery: A deep learning approach. *IEEE Access*, *6*, 50587-50598.

[8] Edge, J. S., O'Kane, S., Prosser, R., Kirkaldy, N. D., Patel, A. N., Hales, A., ... & Offer, G. J. (2021). Lithium ion battery degradation: what you need to know. *Physical Chemistry Chemical Physics*, *23(14)*, 8200-8221.

[9] Wang, R., Zhu, M., Zhang, X., & Pham, H. (2023). Lithium-ion battery remaining useful life prediction using a two-phase degradation model with a dynamic change point. *Journal of Energy Storage*, *59*, 106457.

[10] Birkl, C. R., Roberts, M. R., McTurk, E., Bruce, P. G., & Howey, D. A. (2017). Degradation diagnostics for lithium ion cells. *Journal of Power Sources*, *341*, 373-386.

[11] Han, X., Lu, L., Zheng, Y., Feng, X., Li, Z., Li, J., & Ouyang, M. (2019). A review on the key issues of the lithium ion battery degradation among the whole life cycle. *ETransportation*, *1*, 100005.

[12] O'Kane, S. E., Ai, W., Madabattula, G., Alonso-Alvarez, D., Timms, R., Sulzer, V., ... & Marinescu, M. (2022). Lithium-ion battery degradation: how to model it. *Physical Chemistry Chemical Physics*, *24(13)*, 7909-7922.

[13] Lin, C., Tang, A., Mu, H., Wang, W., & Wang, C. (2015). Aging mechanisms of electrode materials in lithium-ion batteries for electric vehicles. *Journal of Chemistry*, 2015.

[14] Attia, P. M., Das, S., Harris, S. J., Bazant, M. Z., & Chueh, W. C. (2019). Electrochemical kinetics of SEI growth on carbon black: part I. Experiments. *Journal of The Electrochemical Society*, *166(4)*, E97-E106.

[15] Campbell, I. D., Marzook, M., Marinescu, M., & Offer, G. J. (2019). How observable is lithium plating? Differential voltage analysis to identify and quantify lithium plating following fast charging of cold lithium-ion batteries. *Journal of the electrochemical society*, *166(4*), A725-A739.

[16] Yang, X. G., Leng, Y., Zhang, G., Ge, S., & Wang, C. Y. (2017). Modeling of lithium plating induced aging of lithium-ion batteries: Transition from linear to nonlinear aging. *Journal of Power Sources, 360*, 28-40.

[17] Hendricks, C., Williard, N., Mathew, S., & Pecht, M. (2015). A failure modes, mechanisms, and effects analysis (FMMEA) of lithium-ion batteries. *Journal of Power Sources, 297*, 113-120.

[18] Khan, S., & Yairi, T. (2018). A review on the application of deep learning in system health management. *Mechanical Systems and Signal Processing, 107*, 241-265.

[19] He, W., Williard, N., Osterman, M., & Pecht, M. (2011). Prognostics of lithium-ion batteries based on Dempster–Shafer theory and the Bayesian Monte Carlo method. *Journal of Power Sources, 196(23)*, 10314-10321.

[20] Wang, D., Yang, F., Tsui, K. L., Zhou, Q., & Bae, S. J. (2016). Remaining useful life prediction of lithium-ion batteries based on spherical cubature particle filter. *IEEE Transactions on Instrumentation and Measurement, 65(6)*, 1282-1291.

[21] Qian, C., Xu, B., Xia, Q., Ren, Y., Sun, B., & Wang, Z. (2023). SOH prediction for Lithium-Ion batteries by using historical state and future load information with an AM-seq2seq model. *Applied Energy, 336*, 120793.

[22] Naumann, M., Spingler, F. B., & Jossen, A. (2020). Analysis and modeling of cycle aging of a commercial LiFePO4/graphite cell. *Journal of Power Sources, 451*, 227666.

[23] Barcellona, S., & Piegari, L. (2020). Effect of current on cycle aging of lithium ion batteries. *Journal of Energy Storage, 29*, 101310.

[24] Doerffel, D., & Sharkh, S. A. (2006). A critical review of using the Peukert equation for determining the remaining capacity of lead-acid and lithium-ion batteries. *Journal of power sources, 155(2)*, 395-400.

[25] Zhang, Q., Cui, N., Zhou, Z., Shang, Y., & Duan, B. (2022). Critical review and analysis of available capacity estimation of $LiFePO_4$ battery using Peukert's law: A case study. *International Journal of Energy Research, 46(15)*, 23808-23823.

[26] Li, Y., Abdel-Monem, M., Gopalakrishnan, R., Berecibar, M., Nanini-Maury, E., Omar, N., ... & Van Mierlo, J. (2018). A quick on-line state of health estimation method for Li-ion battery with incremental capacity curves processed by Gaussian filter. *Journal of Power Sources, 373*, 40-53.

[27] Zhang, S., Guo, X., Dou, X., & Zhang, X. (2020). A rapid online calculation method for state of health of lithium-ion battery based on coulomb counting method and differential voltage analysis. *Journal of Power Sources, 479*, 228740.

[28] Sun, H., Wen, X., Liu, W., Wang, Z., & Liao, Q. (2022). State-of-health estimation of retired lithium-ion battery module aged at 1C-rate. *Journal of Energy Storage, 50*, 104618.

[29] He, J., Wei, Z., Bian, X., & Yan, F. (2020). State-of-health estimation of lithium-ion batteries using incremental capacity analysis based on voltage–capacity model. *IEEE Transactions on Transportation Electrification, 6(2)*, 417-426.

[30] Li, X., Wang, Z., Zhang, L., Zou, C., & Dorrell, D. D. (2019). State-of-health estimation for Li-ion batteries by combing the incremental capacity analysis method with grey relational analysis. *Journal of Power Sources, 410*, 106-114.

[31] Maures, M., Capitaine, A., Delétage, J. Y., Vinassa, J. M., & Briat, O. (2020). Lithium-ion battery SOH estimation based on incremental capacity peak tracking at several current levels for online application. *Microelectronics Reliability*, *114*, 113798.

[32] Pan, W., Luo, X., Zhu, M., Ye, J., Gong, L., & Qu, H. (2021). A health indicator extraction and optimization for capacity estimation of Li-ion battery using incremental capacity curves. *Journal of Energy Storage*, *42*, 103072.

[33] He, J., Bian, X., Liu, L., Wei, Z., & Yan, F. (2020). Comparative study of curve determination methods for incremental capacity analysis and state of health estimation of lithium-ion battery. *Journal of Energy Storage*, *29*, 101400.

[34] Micea, M. V., Ungurean, L., Cârstoiu, G. N., & Groza, V. (2011). Online state-of-health assessment for battery management systems. *IEEE Transactions on Instrumentation and Measurement*, *60(6)*, 1997-2006.

[35] Xing, Y., Ma, E. W., Tsui, K. L., & Pecht, M. (2013). An ensemble model for predicting the remaining useful performance of lithium-ion batteries. *Microelectronics reliability*, *53(6)*, 811-820.

[36] Yang, F., Wang, D., Xing, Y., & Tsui, K. L. (2017). Prognostics of Li (NiMnCo) O2-based lithium-ion batteries using a novel battery degradation model. *Microelectronics Reliability*, *70*, 70-78.

[37] Wang, H., Ma, X., & Zhao, Y. (2020). A mixed-effects model of two-phase degradation process for reliability assessment and RUL prediction. *Microelectronics Reliability*, *107*, 113622.

[38] Lin, J., Liao, G., Chen, M., & Yin, H. (2021). Two-phase degradation modeling and remaining useful life prediction using nonlinear wiener process. *Computers & Industrial Engineering*, *160*, 107533.

[39] Shen, D., Wu, L., Kang, G., Guan, Y., & Peng, Z. (2021). A novel online method for predicting the remaining useful life of lithium-ion batteries considering random variable discharge current. *Energy*, *218*, 119490.

[40] Zhang, Y., Chen, L., Li, Y., Zheng, X., Chen, J., & Jin, J. (2021). A hybrid approach for remaining useful life prediction of lithium-ion battery with Adaptive Levy Flight optimized Particle Filter and Long Short-Term Memory network. *Journal of Energy Storage*, *44*, 103245.

[41] Tong, Z., Miao, J., Tong, S., & Lu, Y. (2021). Early prediction of remaining useful life for Lithium-ion batteries based on a hybrid machine learning method. *Journal of Cleaner Production*, *317*, 128265.

[42] Lai, X., Huang, Y., Han, X., Gu, H., & Zheng, Y. (2021). A novel method for state of energy estimation of lithium-ion batteries using particle filter and extended Kalman filter. *Journal of Energy Storage*, *43*, 103269.

[43] Li, X., Zeng, T., Qin, H., Huo, R., Liu, Y., Wei, D., & Ding, X. (2021). Investigation of inhomogeneous degradation in large-format lithium-ion batteries. Journal of Energy Storage, 42, 103113.

[44] Yao, F., He, W., Wu, Y., Ding, F., & Meng, D. (2022). Remaining useful life prediction of lithium-ion batteries using a hybrid model. *Energy, 248*, 123622.

[45] Messing, M., Shoa, T., & Habibi, S. (2021). Estimating battery state of health using electrochemical impedance spectroscopy and the relaxation effect. *Journal of Energy Storage, 43*, 103210.

[46] Qian, K., Huang, B., Ran, A., He, Y. B., Li, B., & Kang, F. (2019). State-of-health (SOH) evaluation on lithium-ion battery by simulating the voltage relaxation curves. *Electrochimica Acta, 303*, 183-191.

[47] Fang, Q., Wei, X., Lu, T., Dai, H., & Zhu, J. (2019). A state of health estimation method for lithium-ion batteries based on voltage relaxation model. *Energies, 12(7)*, 1349.

[48] Baghdadi, I., Briat, O., Gyan, P., & Vinassa, J. M. (2016). State of health assessment for lithium batteries based on voltage–time relaxation measure. *Electrochimica Acta, 194*, 461-472.

[49] Eddahech, A., Briat, O., Woirgard, E., & Vinassa, J. M. (2012). Remaining useful life prediction of lithium batteries in calendar ageing for automotive applications. *Microelectronics Reliability, 52(9-10)*, 2438-2442.

[50] Virkar, A. V. (2011). A model for degradation of electrochemical devices based on linear non-equilibrium thermodynamics and its application to lithium ion batteries. *Journal of Power Sources, 196(14)*, 5970-5984.

[51] Khumprom, P., & Yodo, N. (2019). A data-driven predictive prognostic model for lithium-ion batteries based on a deep learning algorithm. *Energies, 12(4)*, 660.

[52] Zhou, Y., Huang, M., Chen, Y., & Tao, Y. (2016). A novel health indicator for on-line lithium-ion batteries remaining useful life prediction. *Journal of Power Sources, 321*, 1-10.

[53] Klass, V., Behm, M., & Lindbergh, G. (2014). A support vector machine-based state-of-health estimation method for lithium-ion batteries under electric vehicle operation. *Journal of Power Sources, 270*, 262-272.

[54] Xue, Z., Zhang, Y., Cheng, C., & Ma, G. (2020). Remaining useful life prediction of lithium-ion batteries with adaptive unscented kalman filter and optimized support vector regression. *Neurocomputing, 376*, 95-102.

[55] Patil, M. A., Tagade, P., Hariharan, K. S., Kolake, S. M., Song, T., Yeo, T., & Doo, S. (2015). A novel multistage Support Vector Machine based approach for Li ion battery remaining useful life estimation. *Applied energy, 159*, 285-297.

[56] Li, X., Zhang, L., Wang, Z., & Dong, P. (2019). Remaining useful life prediction for lithium-ion batteries based on a hybrid model combining the long short-term memory and Elman neural networks. *Journal of Energy Storage, 21*, 510-518.

[57] Liu, C., Wang, Y., & Chen, Z. (2019). Degradation model and cycle life prediction for lithium-ion battery used in hybrid energy storage system. *Energy, 166*, 796-806.

[58] Liu, T., Sun, Q., Feng, J., Pan, Z., & Huangpeng, Q. (2017). Residual life estimation under time-varying conditions based on a Wiener process. *Journal of statistical computation and simulation, 87(2)*, 211-226.

[59] Yang, D., Zhang, X., Pan, R., Wang, Y., & Chen, Z. (2018). A novel Gaussian process regression model for state-of-health estimation of lithium-ion battery using charging curve. *Journal of Power Sources, 384*, 387-395.

[60] Guha, A., & Patra, A. (2018). Online estimation of the electrochemical impedance spectrum and remaining useful life of lithium-ion batteries. *IEEE Transactions on Instrumentation and Measurement, 67(8)*, 1836-1849.

[61] Lyu, C., Lai, Q., Ge, T., Yu, H., Wang, L., & Ma, N. (2017). A lead-acid battery's remaining useful life prediction by using electrochemical model in the Particle Filtering framework. *Energy, 120*, 975-984.

[62] Xu, B., Oudalov, A., Ulbig, A., Andersson, G., & Kirschen, D. S. (2016). Modeling of lithium-ion battery degradation for cell life assessment. *IEEE Transactions on Smart Grid, 9(2)*, 1131-1140.

[63] Tran, M. K., Mathew, M., Janhunen, S., Panchal, S., Raahemifar, K., Fraser, R., & Fowler, M. (2021). A comprehensive equivalent circuit model for lithium-ion batteries, incorporating the effects of state of health, state of charge, and temperature on model parameters. *Journal of Energy Storage, 43*, 103252.

[64] Xia, B., Sun, Z., Zhang, R., & Lao, Z. (2017). A cubature particle filter algorithm to estimate the state of the charge of lithium-ion batteries based on a second-order equivalent circuit model. *Energies, 10(4)*, 457.

[65] Feng, T., Yang, L., Zhao, X., Zhang, H., & Qiang, J. (2015). Online identification of lithium-ion battery parameters based on an improved equivalent-circuit model and its implementation on battery state-of-power prediction. *Journal of Power Sources, 281*, 192-203.

[66] Wang, Y., Tian, J., Sun, Z., Wang, L., Xu, R., Li, M., & Chen, Z. (2020). A comprehensive review of battery modeling and state estimation approaches for advanced battery management systems. *Renewable and Sustainable Energy Reviews, 131*, 110015.

[67] Doyle, M., Fuller, T. F., & Newman, J. (1993). Modeling of galvanostatic charge and discharge of the lithium/polymer/insertion cell. *Journal of the Electrochemical society, 140(6)*, 1526.

[68] Zhang, Q., Wang, D., Yang, B., Cui, X., & Li, X. (2020). Electrochemical model of lithium-ion battery for wide frequency range applications. *Electrochimica Acta, 343*, 136094.

[69] Liu, Q., Zhang, J., Li, K., & Lv, C. (2020). The remaining useful life prediction by using electrochemical model in the particle filter framework for lithium-ion batteries. *IEEE Access, 8*, 126661-126670.

[70] Sadabadi, K. K., Jin, X., & Rizzoni, G. (2021). Prediction of remaining useful life for a composite electrode lithium ion battery cell using an electrochemical model to estimate the state of health. *Journal of Power Sources, 481*, 228861.

[71] Tran, M. K., & Fowler, M. (2020). A review of lithium-ion battery fault diagnostic algorithms: Current progress and future challenges. *Algorithms, 13(3)*, 62.

[72] Wei, H., Chen, X., Zhiqiang, L., Wang, Z., Pan, H., & CHEN, L. (2017). Online estimation of lithium-ion battery state of health using grey neural network. *Power Syst. Technol, 41*, 4038-4044.

[73] Panchal, S., Mcgrory, J., Kong, J., Fraser, R., Fowler, M., Dincer, I., & Agelin‐Chaab, M. (2017). Cycling degradation testing and analysis of a LiFePO4 battery at actual conditions. *International Journal of Energy Research, 41(15)*, 2565-2575.

[74] He, H., Xiong, R., Guo, H., & Li, S. (2012). Comparison study on the battery models used for the energy management of batteries in electric vehicles. *Energy Conversion and Management, 64*, 113-121.

[75] Shi, E., Xia, F., Peng, D., Li, L., Wang, X., & Yu, B. (2019). State-of-health estimation for lithium battery in electric vehicles based on improved unscented particle filter. Journal of *Renewable and Sustainable Energy, 11(2)*.

[76] Zhang, J., Liu, X., Chen, C., & Simeone, A. (2020). An intelligent deformation‐based approach to the state of health estimation of collided lithium‐ion batteries for facilitating battery module safety evaluation. *Energy Technology, 8(11)*, 2000624.

[77] Li, Y., & Tao, J. (2020). CNN and transfer learning based online SOH estimation for lithium-ion battery. *In 2020 Chinese Control and Decision Conference (CCDC), IEEE*, 5489-5494.

[78] Ansari, S., Ayob, A., Hossain Lipu, M. S., Hussain, A., & Saad, M. H. M. (2021). Data-driven remaining useful life prediction for lithium-ion batteries using multi-charging profile framework: A recurrent neural network approach. *Sustainability, 13(23)*, 13333.

[79] Park, K., Choi, Y., Choi, W. J., Ryu, H. Y., & Kim, H. (2020). LSTM-based battery remaining useful life prediction with multi-channel charging profiles. *IEEE Access, 8*, 20786-20798.

[80] Bonfitto, A. (2020). A method for the combined estimation of battery state of charge and state of health based on artificial neural networks. *Energies, 13(10)*, 2548.

[81] Ansari, S., Ayob, A., Hossain Lipu, M. S., Hussain, A., & Saad, M. H. M. (2021). Multi-channel profile based artificial neural network approach for remaining useful life prediction of electric vehicle lithium-ion batteries. *Energies, 14(22)*, 7521.

[82] Zhang, S., Zhai, B., Guo, X., Wang, K., Peng, N., & Zhang, X. (2019). Synchronous estimation of state of health and remaining useful lifetime for lithium-ion battery using the incremental capacity and artificial neural networks. *Journal of Energy Storage, 26*, 100951.

[83] Wu, J., Zhang, C., & Chen, Z. (2016). An online method for lithium-ion battery remaining useful life estimation using importance sampling and neural networks. *Applied energy, 173*, 134-140.

[84] Kong, J. Z., Yang, F., Zhang, X., Pan, E., Peng, Z., & Wang, D. (2021). Voltage-temperature health feature extraction to improve prognostics and health management of lithium-ion batteries. *Energy, 223*, 120114.

[85] Liu, W., & Xu, Y. (2020). Data-driven online health estimation of Li-ion batteries using a novel energy-based health indicator. *IEEE Transactions on Energy Conversion, 35(3)*, 1715-1718.

[86] Ren, L., Dong, J., Wang, X., Meng, Z., Zhao, L., & Deen, M. J. (2020). A data-driven auto-CNN-LSTM prediction model for lithium-ion battery remaining useful life. *IEEE Transactions on Industrial Informatics, 17(5)*, 3478-3487.

[87] Li, D., & Yang, L. (2021). Remaining useful life prediction of lithium battery based on sequential CNN–LSTM method. *Journal of Electrochemical Energy Conversion and Storage, 18(4)*, 041005.

[88] Kara, A. (2021). A data-driven approach based on deep neural networks for lithium-ion battery prognostics. *Neural Computing and Applications, 33(20)*, 13525-13538.

[89] Zhang, Y., Xiong, R., He, H., & Liu, Z. (2017). A LSTM-RNN method for the lithuim-ion battery remaining useful life prediction. *In 2017 Prognostics and System Health Management Conference (PHM-Harbin)*, IEEE, 1-4.

[90] Song, Y., Li, L., Peng, Y., & Liu, D. (2018). Lithium-ion battery remaining useful life prediction based on GRU-RNN. *In 2018 12th international conference on reliability, maintainability, and safety (icrms)*, IEEE, 317-322.

[91] Nuhic, A., Terzimehic, T., Soczka-Guth, T., Buchholz, M., & Dietmayer, K. (2013). Health diagnosis and remaining useful life prognostics of lithium-ion batteries using data-driven methods. *Journal of power sources, 239*, 680-688.

[92] Widodo, A., Shim, M. C., Caesarendra, W., & Yang, B. S. (2011). Intelligent prognostics for battery health monitoring based on sample entropy. *Expert Systems with Applications, 38(9)*, 11763-11769.

[93] Zhang, Z., Huang, M., Chen, Y., & Zhu, S. (2016). Prediction of Lithium-ion battery's remaining useful life based on relevance vector machine. *SAE International Journal of Alternative Powertrains, 5(1)*, 30-40.

[94] Gong, Y., Zhang, X., Li, H., Liao, H., Meng, Z., Liu, Y., & Huang, Z. (2020). Estimation of Peukert constant of lithium-ion batteries and its application in battery discharging time prediction. *In 2020 IEEE Energy Conversion Congress and Exposition (ECCE)*, IEEE, 905-910.

[95] Nebl, C., Kotzur, F. O., Koch, D., & Schweiger, H. G. (2020). Prediction of constant power delivery of lithium-ion cells at high loads. *Journal of Energy Storage, 30*, 101552.

[96] Ioannou, S., Dalamagkidis, K., Stefanakos, E. K., Valavanis, K. P., & Wiley, P. H. (2016, June). Runtime, capacity and discharge current relationship for lead acid and lithium batteries. *In 2016 24th Mediterranean Conference on Control and Automation (MED)*, IEEE, 46-53.

[97] Yang, A., Wang, Y., Yang, F., Wang, D., Zi, Y., Tsui, K. L., & Zhang, B. (2019). A comprehensive investigation of lithium-ion battery degradation performance at different discharge rates. *Journal of Power Sources, 443*, 227108.

[98] Omar, N., Van den Bossche, P., Coosemans, T., & Van Mierlo, J. (2013). Peukert revisited—Critical appraisal and need for modification for lithium-ion batteries. *Energies, 6(11)*, 5625-5641.

[99] Leksono, E., Haq, I. N., Iqbal, M., Soelami, F. N., & Merthayasa, I. G. N. (2013, November). State of charge (SoC) estimation on LiFePO 4 battery module using Coulomb counting methods with modified Peukert. *In 2013 Joint International Conference on Rural Information & Communication Technology and Electric-Vehicle Technology (rICT & ICeV-T)*, IEEE, 1-4.

[100] Jiang, Y., Jiang, J., Zhang, C., Zhang, W., Gao, Y., & Li, N. (2018). State of health estimation of second-life LiFePO4 batteries for energy storage applications. *Journal of cleaner production, 205*, 754-762.

[101] Xia, F., Wang, K., & Chen, J. (2023). State of health and remaining useful life prediction of lithium-ion batteries based on a disturbance-free incremental capacity and differential voltage analysis method. *Journal of Energy Storage, 64*, 107161.

[102] Wang, L., Zhao, X., Liu, L., & Pan, C. (2017). State of health estimation of battery modules via differential voltage analysis with local data symmetry method. *Electrochimica Acta, 256*, 81-89.

[103] Zhou, Z., Duan, B., Kang, Y., Zhang, Q., Shang, Y., & Zhang, C. (2023). Online state of health estimation for seriesconnected LiFePO4 battery pack based on differential voltage and inconsistency analysis. *IEEE Transactions on Transportation Electrification*.

[104] Wang, R., & Feng, H. (2020). Lithium-ion batteries remaining useful life prediction using Wiener process and unscented particle filter. *Journal of power electronics*, *20*, 270-278.

[105] Chen, Y., He, Y., Li, Z., Chen, L., & Zhang, C. (2020). Remaining useful life prediction and state of health diagnosis of lithium-ion battery based on second-order central difference particle filter. *IEEE Access, 8*, 37305-37313.

[106] Duan, B., Zhang, Q., Geng, F., & Zhang, C. (2020). Remaining useful life prediction of lithium‐ion battery based on extended Kalman particle filter. *International Journal of Energy Research, 44(3)*, 1724-1734.

[107] Cai, H., Feng, J., Li, W., Hsu, Y. M., & Lee, J. (2020). Similarity-based particle filter for remaining useful life prediction with enhanced performance. *Applied Soft Computing, 94*, 106474.

[108] Kim, S., Park, H. J., Choi, J. H., & Kwon, D. (2020). A novel prognostics approach using shifting kernel particle filter of Li-ion batteries under state changes. *IEEE Transactions on Industrial Electronics, 68(4)*, 3485-3493.

[109] Zheng, X., & Fang, H. (2015). An integrated unscented kalman filter and relevance vector regression approach for lithium-ion battery remaining useful life and short-term capacity prediction. *Reliability Engineering & System Safety, 144*, 74-82.

[110] Zhang, H., Miao, Q., Zhang, X., & Liu, Z. (2018). An improved unscented particle filter approach for lithium-ion battery remaining useful life prediction. *Microelectronics Reliability, 81*, 288-298.

[111] Hu, Y., & Zhu, M. (2022). System Reliability Models with Random Shocks and Uncertainty: A State-of-the-Art Review. *Predictive Analytics in System Reliability*, 19-38.

[112] Lin, W., & Chai, Y. (2023). Remaining useful life prediction for nonlinear two-phase degradation process with measurement errors and imperfect prior information. *Measurement Science and Technology, 34(5)*, 055018.

[113] Xu, X., Tang, S., Yu, C., Xie, J., Han, X., & Ouyang, M. (2021). Remaining useful life prediction of lithium-ion batteries based on wiener process under time-varying temperature condition. *Reliability Engineering & System Safety, 214*, 107675.

[114] Tang, S., Yu, C., Wang, X., Guo, X., & Si, X. (2014). Remaining useful life prediction of lithium-ion batteries based on the wiener process with measurement error. *Energies, 7(2)*, 520-547.

[115] Kong, J. Z., Wang, D., Yan, T., Zhu, J., & Zhang, X. (2021). Accelerated stress factors based nonlinear Wiener process model for lithium-ion battery prognostics. *IEEE Transactions on Industrial Electronics, 69(11)*, 11665-11674.

[116] Zhang, S., Zhai, Q., & Li, Y. (2023). Degradation modeling and RUL prediction with Wiener process considering measurable and unobservable external impacts. *Reliability Engineering & System Safety, 231*, 109021.

[117] Zhang, J. X., Hu, C. H., He, X., Si, X. S., Liu, Y., & Zhou, D. H. (2018). A novel lifetime estimation method for two-phase degrading systems. *IEEE Transactions on Reliability, 68(2)*, 689-709.

[118] Wen, Y., Wu, J., Das, D., & Tseng, T. L. B. (2018). Degradation modeling and RUL prediction using Wiener process subject to multiple change points and unit heterogeneity. *Reliability Engineering & System Safety, 176*, 113-124.

[119] Liao, G., Yin, H., Chen, M., & Lin, Z. (2021). Remaining useful life prediction for multi-phase deteriorating process based on Wiener process. *Reliability Engineering & System Safety, 207*, 107361.

[120] Ouyang, D., Weng, J., Chen, M., & Wang, J. (2020). Impact of high-temperature environment on the optimal cycle rate of lithium-ion battery. *Journal of Energy Storage, 28*, 101242.

[121] Mevawalla, A., Panchal, S., Tran, M. K., Fowler, M., & Fraser, R. (2021). One dimensional fast computational partial differential model for heat transfer in lithium-ion batteries. *Journal of Energy Storage, 37*, 102471.

[122] Ye, X., Zhao, Y., & Quan, Z. (2018). Thermal management system of lithium-ion battery module based on micro heat pipe array. *International Journal of Energy Research, 42(2)*, 648-655.

[123] Ruan, H., He, H., Wei, Z., Quan, Z., & Li, Y. (2021). State of health estimation of lithium-ion battery based on constant-voltage charging reconstruction. *IEEE Journal of Emerging and Selected Topics in Power Electronics, 11(4)*, 4393-4402.

[124] Wang, D., Yang, F., Zhao, Y., & Tsui, K. L. (2017). Battery remaining useful life prediction at different discharge rates. *Microelectronics Reliability, 78*, 212-219.

[125] Lamrani, B., Lebrouhi, B. E., Khattari, Y., & Kousksou, T. (2021). A simplified thermal model for a lithium-ion battery pack with phase change material thermal management system. *Journal of Energy Storage, 44*, 103377.

[126] Messing, M., Shoa, T., & Habibi, S. (2021). Electrochemical impedance spectroscopy with practical rest-times for battery management applications. *IEEE Access, 9*, 66989-66998.

[127] Sieg, J., Storch, M., Fath, J., Nuhic, A., Bandlow, J., Spier, B., & Sauer, D. U. (2020). Local degradation and differential voltage analysis of aged lithium-ion pouch cells. *Journal of Energy Storage, 30*, 101582.

[128] Dos Reis, G., Strange, C., Yadav, M., & Li, S. (2021). Lithium-ion battery data and where to find it. Energy and AI, 5, 100081.

[129] Saha, B., & Goebel, K. (2007). Battery data set. *NASA AMES prognostics data repository*.

[130] Raj, T., Wang, A. A., Monroe, C. W., & Howey, D. A. (2020). Investigation of path-dependent degradation in lithium-ion batteries. *Batteries & Supercaps, 3(12)*, 1377-1385.

[131] Severson, K. A., Attia, P. M., Jin, N., Perkins, N., Jiang, B., Yang, Z., ... & Braatz, R. D. (2019). Data-driven prediction of battery cycle life before capacity degradation. *Nature Energy, 4(5)*, 383-391.

[132] Lu, L., Han, X., Li, J., Hua, J., & Ouyang, M. (2013). A review on the key issues for lithium-ion battery management in electric vehicles. *Journal of power sources, 226*, 272-288.

[133] Yang, F., Wang, D., Zhao, Y., Tsui, K. L., & Bae, S. J. (2018). A study of the relationship between coulombic efficiency and capacity degradation of commercial lithium-ion batteries. *Energy, 145*, 486-495.

[134] Deng, Z., Yang, L., Cai, Y., Deng, H., & Sun, L. (2016). Online available capacity prediction and state of charge estimation based on advanced data-driven algorithms for lithium iron phosphate battery. *Energy, 112*, 469-480.

[135] Wang, R., & Zhu, M. (2022). Shock-loading-based reliability modeling with dependent degradation processes and random shocks. *International Journal of Reliability, Quality and Safety Engineering, 29(03)*, 2250002.

[136] Zhu, M. (2022). A new framework of complex system reliability with imperfect maintenance policy. *Annals of Operations Research, 312(1)*, 553-579.

[137] Li, X., Ding, Q., & Sun, J. Q. (2018). Remaining useful life estimation in prognostics using deep convolution neural networks. *Reliability Engineering & System Safety, 172*, 1-11.

[138] Motulsky, H. J., & Ransnas, L. A. (1987). Fitting curves to data using nonlinear regression: a practical and nonmathematical review. *The FASEB journal, 1(5)*, 365-374.

[139] Shibata, R. (1976). Selection of the order of an autoregressive model by Akaike's information criterion. *Biometrika, 63(1)*, 117-126.

[140] Qu, X., Song, Y., Liu, D., Cui, X., & Peng, Y. (2020). Lithium-ion battery performance degradation evaluation in dynamic operating conditions based on a digital twin model. *Microelectronics Reliability, 114*, 113857.

[141] Pang, X., Liu, X., Jia, J., Wen, J., Shi, Y., Zeng, J., & Zhao, Z. (2021). A lithium-ion battery remaining useful life prediction method based on the incremental capacity analysis and Gaussian process regression. *Microelectronics Reliability*, *127*, 114405.

[142] Harvey, L. D. (2020). Rethinking electric vehicle subsidies, rediscovering energy efficiency. *Energy policy*, *146*, 111760.

[143] Xu, B., Diao, W., Wen, G., Choe, S. Y., Kim, J., & Pecht, M. (2021). Decoupling the thermal and non-thermal effects of discharge C-rate on the capacity fade of lithium-ion batteries. *Journal of Power Sources*, *510*, 230390.

[144] Malavé, V., Berger, J. R., Zhu, H., & Kee, R. J. (2014). A computational model of the mechanical behavior within reconstructed LixCoO2 Li-ion battery cathode particles. *Electrochimica Acta*, *130*, 707-717.

[145] Qu, J. G., Jiang, Z. Y., & Zhang, J. F. (2022). Investigation on lithium-ion battery degradation induced by combined effect of current rate and operating temperature during fast charging. *Journal of Energy Storage*, *52*, 104811.

[146] Collath, N., Tepe, B., Englberger, S., Jossen, A., & Hesse, H. (2022). Aging aware operation of lithium-ion battery energy storage systems: A review. *Journal of Energy Storage*, *55*, 105634.

[147] Hu, Y., Wang, R., Zhu, M., & Chen, K. B. (2023). Modeling Human-Machine Interaction System Reliability with Multiple Dependent Degradation Processes and Situation Awareness. *International Journal of Reliability, Quality and Safety Engineering*, 30(04), 2350014.

[148] Ma, Y., Shan, C., Gao, J., & Chen, H. (2022). A novel method for state of health estimation of lithium-ion batteries based on improved LSTM and health indicators extraction. *Energy*, *251*, 123973.

[149] Wang, R & Zhu, M (2023). Experimental analysis of Lithium-ion battery degradation with varying discharge rates. *Proceedings of the 28th ISSAT International Conference on Reliability and Quality in Design, San Francisco*, CA, 37-41.

[150] Cohen, I., Huang, Y., Chen, J., Benesty, J., Benesty, J., Chen, J., ... & Cohen, I. (2009). Pearson correlation coefficient. Noise reduction in speech processing, 1-4.

[151] Killick, R., Fearnhead, P., & Eckley, I. A. (2012). Optimal detection of changepoints with a linear computational cost. *Journal of the American Statistical Association*, *107(500)*, 1590-1598.

[152] Wang, H., Song, W., Zio, E., Kudreyko, A., & Zhang, Y. (2020). Remaining useful life prediction for Lithium-ion batteries using fractional Brownian motion and Fruit-fly Optimization Algorithm. *Measurement*, *161*, 107904.

[153] Jarque, C. M., & Bera, A. K. (1980). Efficient tests for normality, homoscedasticity and serial independence of regression residuals. *Economics letters*, *6(3)*, 255-259.

[154] De Freitas, N., & Gordon, N. J. (2001). Sequential Monte Carlo methods in practice (Vol. 1, No. 2, p. 2). A. Doucet (Ed.). New York: Springer.

[155] Cadini, F., Zio, E., & Avram, D. I. A. N. A. (2009). Monte Carlo-based filtering for fatigue crack growth estimation. *Probabilistic Engineering Mechanics*, *24(3)*, 367-373.

[156] Li, T., Bolic, M., & Djuric, P. M. (2015). Resampling methods for particle filtering: classification, implementation, and strategies. *IEEE Signal processing magazine, 32(3),* 70-86.
[157] Atalay, S., Sheikh, M., Mariani, A., Merla, Y., Bower, E., & Widanage, W. D. (2020). Theory of battery ageing in a lithium-ion battery: Capacity fade, nonlinear ageing and lifetime prediction. *Journal of Power Sources, 478,* 229026.
[158] Pang, X., Huang, R., Wen, J., Shi, Y., Jia, J., & Zeng, J. (2019). A lithium-ion battery RUL prediction method considering the capacity regeneration phenomenon. *Energies, 12(12),* 2247.
[159] Johnen, M., Pitzen, S., Kamps, U., Kateri, M., Dechent, P., & Sauer, D. U. (2021). Modeling long-term capacity degradation of lithium-ion batteries. *Journal of Energy Storage, 34,* 102011.
[160] Pozzato, G., Allam, A., & Onori, S. (2022). Lithium-ion battery aging dataset based on electric vehicle real-driving profiles. *Data in Brief, 41,* 107995.
[161] Liu, Y., Zhao, G., & Peng, X. (2019). Deep learning prognostics for lithium-ion battery based on ensembled long short-term memory networks. *IEEE Access, 7,* 155130-155142.
[162] Meng, H., & Li, Y. F. (2019). A review on prognostics and health management (PHM) methods of lithium-ion batteries. *Renewable and Sustainable Energy Reviews, 116,* 109405.
[163] Wang, R. & Zhu, M. (2022). Shock-loading based method for modeling dependent competing risks with degradation processes and random shocks. *International Journal of Reliability, Quality and Safety Engineering, 29 (3),* 2250002.
[164] Song, S., Coit, D. W., & Feng, Q. (2014). Reliability for systems of degrading components with distinct component shock sets. *Reliability Engineering & System Safety, 132,* 115-124.
[165] Zhu, M., & Pham, H. (2019). A novel system reliability modeling of hardware, software, and interactions of hardware and software. Mathematics, 7(11), 1049.
[166] Chen, X., Liu, Z., Wang, J., Yang, C., Long, B., & Zhou, X. (2021). An adaptive prediction model for the remaining life of an Li-ion battery based on the fusion of the two-phase Wiener process and an extreme learning machine. *Electronics, 10(5),* 540.
[167] Deng, Z., Hu, X., Lin, X., Xu, L., Che, Y., & Hu, L. (2020). General discharge voltage information enabled health evaluation for lithium-ion batteries. *IEEE/ASME Transactions on Mechatronics, 26(3),* 1295-1306.
[168] Liu, D., Wang, H., Peng, Y., Xie, W., & Liao, H. (2013). Satellite lithium-ion battery remaining cycle life prediction with novel indirect health indicator extraction. *Energies, 6(8),* 3654-3668.
[169] Liu, D., Zhou, J., Liao, H., Peng, Y., & Peng, X. (2015). A health indicator extraction and optimization framework for lithium-ion battery degradation modeling and prognostics. *IEEE Transactions on Systems, Man, and Cybernetics: Systems, 45(6),* 915-928.
[170] Liu, D., Song, Y., Li, L., Liao, H., & Peng, Y. (2018). On-line life cycle health assessment for lithium-ion battery in electric vehicles. *Journal of cleaner production, 199,* 1050-1065.
[171] Lines, J., & Bagnall, A. (2015). Time series classification with ensembles of elastic distance measures. *Data Mining and Knowledge Discovery, 29(3),* 565-592.

[172] Sharabiani, A., Darabi, H., Rezaei, A., Harford, S., Johnson, H., & Karim, F. (2017). Efficient classification of long time series by 3-d dynamic time warping. *IEEE Transactions on Systems, Man, and Cybernetics: Systems, 47(10)*, 2688-2703.

[173] Lee, D., & Seung, H. S. (2000). Algorithms for non-negative matrix factorization. *Advances in neural information processing systems, 13*.

[174] Berry, M. W., Browne, M., Langville, A. N., Pauca, V. P., & Plemmons, R. J. (2007). Algorithms and applications for approximate nonnegative matrix factorization. *Computational Statistics & Data Analysis, 52(1)*, 155-173.

[175] Lu, Y., Yuan, C., Zhu, W., & Li, X. (2018). Structurally incoherent low-rank nonnegative matrix factorization for image classification. *IEEE Transactions on Image Processing, 27(11)*, 5248-5260.

[176] Ding, C., He, X., & Simon, H. D. (2005). On the equivalence of nonnegative matrix factorization and spectral clustering. *In Proceedings of the 2005 SIAM International Conference on Data Mining*, *Society for Industrial and Applied Mathematics*, 606-610.

[177] Si, X. S., Wang, W., Hu, C. H., Zhou, D. H., & Pecht, M. G. (2012). Remaining useful life estimation based on a nonlinear diffusion degradation process. *IEEE Transactions on Reliability, 61(1)*, 50-67.

[178] Antolín, D., Medrano, N., Calvo, B., & Pérez, F. (2017). A wearable wireless sensor network for indoor smart environment monitoring in safety applications. *Sensors, 17(2)*, 365.

[179] Praveen, S., Santhoshkumar, P., Joe, Y. C., Senthil, C., & Lee, C. W. (2020). 3D-printed architecture of Li-ion batteries and its applications to smart wearable electronic devices. *Applied Materials Today, 20*, 100688.

[180] Li, S., Wu, Y., Ma, X., Hu, J., Song, Q., Shen, X., & Zhang, W. (2023). Organic phase change composite separators to enhance the safety performance of lithium-ion batteries. *Journal of Power Sources, 584*, 233620.

[181] Meng, H., Geng, M., Xing, J., & Zio, E. (2022). A hybrid method for prognostics of lithium-ion batteries capacity considering regeneration phenomena. *Energy, 261*, 125278.

[182] Duong, P. L. T., & Raghavan, N. (2018). Heuristic Kalman optimized particle filter for remaining useful life prediction of lithium-ion battery. *Microelectronics Reliability, 81*, 232-243.

[183] Li, L. L., Liu, Z. F., Tseng, M. L., & Chiu, A. S. (2019). Enhancing the Lithium-ion battery life predictability using a hybrid method. *Applied Soft Computing, 74*, 110-121.

APPENDICES

Appendix A

Based on Theorem 3 in study [49], the expressions are obtained in two stages, in which τ is obtained from NMF to represent the time at CP and $p(a_i)$ represents the PDF of random variable $a_i,\ i = 1$ or 2.

The first stage: If $0 < t < \tau$, then

$$f_T(t) = \int_{-\infty}^{\infty} f_T(t|a_1)p(a_1)da_1$$
$$\cong \frac{1}{\sqrt{2\pi t^2\left(\sigma_{a_1}^2\left(\int_0^t u_1(t_1,\theta_1)dt_1\right)^2+\sigma_1^2 t\right)}} \times \left[\omega - \left(\int_0^t u_1(t_1,\theta_1)dt_1 - u_1(t,\theta_1)t\right) \times \right.$$
$$\left. \frac{\omega\sigma_{a_1}^2 \int_0^t u_1(t_1,\theta_1)dt_1 + u_{a_1}\sigma_1^2 t}{\sigma_{a_1}^2\left(\int_0^t u_1(t_1,\theta_1)dt_1\right)^2+\sigma_1^2 t}\right] \times \exp\left(\frac{\left(\omega - u_{a_1}\int_0^t u_1(t_1,\theta_1)dt_1\right)^2}{2\left(\sigma_{a_1}^2\left(\int_0^t u_1(t_1,\theta_1)dt_1\right)^2+\sigma_1^2 t\right)}\right)$$

The second stage: If $t \geq \tau$, then

$$f_T(t) = \int_{-\infty}^{\infty} f_T(t|a_2)p(a_2)da_2$$
$$\cong \frac{1}{\sqrt{2\pi(t-\tau)^2\left(\sigma_{a_2}^2\left(\int_\tau^t u_2(t_2-\tau,\theta_2)dt_2\right)^2+\sigma_2^2(t-\tau)\right)}}$$
$$\times \left[\omega - x_\tau - \left(\int_\tau^t u_2(t_2-\tau,\theta_2)dt_2 - u_2(t-\tau,\theta_2)(t-\tau)\right) \times \right.$$
$$\left. \frac{(\omega - x_\tau)\sigma_{a_2}^2 \int_\tau^t u_2(t_2-\tau,\theta_2)dt_2 + u_{a_2}\sigma_2^2(t-\tau)}{\sigma_{a_2}^2\left(\int_\tau^t u_2(t_2-\tau,\theta_2)dt_2\right)^2+\sigma_2^2(t-\tau)}\right] \times \exp\left(-\frac{\left(\omega - x_\tau - u_{a_2}\int_\tau^t u_2(t_2-\tau,\theta_2)dt_2\right)^2}{2\left(\sigma_{a_2}^2\left(\int_\tau^t u_2(t_2-\tau,\theta_2)dt_2\right)^2+\sigma_2^2(t-\tau)\right)}\right)$$

Appendix B

$J_{i,n}$ and $O_{i,n}$ represent the mean and variance of the multivariate normal distribution that $\Delta X_{i,n}$ follows [16], expressed as follows.

$$J_{i,n} = \begin{cases} u_{a_1} H_{1,n}, & i = 1 \\ u_{a_2} H_{2,n}, & i = 2 \end{cases}$$

$$O_{i,n} = \begin{cases} \sigma_{a_1}^2 H_{1,n} H_{1,n}' + \sigma_1^2 S_{1,n}, & i = 1 \\ \sigma_{a_2}^2 H_{2,n} H_{2,n}' + \sigma_2^2 S_{2,n}, & i = 2 \end{cases}$$

where $H_{1,n} = \left[\int_0^{t_{n,1}} u_1(t_1, \theta_1) dt_1 , \int_{t_{n,1}}^{t_{n,2}} u_1(t_1, \theta_1) dt_1 , \dots , \int_{t_{n,k_{1,n}-1}}^{t_{n,k_{1,n}}} u_1(t_1, \theta_1) dt_1 \right]'$,

$H_{2,n} = \left[\int_{t_{n,k_{1,n}}}^{t_{n,k_{1,n}+1}} u_2(t_2, \theta_2) dt_2 , \int_{t_{n,k_{1,n}+1}}^{t_{n,k_{1,n}+2}} u_2(t_2, \theta_2) dt_2 , \dots , \int_{t_{n,k_{2,n}+k_{1,n}-1}}^{t_{n,k_{2,n}+k_{1,n}}} u_2(t_2, \theta_2) dt_2 \right]'$,

$$S_{1,n} = \begin{bmatrix} t_{n,1} & t_{n,1} & \dots & t_{n,1} \\ t_{n,1} & t_{n,2} - t_{n,1} & \dots & t_{n,2} - t_{n,1} \\ \vdots & \vdots & \ddots & \vdots \\ t_{n,1} & t_{n,2} - t_{n,1} & \dots & t_{n,k_{1,n}} - t_{n,k_{1,n}-1} \end{bmatrix}, \text{ and}$$

$$S_{2,n} = \begin{bmatrix} t_{n,k_{1,n}+1} - t_{n,k_{1,n}} & t_{n,k_{1,n}+1} - t_{n,k_{1,n}} & \dots & t_{n,k_{1,n}+1} - t_{n,k_{1,n}} \\ t_{n,k_{1,n}+1} - t_{n,k_{1,n}} & t_{n,k_{1,n}+2} - t_{n,k_{1,n}+1} & \dots & t_{n,k_{1,n}+2} - t_{n,k_{1,n}+1} \\ \vdots & \vdots & \ddots & \vdots \\ t_{n,k_{1,n}+1} - t_{n,k_{1,n}} & t_{n,k_{1,n}+2} - t_{n,k_{1,n}+1} & \dots & t_{n,k_{2,n}+k_{1,n}} - t_{n,k_{2,n}+k_{1,n}-1} \end{bmatrix}.$$